Met. O. 946

METEOROLOGICAL OFFICE

Scientific Paper No. 40

The Meteorological Office GATE Modelling Experiment

edited by P. R. ROWNTREE, Ph.D. and H. CATTLE, Ph.D., D.I.C.

LONDON: HER MAJESTY'S STATIONERY OFFICE

£8.80 NET

Met. O. 946

METEOROLOGICAL OFFICE

Scientific Paper No. 40

The Meteorological Office GATE Modelling Experiment

edited by P. R. ROWNTREE, Ph.D. and H. CATTLE, Ph.D., D.I.C.

LONDON: HER MAJESTY'S STATIONERY OFFICE

U.D.C. 551.506.24:
551.509.313

© *Crown Copyright 1983*

ISBN 011 400342 4

Contents

	Page
Notation	iv
Summary	1
1. Introduction	1
2. The GATE modelling experiment	2
3. Data	3
4. Analysis	8
5. Vertical interpolation	26
6. Dynamic initialization during the GATE experiment	27
7. Forecast model	34
8. Results of the forecast experiment	41
9. Revised estimates of the background field error statistics	63
10. Some experiments since GATE	67
11. Concluding remarks	73
Acknowledgements	73
Bibliography	74

a	radius of the earth
$\mathbf{A}$	$(n + 1) \times (n + 1)$ matrix with elements $A_{ij} = \overline{\epsilon_i \epsilon_j}$
b	coefficient used in filtering
$\mathbf{B}$	column vector with $(n + 1)$ elements $\overline{s_g \epsilon_i}$ $\quad i = 1, n + 1$
c	constant used in final data check
c_o	diurnal variation coefficient
C	constant used by the convective scheme
C_D	drag coefficient
d_{p_l}	correction applied to the background field at a secondary analysis level, p_1, following analysis at primary levels.
D	lateral divergence
E_p	potential evaporation rate
E_v	evaporation rate
$\overline{E^2}$	the mean square analysis error at a grid point
f	Coriolis parameter
f_t	any model parameter at time t
$\hat{f}_t$	time-meaned value of f_t
g	acceleration due to gravity
H	upward flux of sensible heat
I	variational integral
k	subscript indicating a level of the model (as in σ_k, U_k etc)
$\mathbf{k}$	unit vertical vector
K	eddy diffusion coefficient
l	mixing length
L	Obukhov length
L_*	scaling length: minimum value of $(10^4, u_*/f)$
n	number of observations used in analysis at a particular grid point.
N_i	order of filter in direction normal to the boundary of the ith boundary row ($i \leqslant 3$)
p	pressure
p_*	pressure at the earth's surface
p_0	pressure at mean sea level
p_i	weight used in analysis
$\mathbf{P}$	column vector with $(n + 1)$ elements p_i
$\mathbf{P}^T$	transpose of column vector $\mathbf{P}$
q	specific humidity
q_0	surface value of specific humidity
r	correlation function for background field errors
r_{ij}	correlation coefficient of background field errors at points i and j
R	long-wave cooling rate
R_D	gas constant for dry air
R_m	gas constant for moist air
s	generalized variable for analysis
s_i	the observed value of s at point i
$\hat{s}_i$	the true value of s at an observation point

$\hat{s}_g$	the true value of s at a grid point
$\tilde{s}_i$	the background field value of s at an observation point
$\tilde{s}_g$	the background field value of s at a grid point
s_{ic}	unweighted estimate of the true value of s at a grid point derived from a single observation and/or the background field.
s_{ge}	estimate of the true value of s at a grid point from a weighted combination of values of s_{ic}.
S	mean daily radiative heating rate
S_G	net downward solar flux
S_i	coefficient multiplying tendencies of the ith boundary row ($i \leqslant 3$) used in 'sponge' boundary conditions
S_{ij}	$S_i \times S_j$: combination of S_i and S_j used at grid corners where grid rows (i) and columns (j) overlap.
t	time
T	temperature
T_0	surface temperature
T_v	virtual temperature
$\mathbf{T}$	column vector with $(n + 1)$ elements equal to unity
$\mathbf{T}^T$	transpose of $\mathbf{T}$
u_*	friction velocity
$\mathbf{u}$	vector representing all the model variables
$\mathbf{u}^*, \mathbf{u}^{**}$	intermediate values of $\mathbf{u}$ during dynamic initialization
$\mathbf{u}^{(\nu)}$	value of $\mathbf{u}$ after the νth iteration in dynamic initialization
$\mathbf{V} \equiv (u, v)$	lateral vector wind
U, V	$p_* u, p_* v$
$\tilde{\mathbf{V}} \equiv (\tilde{u}, \tilde{v})$	vector wind as analysed, prior to Sasaki step
$\tilde{\mathbf{V}}_{1000}$	value of $\tilde{\mathbf{V}}$ appropriate to 1000 mb
$\mathbf{V}_{10} \equiv (u_{10}, v_{10})$	vector wind at 10 m
W	wave frequency
W_k	weight appropriate to level k used in calculating values of T, q, U, V at layer boundaries for vertical flux divergence calculations.
X_k	any one of T, q, U, V for model level k
x, y	lateral grid coordinates
z	geometric height
z_0	roughness length
z_m	height of the centre of the lowest model layer
α, β, γ	variational parameters
$-\alpha_*$	rate of change with height of the angle between the stress vector and the geostrophic wind.
β_*	$\lvert\partial\tau/\partial z\rvert/\lvert\tau_0\rvert$
γ_c	typical lapse rate for the mean tropical atmosphere
Γ	climatological value of $\partial T/\partial(\ln p)$
δ_p	difference between analysis and background field values at a primary level p.
Δ_i	difference between true and background field values at an observation point

Δ_g	difference between analysis and background field values at a grid point.
ϵ_i	difference between the observed and background field values of s at point i.
ϵ_{oi}	error of an individual observation at point i.
$\overline{\epsilon_o^2}$	variance of observational errors.
$\overline{\epsilon_{oo}^2}$	contribution to the observational error variance of AIREP and GOES observations.
ϵ_{70}	difference between observed and analysed geopotential heights at 70 mb.
ϵ_p	correction to be applied to a radiosonde observed geopotential for pressure level p.
$\overline{\epsilon_{70}^2}$	variance of radiosonde geopotential errors at 70 mb.
$\overline{\epsilon_p^2}$	estimated variance of radiosonde geopotential errors at pressure level p.
ϵ_*	effective surface emissivity.
ζ	constant used in determining estimates of the variance of radiosonde geopotential errors.
η	parameter describing the width of the correlation function for background field errors used during GATE.
θ, λ	latitude, longitude.
Θ	potential temperature.
κ	coefficient relating $\tilde{\tau}_{1000}$ to $\tilde{\mathbf{V}}_{1000}$.
κ_m	ratio of the gas constant to specific heat at constant pressure, for moist air.
κ_D	as above, for dry air.
λ_u	$u_{11}^2/[g(\delta_0\Theta/\Theta_{11} + 0.61\delta_0 q)]$
Λ	Lagrange undetermined multiplier
μ_k, ν_k	$\ln(\sigma_{k+\frac{1}{2}}/\sigma_k)/\ln(\sigma_{k+\frac{1}{2}}/\sigma_{k-\frac{1}{2}})$
ξ	$\gamma\alpha/(\alpha + \gamma f^2)$
ρ	air density
σ	pressure/surface pressure $= p/p_*$
$\dot{\sigma}$	$\mathrm{D}\sigma/\mathrm{D}t$
σ_0	Stefan's constant
τ	frictional stress vector.
τ_0	frictional stress at the surface
$\tilde{\tau} \equiv (\tilde{\tau}_\theta, \tilde{\tau}_\lambda)$	frictional stress vector derived from $\tilde{\mathbf{V}}$
$\tilde{\tau}_{1000}$	value of $\tilde{\tau}$ appropriate to 1000 mb
Φ	geopotential
$\tilde{\Phi}$	geopotential as analysed, prior to the Sasaki step.
Φ_b	geopotential field derived from the wind field by solution of the balance equation, prior to the Sasaki step.
Φ_*	geopotential of the land surface
ψ	station separation measured in terms of the angle subtended at the centre of the earth by the great circle passing through two stations.
ω	$\mathrm{D}p/\mathrm{D}t$
$\overline{A}$	ensemble average of A

$\overline{A}^{x}$	$\{A[x + \Delta x/2] + A[x - \Delta x/2]\}/\Delta x$
δA	arbitrary variation in A
$\delta \mathbf{A}$	arbitrary variation in vector $\mathbf{A}$
$\delta_x A$	$\{A[x + \Delta x/2] - A[x - \Delta x/2]\}/\Delta x$
$\delta_0 A$	difference between A at the lowest model level and at the surface.
Δx	increment in x
$\Delta X_{k+\frac{1}{2}}$	$X_{k+1} - X_k$
$\mathrm{d}S$	element of area
$\mathrm{d}\mathbf{l}$	vector line element
$\mathrm{D}/\mathrm{D}t$	total time derivative
$\partial/\partial t$	partial derivative
∇	lateral gradient operator
$\nabla\cdot$	lateral divergence operator
$\mathscr{L}$	general non-linear operator

The Meteorological Office GATE Modelling Experiment

Edited by P. R. Rowntree, Ph.D. and H. Cattle, Ph.D., D.I.C.

SUMMARY

This paper describes modelling work with a tropical forecast suite developed specifically to take advantage of the increased data coverage in the tropical Atlantic during the GARP Atlantic Tropical Experiment (GATE) of June to September 1974. The paper includes a description of the data extraction methods, a summary of data obtained and a detailed account of the analysis, interpolation, initialization and forecast techniques. Results shown indicate the quality of the analyses and the effects of initialization on the analyses and forecasts. Major errors of the forecasts are documented together with examples of forecasts made since GATE with improved versions of the model and modified initial fields.

1. INTRODUCTION

This paper is an account of the experiment in numerical modelling of the tropics carried out by the Meteorological Office during GATE in the period June–September 1974*. GATE was the Atlantic Tropical Experiment of the Global Atmospheric Research Program (GARP). GARP is a joint program of the World Meteorological Organization and the International Council of Scientific Unions. Its aims are to study atmospheric processes which are essential for understanding (a) the transient behaviour of the atmosphere, so leading to an increase in the accuracy of forecasts over periods ranging from one day to a few weeks and (b) factors that determine the general circulation of the atmosphere, so leading to a better understanding of the physical basis of climate. The primary aim of GATE followed from this — to extend our knowledge of those aspects of tropical meteorology which are essential for a proper understanding of the circulation of the whole atmosphere. However, it was also envisaged in the GATE Design Proposal (World Meteorological Organization 1972) that GATE would provide a basis for a major advance in the understanding of tropical meteorology and weather forecasting.

A principal tool in achieving GARP aims is the numerical simulation of atmospheric behaviour in models; the development of modelling of the tropical atmosphere has previously been limited by the lack of synoptic data with adequate density and spatial extent. In models atmospheric variables such as wind components, temperature, moisture and surface pressure are represented as averages over squares of sides of the order of 200 km. To include the effects of smaller-scale processes such as cumulonimbus clouds or evaporation it is necessary to 'parametrize' them — that is to say, to represent them in terms of the space-averaged variables. Prior to GATE, knowledge of the small-scale disturbances was not sufficient for effective parametrization. Thus one immediate aim of GATE was to provide a basis for the development of parametrizations of the effects of smaller tropical weather systems on the larger-scale circulations. A second aim was to provide data for testing numerical models in the tropics.

* Shorter accounts of some of the work presented here appear in Jones (1976) and Lyne *et al.* (1976).

Late in 1972, plans were prepared in the Meteorological Office to take advantage of the improved data coverage expected over part of the tropics during GATE by carrying out modelling experiments using the GATE data as they were received and to continue, after GATE, with further experimental work designed to develop and test parametrization methods and modelling techniques against the GATE data. Work on the project commenced early in 1973, about 18 months before GATE, the objective analysis scheme being developed in the Forecasting Research Branch and the rest of the work being done in the Dynamical Climatology Branch. This paper documents the techniques used and reports on the results obtained during GATE. Brief accounts are included of subsequent work carried out in the Dynamical Climatology Branch on analysis and forecasting techniques.

2. THE GATE MODELLING EXPERIMENT

The GATE modelling experiment required a data extraction–analysis–forecast cycle which can be summarized as follows:

(a) Derive wind and geopotential background fields from a previous forecast verifying at time t by interpolation from σ- to p-surfaces, except for relative humidity which was analysed for model σ-layers directly (σ = pressure/surface pressure = p/p_*).

(b) Extract data for time t.

(c) Adjust background fields in the light of the observational data and mutually adjust the wind and geopotential fields, using a variational analysis technique, to give preliminary analyses.

(d) After study of data and analyses, insert corrections and bogus data as required and repeat (c) for wind and geopotential fields to give final analyses.

(e) Interpolate from wind and geopotential fields on pressure surfaces to give wind and temperature fields for σ-layers and the surface pressure field.

(f) Reduce high-frequency waves by mutual adjustment of wind and mass fields in a dynamic initialization step.

(g) Use model to advance fields from time t to time $t + \Delta t$.

Though requiring procedures similar to those for the operational numerical forecasting system which had developed in the Meteorological Office over many years (Knighting *et al.* 1962, Burridge and Gadd 1977) GATE modelling required considerable new work which may be summarized as follows:

(i) *Data extraction.* Additional types of data were used and quality control methods applicable to the tropics were designed. Special lists of stations to be used in the analysis were constructed and additional broadcasts monitored to optimize the receipt of data. This work is described in more detail in section 3.

(ii) *Objective analysis.* The operational scheme analysed fields of geopotential and humidity, wind data being used only to assess geopotential gradients. Because of the important role of wind data in the tropics and the rather weak relationship between wind and geopotential fields, it was necessary to develop an entirely

new scheme in which both of these fields were analysed. This scheme is described in section 4.

(iii) *Interpolation, initialization and forecast.* A limited-area tropical model was designed for use in the GATE modelling work as discussed in section 7. Because this model's vertical coordinate is σ, or the ratio of pressure to surface pressure, techniques had to be devised to provide accurate interpolation of data from the pressure surfaces, used in analysis, to the model's σ-surfaces (section 5). A reverse interpolation was also required to provide the forecast background fields for the analysis.

To remove initial imbalances between the interpolated wind and geopotential fields and so provide a smooth start to the forecasts a dynamic initialization procedure, using the forecast model, was included as described in section 6.

(iv) *Intervention.* Special computer programs were required to allow detection and correction of erroneous data, and insertion of data invented to correct analysis errors. Forms were designed to aid in the insertion of these data. Scientists from the Dynamical Climatology and Forecasting Research Branches carried out the monitoring and intervention duties.

(v) *Output programs.* A wide range of output, including maps and tabulations of data, analyses and forecasts was required to assist with the monitoring of the experiment.

Throughout each main observing phase of GATE a forecast–analysis cycle was run with 12-hourly input of data during Phases I and II (25 June to 16 July and 28 July to 17 August 1974) and 24-hourly updating during Phase III (29 August to 18 September 1974).

Analyses were made for 00 and 12 GMT during Phases I and II and for 12 GMT during Phase III. The switch to 24-hourly updating allowed more detailed assessment of the data and analysis quality and of the need for bogus data. It also tested the forecast over a longer period while reducing computer usage. After the first few days the experiment generally ran successfully except that during Phase I several runs were affected by errors, a few being effectively lost owing to the use of wrong background fields, data or analyses when failure of a step to overwrite results from an earlier run was not detected in time.

3. DATA

The upper air geopotential and humidity data came from radiosondes launched from ship stations and land stations; geopotential thickness data from satellite sounding reports (SIRS) were also used. Upper-wind data came from pilot balloon, and rawinsonde observations (radar or LOCATE systems), aircraft reports and satellite cloud vector reports. Finally, surface reports from both ship and land stations were also employed.

Data were received principally via the Global Telecommunication System and via transmissions from Cyprus and Nairobi. Because of a change in transmission frequen-

cies, Dakar broadcasts became unavailable prior to GATE but were received during part of Phase II and Phase III.

The distribution of stations from which data were sought is illustrated in Figures 1 (a)–(c). Although the operational analyses were usually run about 24 hours after observation time, a large number of the observations which might have been available were, in fact, not received, or were not extracted owing to errors in coding and transmis-

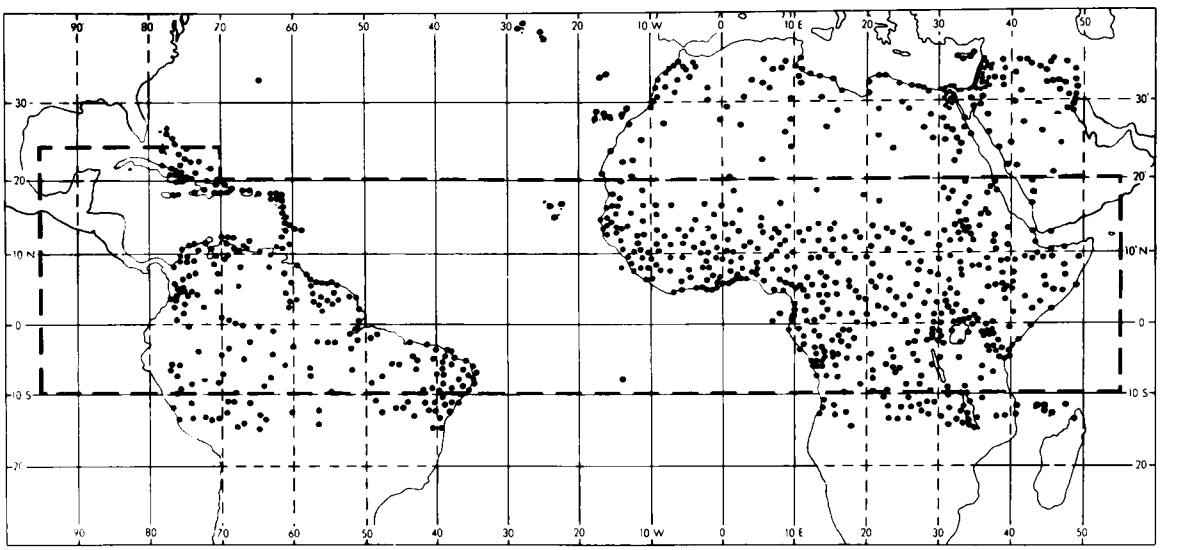

FIGURE 1(a). Surface observation stations over land

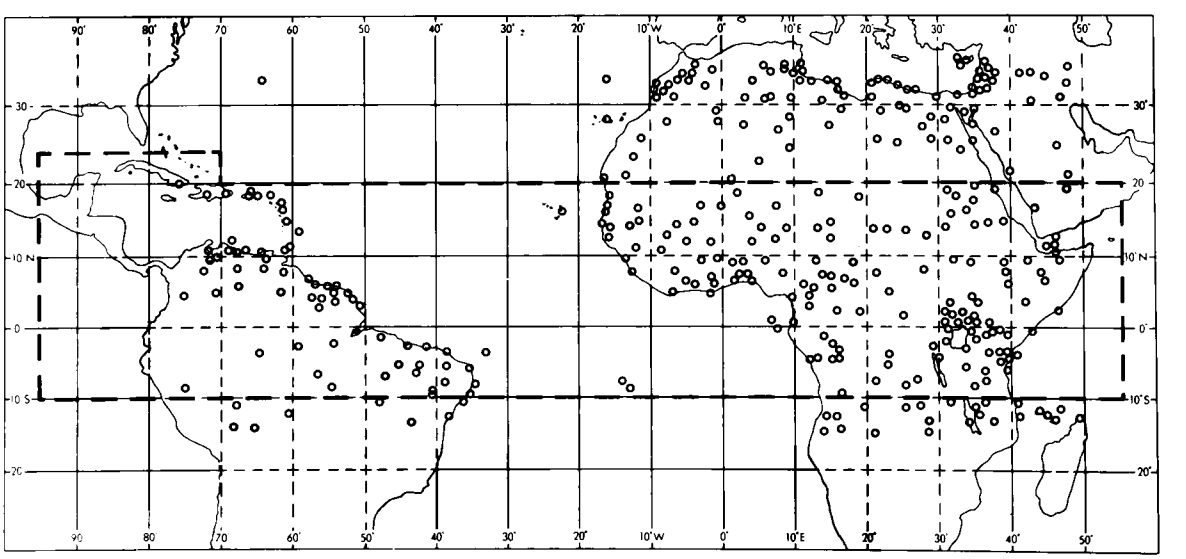

FIGURE 1(b). Upper-air observation stations over land

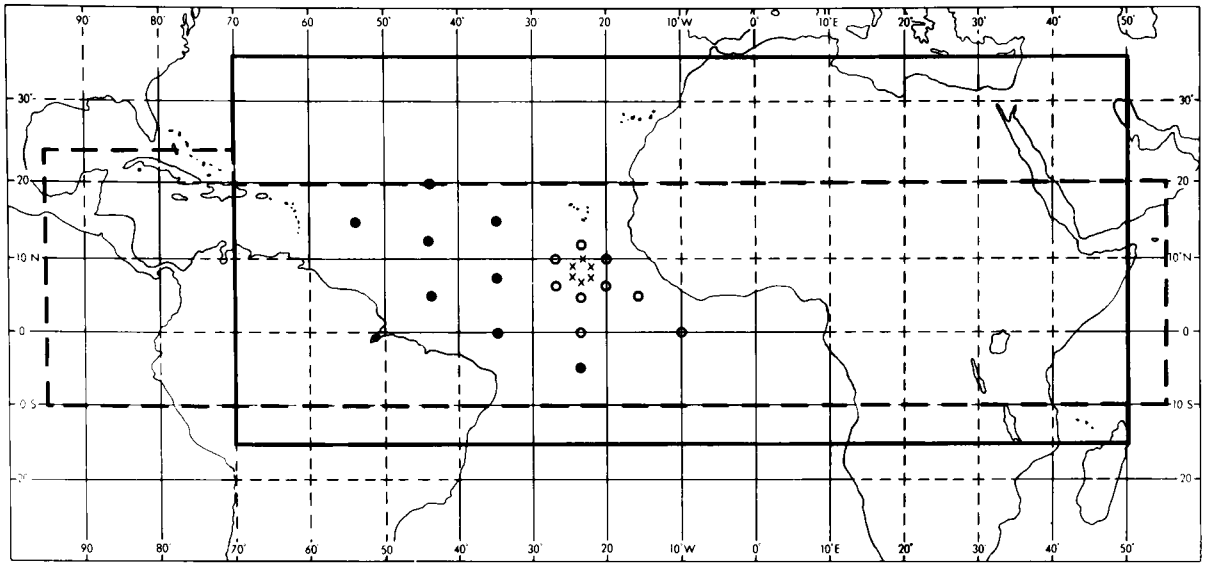

FIGURE 1(c). A- and B-scale ship distribution (Phase I)
x A-scale o A/B scale • B-scale
– – – GATE A-scale area
—— Area of analysis for the UK modelling experiment

sion. The amount of data extracted increased progressively as the experiment proceeded, however; the number of reports extracted on this quasi-operational scheme during Phase III is shown in Table I. The distribution of data received is shown in Figures 2 (a)–(c) (from Spackman and Farmer 1975.)

Analyses were carried out at fixed times and no attempt was made to adjust off-time observations in any way at all except to reduce their weight (increase their error variance) as their time discrepancy increased. Data observed at times differing by more than 6 hours from the analysis time were given zero weight.

TABLE I. *Number of reports extracted daily during Phase III (29 August–19 September 1974)*

	Average	Maximum	Minimum
Upper-air temperature (land)	71	81	61
Upper-air wind (land)	97	120	66
Upper-air (ship)	24	33	13
Surface (land)	532	619	398
Surface (ship)	168	200	114
Aircraft reports	63	90	47
SIRS	60	82	21
Satellite wind	280*	408	118

*4–19 September

Statistics relate to observations made at 12 GMT or centred on 12 GMT for satellite and aircraft reports.

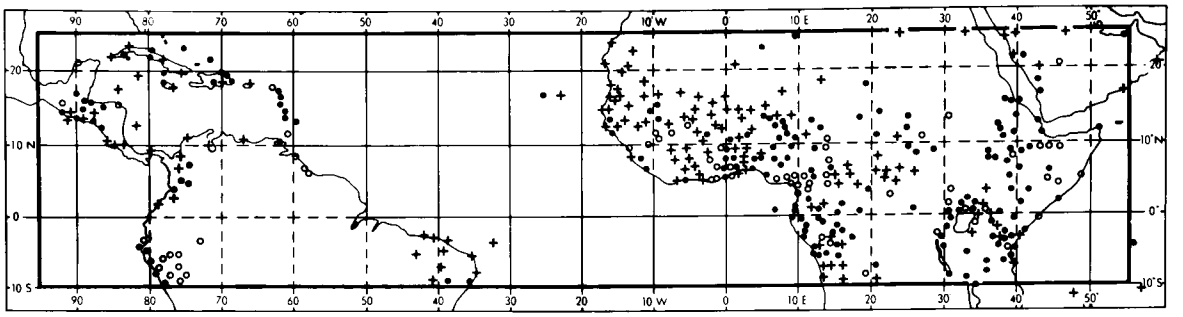

FIGURE 2(a). Number of SYNOP reports extracted during the first 11 days of Phase III for 12 GMT

o 1–3 reports • 4–8 reports + 9–11 reports

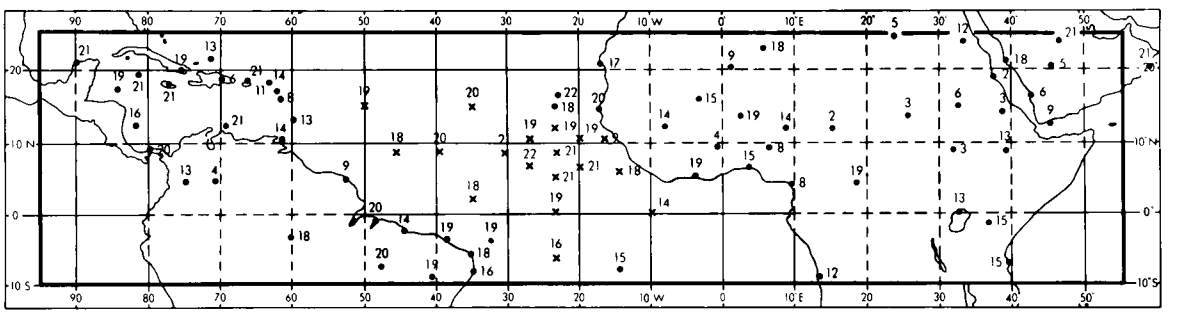

FIGURE 2(b). Number of TEMP reports extracted at 12 GMT during Phase III (21 days)

• Land stations x GATE ship platforms

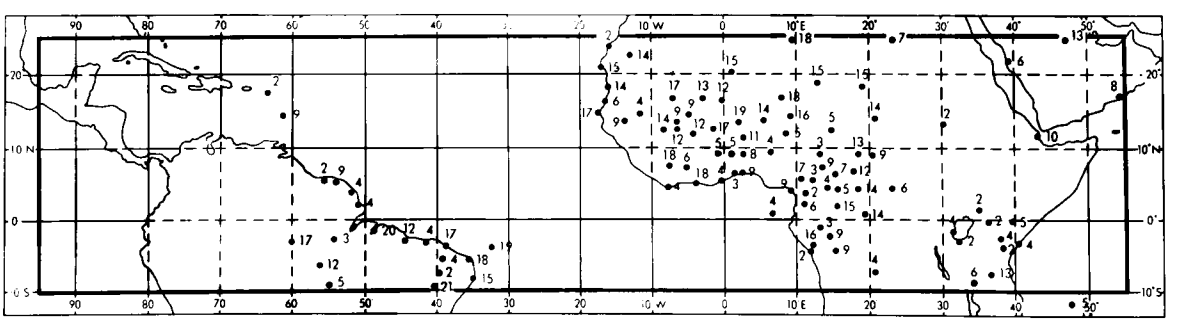

FIGURE 2(c). Number of PILOT reports extracted during Phase III (21 days)

The satellite wind data used came from the ATS 3 satellite during Phase II and, following code changes necessitated by the change of source, from synchronous meteorological satellites (SMS) from 4 September onwards in Phase III. High-level and low-level satellite winds were allocated to the 250 mb and 850 mb analysis levels respectively. Winds from aircraft reports were used at the two nearest analysis levels, one above and one below, and were adjusted to take into account the vertical wind shear. The shears used were the forecast values available from the background fields.

To provide higher resolution in the boundary layer, where the forecast model (section 7) had relatively fine structure, 950 mb geopotential data were estimated using special-point data from radiosonde reports. However, if the result of this calculation differed by more than 15 geopotential metres (gpm) from a value interpolated between the 1000 and 850 mb geopotentials, the interpolated value was used. To avoid the use of uncorroborated 950 mb geopotentials, no value was used if either 1000 or 850 mb geopotential data were flagged (see below) or missing.

For data retrieved from the Meteorological Office synoptic data bank, the quality control warning flags set by the data bank were used. Flagged data were not used in checking other data (see section 4.2.6) but could be retained if not rejected in the analysis data check. This was done because flagged data were sometimes found to be correct; however, retention of such data did lead to analysis errors on some occasions. During Phase III the data bank included no quality control for SMS wind data, so simple checks on wind speed and direction, and position and duplication of data were included.

Special climatological checks on geopotential data were devised for radiosonde observations, based on the variances of geopotential given by Oort and Rasmusson (1971). Data outside estimated climatological limits were flagged, or, if sufficiently extreme, eliminated. If an ascent had several levels outside climatological limits, then the whole ascent was discarded. Further data checks were carried out during analysis as described in section 4.2.6. Despite these measures, it was evident that a substantial proportion of forecast errors were due to incorrect geopotential data. As discussed in section 10.1, in experiments after GATE the best results were obtained when geopotential fields were derived from wind fields using the balance equation, taking account of geopotential data only through the boundary values.

Where possible, radiosonde reports were corrected for systematic bias at all levels (Hawson and Caton 1961). The 1000 mb analysis was carried out first to provide a reference level for the SIRS observations. The next level to be analysed was 70 mb and after this had been done, all radiosonde reports at this level were compared with the analysed fields and the differences (ϵ_{70}) used to estimate the errors at other levels in the sounding. Fractional corrections (ϵ_p) were then made to the observed values at other pressure levels (p) such that

$$\epsilon_p = \epsilon_{70} \times \frac{\ln(p/1000)}{\ln(70/1000)} .$$

Note that a radiosonde was rejected for $|\epsilon_{70}| \geqslant 300$ gpm. This procedure was repeated following the succeeding 100 mb analysis for radiosondes which only attained this level. Corrections for excessive warmth were also made to SIRS data as from 12 GMT on 15 July. Corrections varied from 20 gpm at 850 mb to 40 gpm at 500 mb and 110 gpm at 70 mb.

4. ANALYSIS

by D. E. Jones, M.Sc., D.I.C., A.R.C.S., H. Cattle, Ph.D., D.I.C. and P. Graystone, B.A.

4.1. *Introduction*

In this section the techniques used to provide the analyses of geopotential and wind fields on pressure surfaces, prior to interpolation to σ-surfaces (section 5), are described. The method used to analyse the humidity fields (done for σ-layers directly) was that described by Atkins (1974) and will be outlined only briefly. For geopotential and horizontal wind components, an analysis scheme which combined the methods of optimum interpolation and variational analysis was used.

The optimum interpolation scheme was based on the work of Gandin (1963), but used a model forecast field as a background field as described, *inter alia*, by Kruger (1969). It was decided to use optimum interpolation because the density of data varied considerably from one part of the area to another and optimum interpolation can cope with a spatially biased set of data better than most methods. The analyses were carried out for the 1000, 950 (geopotential only), 850, 700, 500, 400, 300, 250, 200, 150, 100 and 70 mb pressure levels; it was originally intended to include the 30 and 10 mb levels but the quality and quantity of the data were too poor, and so climatological values were used instead. The analysis area extended from 35°N to 15°S and from 77°W to 49°E (Figure 1(c)). A latitude–longitude grid was used with a spacing of 2°.

Because of the northerly latitude reached by the analysis area, a certain amount of balancing between the wind and mass fields was desirable. For this reason an adjustment scheme was used, based on the numerical variational analysis of Sasaki (1970). Use of this scheme enabled the field of one variable to influence the field of the other. This was important in data-sparse areas. In particular, there were often large numbers of satellite wind vectors available for areas where there were few reliable observations of geopotential—for instance over central South America and the south-western parts of the tropical Atlantic. The adjustment step was carried out following the basic analyses of mass and velocity on pressure surfaces and prior to vertical interpolation to σ-surfaces. It will therefore be discussed here, following description of the optimum interpolation analysis scheme.

4.2. *The optimum interpolation scheme*

4.2.1. *Mathematical formulation.* Let us denote any one of the variables to be analysed by s; then the purpose of our analysis is to form the best possible estimates s_{ge} of the true values, $\hat{s}_g$, of s at a set of grid points. So that we may form such an estimate at a grid point let us select a set of n observations, s_i, of s in the neighbourhood of the grid point where we also have a background value, $\tilde{s}_g$. If we can assume that we may also derive the background values at the observation points, then we can define a set of $(n + 1)$ individual estimates of s at the grid point to be:

$$s_{ie} = s_i - \tilde{s}_i + \tilde{s}_g \qquad i = 1, n$$

$$s_{ie} = \tilde{s}_g = \tilde{s}_g - \tilde{s}_g + \tilde{s}_g \qquad i = n+1$$

and take our estimate of s to be given by a weighted mean of the individual estimates, i.e. by

$$s_{ge} = \sum_{i=1}^{n+1} p_i s_{ie} \qquad \ldots (1)$$

where we specify the constraint on the weights p_i that

$$\sum_{i=1}^{n+1} p_i = 1 \qquad \ldots (2)$$

The problem now is to determine the set of weights, p_i. To this end we define the optimal set of p_i as that set which minimizes the mean-square error of the analysis at the grid point, given the same configuration of observing stations on all occasions; i.e. defining $\overline{E^2} = \overline{(s_{ge} - \hat{s}_g)^2}$, where the bar represents a mean over many meteorological situations, we define the optimal set of p_i by solving the $(n + 2)$ equations:

$$\begin{aligned} &\partial \overline{E^2} \,/\, \partial p_j = \Lambda \qquad\qquad j = 1, n+1 \\ &\sum_{j=1}^{n+1} p_j = 1 \end{aligned} \qquad \ldots (3)$$

where Λ is the Lagrange undetermined multiplier of $\sum_{j=1}^{n+1} p_j = 1$. Substituting into $\overline{E^2}$ from (1) for s_{ge} we obtain the set of equations

$$\frac{\partial}{\partial p_j} \overline{\left(\sum_{i=1}^{n+1} p_i s_{ie} - \hat{s}_g\right)^2} = \Lambda \qquad j = 1, n+1$$

which yields the further set

$$2s_{je} \overline{\left(\sum_{i=1}^{n+1} p_i s_{ie} - \hat{s}_g\right)} = \Lambda \qquad j = 1, n+1$$

If we now write $s_{ie} = \hat{s}_g + \epsilon_i$, this gives us

$$2(\hat{s}_g + \epsilon_j) \overline{\left(\sum_{i=1}^{n+1} p_i \hat{s}_g - \hat{s}_g + \sum_{i=1}^{n+1} p_i \epsilon_i\right)} = \Lambda \qquad j = 1, n+1$$

and using the condition $\sum_{i=1}^{n+1} p_i = 1$ we obtain

$$2(\hat{s}_g + \epsilon_j) \sum_{i=1}^{n+1} p_i \overline{\epsilon_i} = \Lambda \qquad j = 1, n+1$$

In matrix notation, the $(n + 2)$ equations (3) can thus be written as:

$$\mathbf{A}\cdot\mathbf{P} + (\mathbf{B}\cdot\mathbf{P})\,\mathbf{T} = \tfrac{1}{2}\Lambda\mathbf{T} \qquad \ldots (4a)$$

$$\mathbf{T}^{\mathrm{T}}\cdot\mathbf{P} = 1 = \mathbf{P}^{\mathrm{T}}\cdot\mathbf{T} \qquad \ldots (4b)$$

where $\mathbf{A}$ is the $(n + 1) \times (n + 1)$ matrix with elements $A_{ij} = \overline{\epsilon_i\epsilon_j}$; $\mathbf{B}$ is a column vector with $(n + 1)$ elements $\overline{\hat{s}_g\epsilon_i}$ and $\mathbf{P}$ is a corresponding vector for the weights p_i. $\mathbf{T}$ is a vector with $(n + 1)$ elements each equal to unity and $\mathbf{T}^{\mathrm{T}}$ is its transpose.

From (4a) we deduce that

$$\mathbf{P} = \mathbf{A}^{-1}\cdot\mathbf{T}\,\{\tfrac{1}{2}\Lambda - \mathbf{B}\cdot\mathbf{P}\}$$

Using (4b) we have

$$\mathbf{T}^{\mathrm{T}}\cdot\mathbf{P} = 1 = \mathbf{T}^{\mathrm{T}}\cdot\mathbf{A}^{-1}\cdot\mathbf{T}\,\{\tfrac{1}{2}\Lambda - \mathbf{B}\cdot\mathbf{P}\}$$

Hence

$$\{\tfrac{1}{2}\Lambda - \mathbf{B}\cdot\mathbf{P}\} = (\mathbf{T}^{\mathrm{T}}\cdot\mathbf{A}^{-1}\cdot\mathbf{T})^{-1}$$

and

$$\mathbf{P} = \mathbf{A}^{-1}\mathbf{T}/(\mathbf{T}^{\mathrm{T}}\cdot\mathbf{A}^{-1}\cdot\mathbf{T}) \qquad \ldots (5)$$

Thus we have obtained an expression for $\mathbf{P}$ in terms of the covariance matrix $\overline{\epsilon_i\epsilon_j}$. Now since $s_{ie} = \hat{s}_g + \epsilon_i$ we have

$$\epsilon_i = s_{ie} - \hat{s}_g = s_i - \tilde{s}_i + \tilde{s}_g - \hat{s}_g \qquad i = 1, n$$

$$\epsilon_{n+1} = s_{ie} - \hat{s}_g = \tilde{s}_g - \hat{s}_g \qquad i = n + 1$$

Let us now write $s_i = \hat{s}_i + \epsilon_{oi}$ where $\hat{s}_i$ represents the true value at the observation point and ϵ_{oi} the corresponding observational error. Then

$$\epsilon_i = \hat{s}_i + \epsilon_{oi} - \tilde{s}_i + \tilde{s}_g - \hat{s}_g \qquad i = 1, n$$

$$\epsilon_{n+1} = \tilde{s}_g - \hat{s}_g$$

If we now define Δ_i as the difference between the truth and the background fields at the point i and Δ_g as the corresponding quantity at the grid point, i.e.

$\Delta_i = \hat{s}_i - \tilde{s}_i$ and $\Delta_g = \hat{s}_g - \tilde{s}_g$ then

$$\epsilon_i = \epsilon_{oi} + \Delta_i - \Delta_g \qquad i = 1, n$$

$$\epsilon_{n+1} = -\Delta_g$$

and, since we may assume that the observational errors are random, so that ϵ_{oi} and ϵ_{oj} are correlated with nothing but themselves, then the elements of the matrix **A** become

$$\begin{aligned}
A_{ij} &= \overline{\epsilon_i\epsilon_j} = \overline{\Delta_i\Delta_j} + \overline{\Delta_g\Delta_g} - \overline{\Delta_i\Delta_g} - \overline{\Delta_j\Delta_g} && i \neq j;\ i, j \neq n+1 \\
A_{ii} &= \overline{\epsilon_i\epsilon_i} = \overline{\Delta_i\Delta_i} - 2\overline{\Delta_i\Delta_g} + \overline{\Delta_g\Delta_g} + \overline{\epsilon_{oi}^2} && i \neq n+1 \\
A_{i,\,n+1} &= \overline{\epsilon_i\epsilon_{n+1}} = \overline{\Delta_g\Delta_g} - \overline{\Delta_i\Delta_g} && i \neq n+1 \\
A_{n+1,\,n+1} &= \overline{\epsilon_{n+1}\,\epsilon_{n+1}} = \overline{\Delta_g\Delta_g} && \ldots(6)
\end{aligned}$$

The terms $\overline{\Delta_i\Delta_j}$ are the covariances of the errors of the background field (variances for suffixes which are identical). Thus if we can specify these quantities together with the observational error variances, we may determine the elements of **A** from (6) and solve (5) for the optimal weights p_i. The grid-point estimate is then obtained from the observed values using equation (1). It should be noted that the scheme defined by equations (1), (2) and (5) is, except in the particular choice of the background field, formally identical to that of Gandin (1963) (Cattle 1982).

Before we move on to discuss the particular choice of background field and the specification of appropriate error variances and covariances for the GATE analyses, we also note that the mean-square error of the analysis is given by

$$\overline{E^2} = \overline{\left(\sum_{i=1}^{n+1} p_i\epsilon_i\right)^2} = \sum_{i,j=1}^{n+1} \overline{(p_i\epsilon_i p_j\epsilon_j)} = \mathbf{P}^{\mathrm{T}}\cdot\mathbf{A}\cdot\mathbf{P}$$

whilst, from (4a),

$$\mathbf{A}\cdot\mathbf{P} = \mathbf{T}/(\mathbf{T}^{\mathrm{T}}\cdot\mathbf{A}^{-1}\cdot\mathbf{T})$$

$$\mathbf{P}^{\mathrm{T}}\cdot\mathbf{A}\cdot\mathbf{P} = \mathbf{P}^{\mathrm{T}}\cdot\mathbf{T}/(\mathbf{T}^{\mathrm{T}}\cdot\mathbf{A}^{-1}\cdot\mathbf{T}) = (\mathbf{T}^{\mathrm{T}}\cdot\mathbf{A}^{-1}\cdot\mathbf{T})^{-1}, \text{ using (4b)}$$

i.e. $$\overline{E^2} = (\mathbf{T}^{\mathrm{T}}\cdot\mathbf{A}^{-1}\cdot\mathbf{T})^{-1} \qquad \ldots (7)$$

4.2.2. *The background fields*. Background fields for the optimum interpolation were obtained from the forecast model for both winds and geopotentials. The forecast fields on σ-surfaces were first smoothed by means of a 17-point filter before interpolation to pressure levels. At 1000 mb, 950 mb and some parts of the 850 mb levels it was necessary for some downward extrapolation from the model forecasts to be done. At 70 mb the background field was a mixture of 85 per cent forecast and 15 per cent climatology. Boundary values were kept unaltered in the forecasts so that the background fields on the boundaries were persistence values from the previous analysis time.

At the so-called primary levels, that is to say 1000, 850, 500, 250, 100 and 70 mb, the background fields were used as they stood.* The other (secondary) levels, that is 950, 700, 400, 300, 200 and 150 mb, were modified on the basis of the analyses at the primary levels to give improved background fields and to help preserve the vertical consistency. The correction terms were formed by vertical interpolation of the differences between the analyses and background fields at the primary levels. Thus if δ_p is the difference

*Apart from a double application of 1-2-1 smoothing with effect from 14 September.

between analysis and background field at any primary level p and d_p is the correction applied to the forecast field at a secondary level, d_p was taken as:

$$d_p = \frac{p - p_2}{p_1 - p_2}\delta_{p_1} + \frac{p_1 - p}{p_1 - p_2}\delta_{p_2},$$

where p_1 and p_2 are two successive primary levels and p is now a secondary level between them.

4.2.3. *Background field error statistics*. We have seen that calculation of the weights involves the inversion of a matrix whose terms depend on the spatial covariances ($\overline{\Delta_i\Delta_j}$ etc.) of model error for the particular element being analysed (equations (5) and (6)). We write these equations in the form:

$$\overline{\Delta_i\Delta_j} = (\overline{\Delta_i^2} \cdot \overline{\Delta_j^2})^{\frac{1}{2}} r_{ij},$$

where $\overline{\Delta_i^2}$ etc. are the background field error variances and r_{ij} is the spatial correlation coefficient for these errors between points i and j. During GATE it was assumed that r_{ij} depends only on the horizontal distance between i and j. A correlation function of the form

$$r(\psi) = \frac{1 - \psi^2/2\eta^2}{(1 + \psi^2/\eta^2)^{5/2}}$$

was chosen as a model of an empirical curve published by Rutherford (1972). Its form ensures that the implied error spectrum is positive for all wavelengths. η is a parameter which defines the width of the function. It was set empirically to give $r(\psi) = 0$ at a distance equivalent to 20° of latitude (approximately 2200 km). The form of $r(\psi)$ with this value of η is shown in Figure 3.

The assessment of errors of the background field $\overline{\Delta_i^2}$, was a problem because no forecasts had been run on real data. An assessment of these was originally obtained before the start of the experiment from the model climatological variability to give error variances varying between 5 $(\text{gpm})^2$ and 48 $(\text{gpm})^2$ for geopotentials and 2 $\text{m}^2\ \text{s}^{-2}$ and 36 $\text{m}^2\ \text{s}^{-2}$ for winds, depending on latitude and level (see Meteorological Office 1976, Appendix 1). In running the scheme it became evident, however, that the estimates of error variance so obtained were far too optimistic and values over the chart were raised everywhere by 600 $(\text{gpm})^2$ for geopotentials and by 9 $\text{m}^2\ \text{s}^{-2}$ for winds at all levels. Later, during Phase II of the GATE experiment, a further large addition to the variances of the background fields was found to be necessary over the eastern part of the analysis region. There, background variances were raised a further 600 $(\text{gpm})^2$ for geopotentials and 36 $\text{m}^2\ \text{s}^{-2}$ for winds, with a linear adjustment into the rest of the background field between longitudes 18°E and 28°E. This latter adjustment was found necessary because the background fields over the east African area were particularly poor, since this was a strong inflow region on many occasions (see, for example, Figure 7(a)) often with few available data.

4.2.4. *Observational errors*. These were assessed from the literature and are summarized in Table II. Note that different error values were used for corrected as against uncorrected radiosondes. It is important to note that the error variances required by the optimum interpolation process are not just the instrumental errors but should also include the noise effects of scales of motion too small to be represented in the grid used.

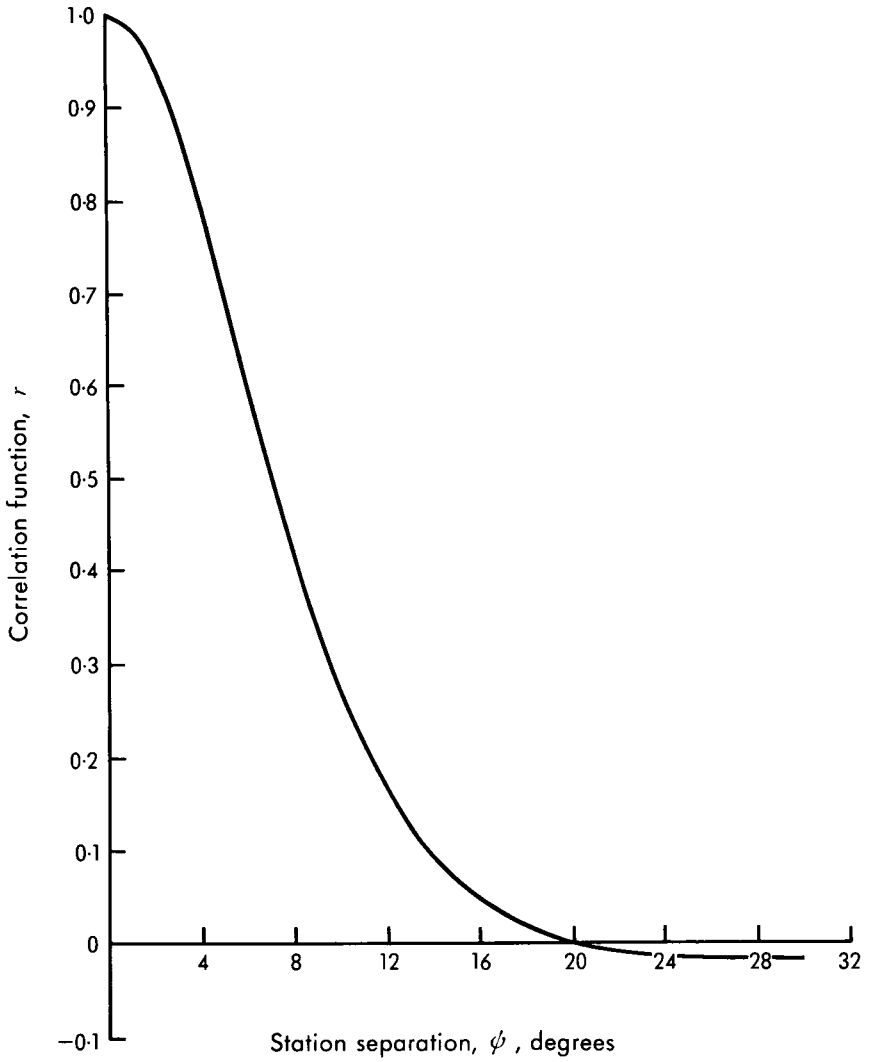

FIGURE 3. Function describing the correlation coefficient for errors of the background field at two stations as a function of station separation ψ as used during GATE.

The form of the curve is $r(\psi) = (1 - \psi^2/2\eta^2)/(1 + \psi^2/\eta^2)^{5/2}$ with ψ measured in terms of the angle (degrees) subtended at the centre of the earth by the great-circle arc passing through the two stations and $\eta = 14.14°$.

These effects were assumed to have no spatial correlation but to contribute to the estimated instrumental error variances by an amount equal to 2.25 $m^2\ s^{-2}$ for winds and addition of a value which varied with level for geopotential:

1000	950	850	700	500	400	300	250	200	150	100	70	mb
1.4	1.2	0.75	1.5	2.4	3.4	4.2	5.1	6.1	6.1	6.1	6.1	$(gpm)^2$

For a fuller discussion see Meteorological Office (1976).

TABLE II. *Specification of observational error variances for various data types*

Surface geopotential	$\overline{\epsilon_o^2} = 44$ (gpm)^2 (land and ship)
Upper-air geopotential	Radiosonde: Largest value of 44 (gpm)^2 and $\overline{\epsilon_p^2} = \overline{\epsilon_{70}^2}\zeta \left\{\frac{\ln(p/1000)}{\ln(70/1000)}\right\}^2$ where values of $\overline{\epsilon_{70}^2}$ were specified separately for each land station and took values of 900 (gpm)^2 over sea $\zeta = 1$ for uncorrected ascents $\zeta = 0.64 + 4 \times 10^{-6}\,\epsilon_{70}$ for corrected ascents (for ϵ_{70} see section 3) SIRS: $\overline{\epsilon_o^2} = (172 - 44 \log_{10} p)^2$
Surface wind	Ship: $\overline{\epsilon_o^2} = 4$ m^2 s^{-2}
Upper-air wind	Radar and pilot balloon (land and ship): $\overline{\epsilon_o^2} = (4.9 - 1.4 \log_{10} p)^2$ m^{2}s^{-2} OMEGA (ship): allocated according to ship position; values ranged from 1 m^2 s^{-2} in the north to 300 m^2 s^{-2} in the south-east corner of the analysis area AIREPS: $\overline{\epsilon_o^2} = \overline{\epsilon_{oo}^2} + 0.05\sigma_c^2\lvert\Delta t\rvert + 0.06\lvert\Delta p\rvert$ Δt = difference between observation and analysis times Δp = difference between observation and analysis levels σ_c^2 = (model) climatological variability (section 4.2.3) $\overline{\epsilon_{oo}^2} = (1.2)^2$ m^2 s^{-2} for spot winds; $(3.6)^2$ m^2 s^{-2} for mean winds GOES: $\overline{\epsilon_o^2} = \overline{\epsilon_{go}^2} + 0.05\sigma_c^2\lvert\Delta t\rvert$ $\overline{\epsilon_{oo}^2} = (5.4)^2$ m^2 s^{-2} for 850 mb; $(8.6)^2$ m^2 s^{-2} for 250 mb

4.2.5. *Selection of observations and derivation of the weights.* The number of observations used to estimate the value of the field at each grid point was kept to 8 (cf. Kruger 1969, Alaka and Elvander 1972). Raising the number to 12 made very little difference to the interpolated values and did not warrant the extra computational work involved. To remove any unwanted bias that might otherwise occur the search for data about the analysis point was made according to quadrant as follows: at upper levels the nearest synoptic wind (i.e. radar/omega/rawinsonde) or radiosonde height in each quadrant was accepted provided that it lay within a certain limiting distance. The number of observations was then made up to two in each quadrant by accepting the observation i of any type with the largest value of

$$\frac{\overline{\Delta_i \Delta_g}}{(\overline{\Delta_i^2} + \overline{\epsilon_{oi}^2})}$$

this being the weight which an observation would have in the absence of all others; this allowed a good quality observation to be selected even though it was somewhat further away from the grid point than another observation which was less reliable. The total

number of observations was made up to 8 (if necessary) by finally selecting observations irrespective of quadrant using the same parameter. An upper limit of 6 was placed on the number of observations chosen without regard to quadrant. To take advantage of the large number of surface observations that were available and to reduce the possibility of ill-conditioning (see below), all those which lay within each 1° square of latitude and longitude were averaged and the value allocated to an appropriate mean position. Though this 'super-ob' could be expected to have a smaller error variance than the original observations, the appropriate value as given in Table II was retained. A selection procedure similar to that for upper levels was then followed.

The set of linear equations for the weights (equation (5)) was solved by the method of Choleski (e.g. Hartree 1958, p. 180). Such a set of equations can, however, become ill-conditioned when two observations used in the interpolation are much closer to each other than either is to the grid point in question, especially when all three points fall on a straight line. The result is an interpolated value that can often be quite erroneous. It was found by experiment that the problem could be solved by combining any observation whose weight was less than -0.5 with its nearest neighbour and recalculating the weights appropriately.

4.2.6. *Data Checking*. All the data had undergone quality control checks, but a further check was introduced before the final analysis. To do this, each observation was compared with a value interpolated at its location from surrounding data by the analysis scheme. The observed value of a variable s was rejected if it did not satisfy the criterion

$$|s_{\text{observed}} - s_{\text{interpolated}}| < c_V(\overline{\epsilon_o^2} + \overline{E^2})$$

where $\overline{\epsilon_o^2}$ is the observational error variance and $\overline{E^2}$ is the variance of the errors of analysis (see section 4.2.1). The criterion is based on the theory of maximum likelihood (see Meteorological Office 1976, Appendix 2). The constant c can obviously be varied according to the severity of the test required; during GATE it was given values of 6 for geopotentials and 12 for winds. Note that an observation with a large deviation is more likely to be accepted where the analysis is regarded as being unreliable or if the observation itself has a large observational error variance attributed to it. However, in the latter case the weight that the observation is allotted in the analysis scheme will be small on this account.

In performing the data checking, two sweeps were made through the observations. The first sweep was made using only those data that had not been rejected by the preceding data extraction quality control checks. The second sweep was made just through those observations rejected by the first sweep; they were reaccepted by the analysis if they now satisfied the necessary criterion. This was done in case observations had been rejected in the first check owing to the inclusion of observations later found to be incorrect.

In spite of these checks a considerable amount of human monitoring was required, correcting erroneous reports or inserting artificial ones where this was thought desirable. Considerable difficulty was encountered over the mountainous regions of east Africa, over South America and the south-western part of the tropical Atlantic and around the boundaries. In general, analyses were not amended subjectively unless they contained features that were obviously unrealistic.

4.3 *Adjustment stage*

4.3.1. *Theoretical background.* Up to the adjustment stage the analyses of geopotential and wind were independent of each other, with the exception that the background fields of both were derived from the prediction model. The adjustment used was based on the numerical variational analysis due to Sasaki (1970) using a 'weak constraint' in the 'timewise-localized' form, also used successfully by Lewis and Grayson (1972). Carrying out this step allows the field of one variable to adjust to the field of another and to reduce the time necessary for initialization (section 6).

In our case the variational integral to be minimized is taken to be

$$I = \int\int[\alpha(\mathbf{V} - \tilde{\mathbf{V}})^2 + \beta(\Phi - \tilde{\Phi})^2 + \gamma\{\nabla(\Phi - \Phi_b) + f\mathbf{k} \times (\mathbf{V} - \tilde{\mathbf{V}})\}^2]\mathrm{d}S$$

where

$\mathbf{V}$ = final value of the velocity field,
$\tilde{\mathbf{V}}$ = initial (analysis) value of the velocity field,
Φ = final value of the geopotential field,
$\tilde{\Phi}$ = initial (analysis) value of the geopotential field,
Φ_b = geopotential field obtained from $\tilde{\mathbf{V}}$ by solving the balance equation, and
$\mathbf{k}$ = unit vertical vector,

the parameters α, β and γ being predetermined. The first two terms keep the departures from the analysed fields to a minimum. Bearing in mind the fact that Φ_b and $\tilde{\mathbf{V}}$ satisfy the balance equation, the third term requires that departures of $\mathbf{V}$ and Φ from the balance equation should approximately be in geostrophic balance, the extent to which this constraint is satisfied depending on the size of γ relative to α and β. Note that near the equator the term $\mathbf{k} \times (\mathbf{V} - \tilde{\mathbf{V}})$ is negligible so that there $\mathbf{V}$ will be very close to $\tilde{\mathbf{V}}$ and the value of Φ close to $\tilde{\Phi}$, but the shape (gradients) of Φ will be close to that of Φ_b.

Minimizing I with respect to arbitrary variations of $\mathbf{V}$ and Φ with the use of the vector identity

$$\int\int\mathbf{V}\cdot\nabla(\delta\Phi)\mathrm{d}S = \int\int\nabla\cdot(\mathbf{V}\delta\Phi)\mathrm{d}S - \int\int(\nabla\cdot\mathbf{V})\,\delta\Phi\mathrm{d}S = \int(\mathbf{V}\delta\Phi)\cdot\mathrm{d}\mathbf{l} - \int\int(\nabla\cdot\mathbf{V})\delta\Phi\mathrm{d}S,$$

where $\mathrm{d}S$ is an element of area and $\mathrm{d}\mathbf{l}$ a line element, and setting $\delta\Phi = 0$ around the boundary, we obtain the equations

$$\alpha(\mathbf{V} - \tilde{\mathbf{V}}) + \gamma f\mathbf{k} \times \{\nabla(\Phi - \Phi_b) + f\mathbf{k} \times (\mathbf{V} - \tilde{\mathbf{V}})\} = 0 \quad \ldots (8)$$

$$\beta(\Phi - \tilde{\Phi}) - \nabla\cdot[\gamma\{\nabla(\Phi - \Phi_b) + f\mathbf{k} \times (\mathbf{V} - \tilde{\mathbf{V}})\}\,] = 0 \quad \ldots (9)$$

Eliminating $\mathbf{V} - \tilde{\mathbf{V}}$ from (8) and (9) yields the elliptic equation

$$\nabla\cdot(\xi\nabla\Phi) - \beta\Phi = \nabla\cdot(\xi\nabla\Phi_b) - \beta\tilde{\Phi}, \quad \ldots (10)$$

which we are required to solve for Φ. Here $\xi = \gamma\alpha/(\alpha + \gamma f^2)$.

Rearranging (8) gives

$$\mathbf{V} - \tilde{\mathbf{V}} = \frac{\gamma f}{\alpha + \gamma f^2}\,\mathbf{k} \times \nabla(\Phi - \Phi_b)$$

or, in component form,

$$u - \tilde{u} = -\frac{\gamma f}{\alpha + \gamma f^2}\frac{\partial}{\partial y}(\Phi - \Phi_b)$$

$$v - \tilde{v} = \frac{\gamma f}{\alpha + \gamma f^2}\frac{\partial}{\partial x}(\Phi - \Phi_b) \qquad \ldots (11)$$

4.3.2. *Solution of the balance equation for* Φ_b. Before equations (10) and (11) can be solved to give the final adjusted fields (Φ, u, v) it is necessary to derive the field Φ_b from $\tilde{\mathbf{V}}$ through the balance equation. The form of the balance equation used in the present scheme may be derived by taking the two-dimensional divergence of the equations of motion written in spherical polar coordinates, neglecting the vertical motion terms and setting $D = 0$ and $\partial D/\partial t = 0$, where D is the horizontal divergence.

Thus we have

$$\frac{1}{\cos^2\theta}\frac{\partial^2\Phi_b}{\partial\lambda^2} + \frac{1}{\cos\theta}\frac{\partial}{\partial\theta}\left(\frac{\partial\Phi_b}{\partial\theta}\cos\theta\right) +$$

$$+ \frac{1}{\cos\theta}\left[\frac{1}{\cos\theta}\frac{\partial}{\partial\lambda}\left(\tilde{u}\frac{\partial\tilde{u}}{\partial\lambda}\right) + \frac{\partial}{\partial\lambda}\left(\tilde{v}\frac{\partial\tilde{u}}{\partial\theta}\right) - \frac{\partial}{\partial\lambda}(\tilde{u}\tilde{v}\tan\theta) + \frac{1}{\cos\theta}\frac{\partial}{\partial\theta}\left(\tilde{u}\cos\theta\frac{\partial\tilde{v}}{\partial\lambda}\right) +\right.$$

$$\left. + \frac{\partial}{\partial\theta}\left(\tilde{v}\cos\theta\frac{\partial\tilde{v}}{\partial\theta}\right) + \frac{\partial}{\partial\theta}(\tilde{u}^2\sin\theta) + a\left\{-\frac{\partial}{\partial\lambda}(f\tilde{v}) + \frac{\partial}{\partial\theta}(f\tilde{u}\cos\theta)\right\}\right] -$$

$$- \frac{ga}{\cos\theta}\left[\frac{\partial}{\partial\lambda}\left(\frac{\partial\tilde{\tau}_\lambda}{\partial p}\right) + \frac{\partial}{\partial\theta}\left(\cos\theta\frac{\partial\tilde{\tau}_\theta}{\partial p}\right)\right] = 0, \qquad \ldots (12)$$

where a is the radius of the earth, θ and λ represent latitude and longitude and $\tilde{\tau}_\theta$ and $\tilde{\tau}_\lambda$ are the corresponding components of frictional stress. Equation (12) was solved numerically by ADI techniques (Wachspress, 1966).

The frictional terms were parametrized by the method of Lewis and Grayson (1972), taking the stress at 1000 mb to be given by

$$\tilde{\tau}_{1000} = \kappa\tilde{\mathbf{V}}_{1000}$$

and assuming a linear variation of stress with the vertical pressure coordinate to a constant zero value at 900 mb and above. Thus friction was included for the 1000 mb and 950 mb levels only, where $\partial\tilde{\tau}/\partial p$ was taken to be

$$\frac{\partial\tilde{\tau}}{\partial p} = -\frac{\kappa}{\Delta p}\tilde{\mathbf{V}}_{1000},$$

with $\kappa/\Delta p$ having values 1.2×10^{-6} and 2.4×10^{-6} m^{-1} s over sea and land respectively. These constants were derived as in Lewis and Grayson (1972) but assuming $|\tilde{\mathbf{V}}_{1000}| = 10$ m s^{-1}, $C_D = 10^{-3}$ over sea, 2×10^{-3} over land (see section 10.1 for a modification to this approach).

4.3.3. *The variational step.* Once the field Φ_b had been derived the variational step could be carried out; equation (10) was solved numerically for the adjusted field Φ by successive over-relaxation (e.g. Haltiner 1971, p. 111), after which the adjusted wind components were readily derived through equation (11). The weights α and β were taken as being inversely proportional to the estimated analysis error variance at each point. These could, of course, be obtained from the optimum interpolation (equation (7)). These parameters therefore varied over the grid. Thus where one of the analysed fields could be regarded as reliable, it would be changed only a little; where unreliable it would tend to be altered to make the constraint more closely satisfied. γ was taken as a constant. A fairly small value was chosen so that the fields were not modified except where the error variances indicated that they were particularly unreliable. Strictly γ^{-1} represents the mean square value of

$$\{\nabla(\Phi - \Phi_b) + f\mathbf{k} \times (\mathbf{V} - \tilde{\mathbf{V}})\}$$

Note that equation (11), i.e.

$$\mathbf{V} - \tilde{\mathbf{V}} = \frac{\gamma f}{\alpha + \gamma f^2}\,\mathbf{k} \times \nabla(\Phi - \Phi_b)$$

implies that when f is small, $\mathbf{V}$ is virtually independent of the corrections to the geopotential field whilst if γ were chosen to be large, the relationship would reduce to a geostrophic relationship between $(\mathbf{V} - \tilde{\mathbf{V}})$ and $(\Phi - \Phi_b)$. It should further be noted that the adjustment process was applied independently to each level.

4.4 *Overall scheme*

Figure 4 shows an outline of the overall scheme. As noted earlier the first level to be analysed is 1000 mb — this is required to provide a reference level for the SIRS data.

Next follow the 70 mb and 100 mb analyses, each followed by radiosonde corrections. Analyses at 850, 500 and 250 mb are then made simultaneously and the results at these levels are used to adjust the background fields of heights and winds at all the remaining levels, thus ensuring a degree of vertical consistency; this also reduces the number of levels at which bogus data need to be inserted when the analyses require amending on a subjective basis.

One disadvantage of the scheme was that data outside the area of analysis were not included in the analysis procedure. Since the forecast model holds boundary values constant, this omission led to excessive roughness and unrealistic features near the edges of the area during the early part of the experiment. This was controlled by introducing a smoothing of the background fields around the outermost rows of points.

4.5. *Analysis of relative humidity*

The analysis of relative humidity was done using the scheme described by Atkins (1974). It is based on Cressman's successive approximation. It uses a weighting function which depends primarily on the distance of the observation from the grid point but which is anisotropic in that it also depends on the gradient of the background field. The weighting function falls off more rapidly in directions across the contour lines of the background field than for directions along the contour lines so helping to preserve the patterns in the fields.

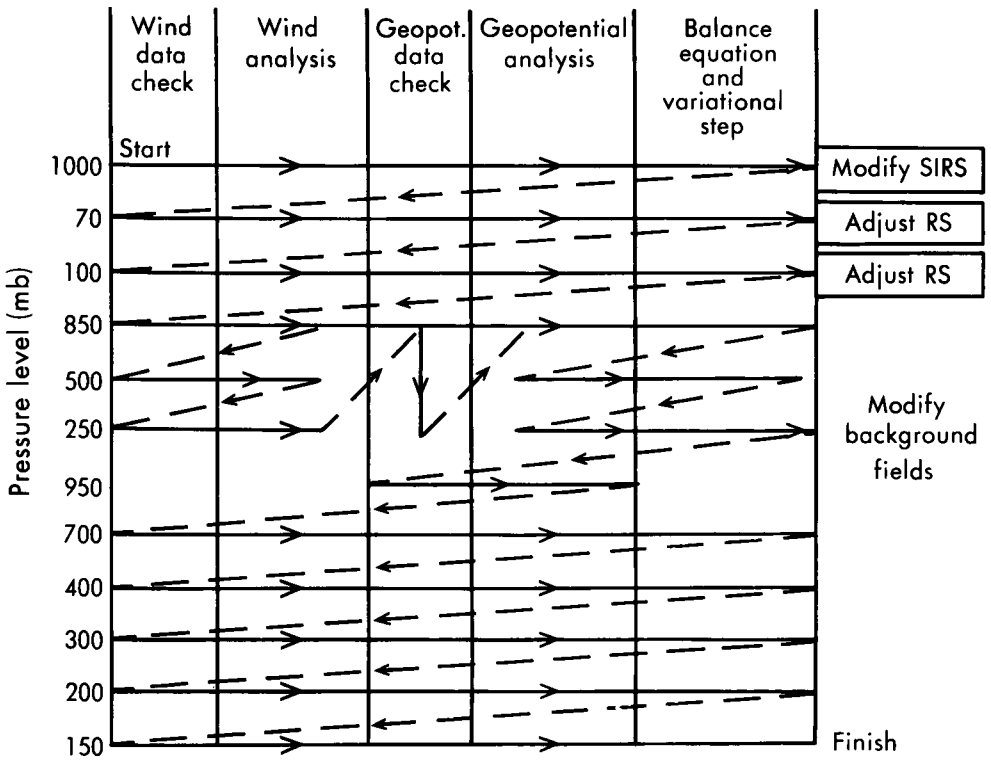

FIGURE 4. Outline of the GATE analysis scheme
RS = Radiosonde; SIRS = Satellite Infra-red Spectrometer Sounding

4.6. *Examples of analysed fields*

Figures 5–8 show examples of analyses computed during the GATE experiment.

Figure 5(a) illustrates grid-point values of wind at 850 mb and shows several features of interest in the low-level flow. Prominent among these are the easterly trade wind flow over the Atlantic, north to north-west winds over the Middle East and southerly cross-equatorial flow off East Africa. Particularly noticeable is the series of vortices stretching across Africa north of the equator and out into the Atlantic. Satellite photographs taken on this day show a band of cloud at about 5–8°N extending across much of the Atlantic in the centre of a broad convergence zone, detectable from the wind pattern. Cloud areas can also be associated with the vortices at about 14°N, 22°W and 8°N, 5°W. For comparison Figure 5(b) shows a hand-drawn streamline analysis at 850 mb; this Figure is a copy of an analysis produced at Dakar during the GATE experiment.

Figures 6(a)–(c) show more detailed comparisons of wind data and objective and subjective analyses, the latter again being made in Dakar during the GATE period. The charts are drawn for 1000 mb at 12 GMT on 2 September 1974. The objective and subjective analyses show good agreement on the broad scale, but details of the smaller-scale features such as convergence lines and centres differ. The subjective analyses are

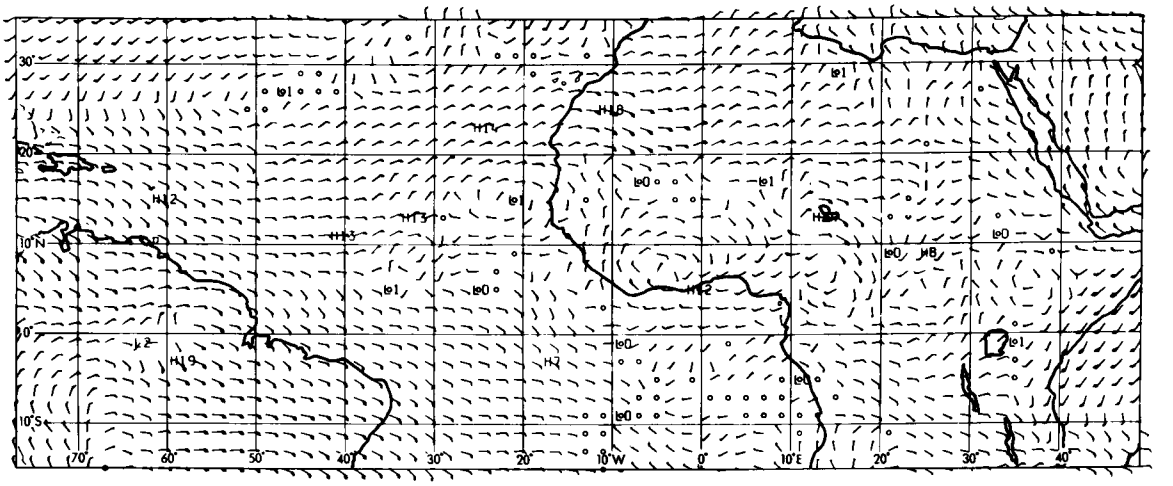

FIGURE 5(a). Objective analysis of winds at 850 mb for 12 GMT on 29 July 1974
Full feather = 5 m s^{-1}

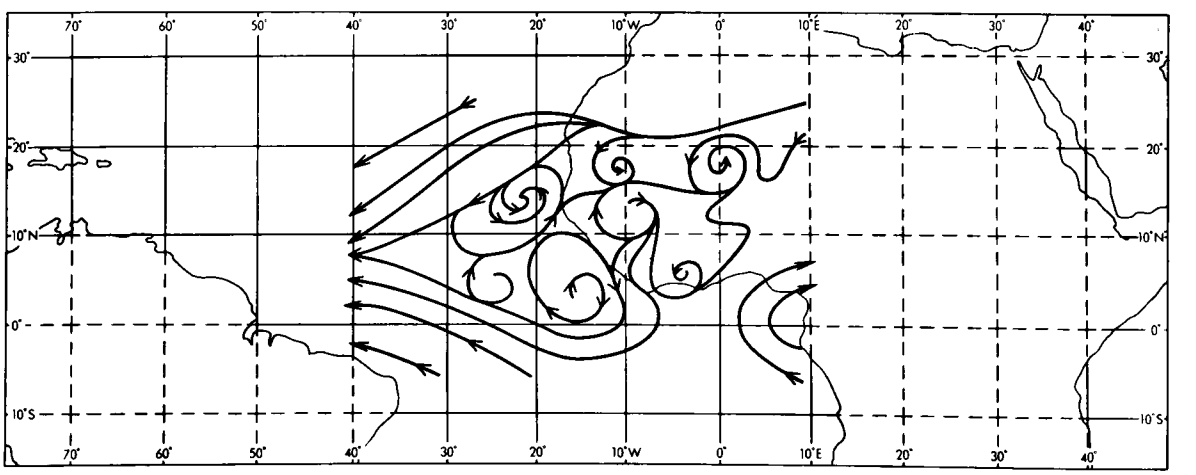

FIGURE 5(b). Hand-drawn 850 mb streamline analysis for 12 GMT on 29 July 1974

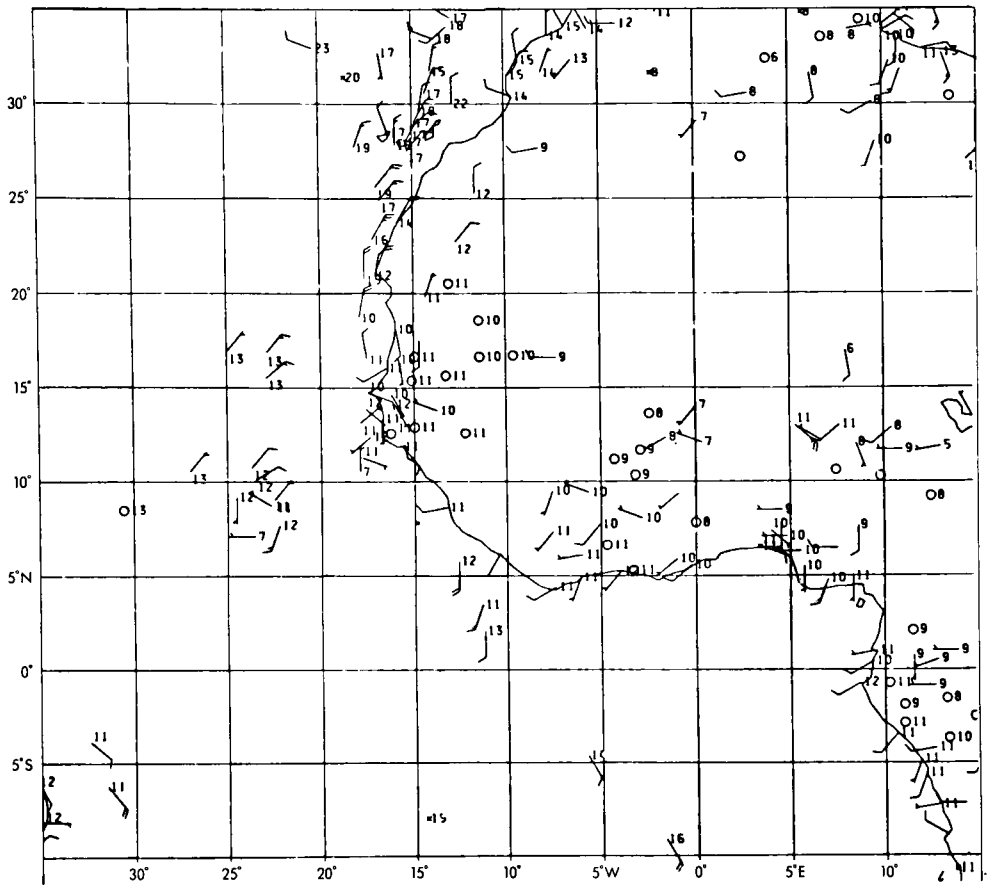

FIGURE 6(a). Data for 1000 mb at 12 GMT on 2 September 1974
1000 mb geopotentials in dagpm; full feather = 5 m s^{-1} for winds

neater and more consistent in these areas than the objective analyses, but nevertheless the latter are reasonably consistent with the existing observations. Figures 7(a) and (b) illustrate the wind and geopotential analyses at 250 mb on yet another occasion, and Figure 7(c) is the hand-drawn streamline chart for 200 mb for the central GATE area. The geopotential analysis shows slack gradients in equatorial latitudes, and there is good correlation between patterns of geopotential and wind flow beyond about 15°N.

Some comparisons of fields before and after the variational step (Figures 8(a)–(c)) show how the geopotential field is modified: the net effect was to smooth out small-scale features from the geopotential field unless they corresponded to specific features in the wind field. The independently analysed fields of wind and geopotential are shown in Figures 8(a) and (b). In Figure 8(c) the geopotential field is shown after application of the Sasaki variational step. It will be seen that geopotential gradients are much reduced, especially over equatorial regions. The centre over Venezuela, which is not represented in the wind flow and has probably originated from an isolated erroneous report, is considerably damped. Further away from the equator, some smoothing is evident in the geopotential field. The wind field has changed little so is not shown.

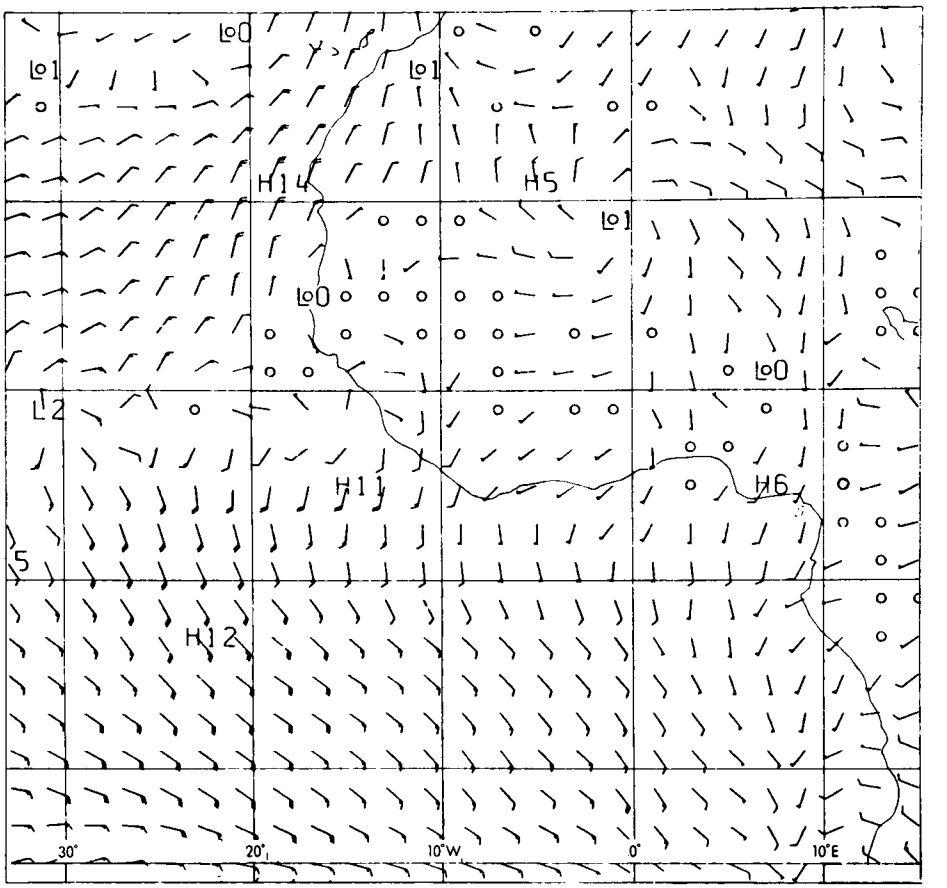

FIGURE 6(b). Part of the objective analysis of the wind field at 1000 mb for 12 GMT on 2 September 1974

Full feather = 5 m s^{-1}

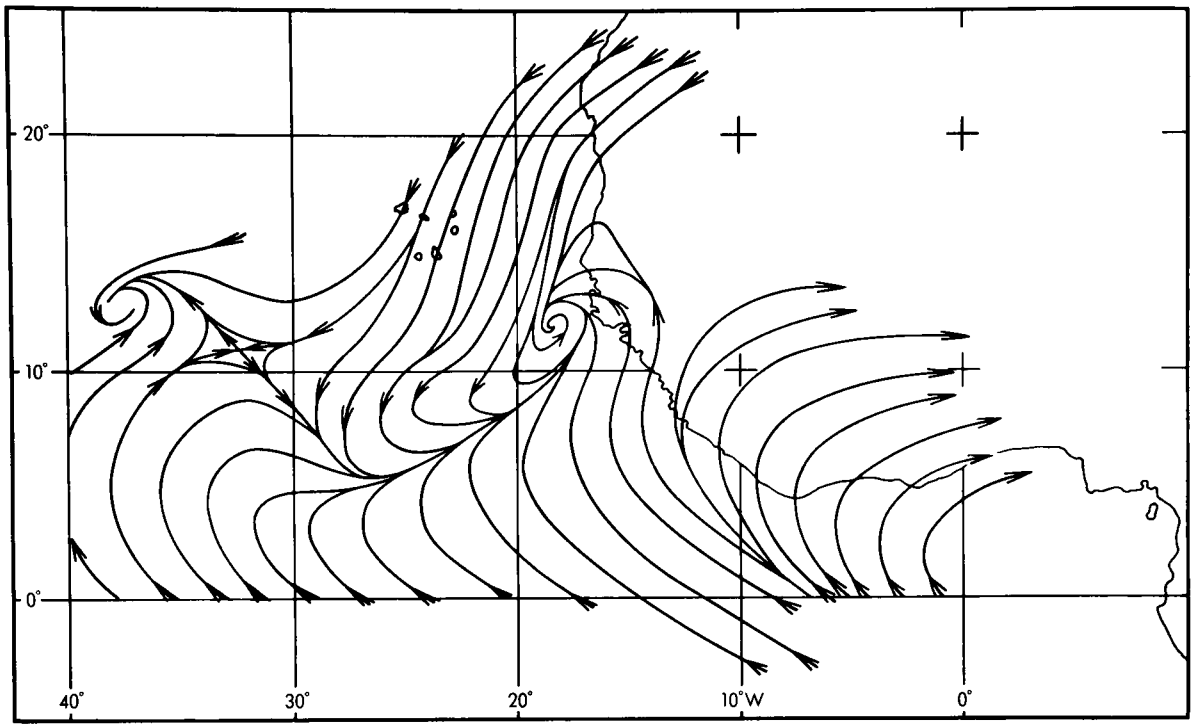

FIGURE 6(c). Subjectively analysed streamlines for 12 GMT on 2 September 1974
Surface wind over ocean; 500–600 m wind over land

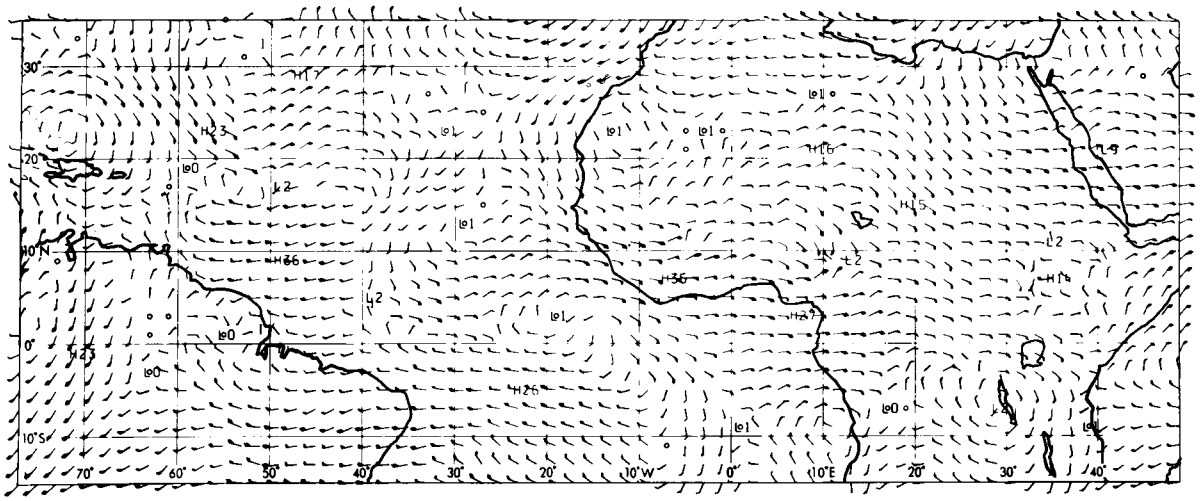

FIGURE 7(a). Objective analysis of winds at 250 mb for 00 GMT on 2 August 1974
Full feather = 5 m s^{-1}

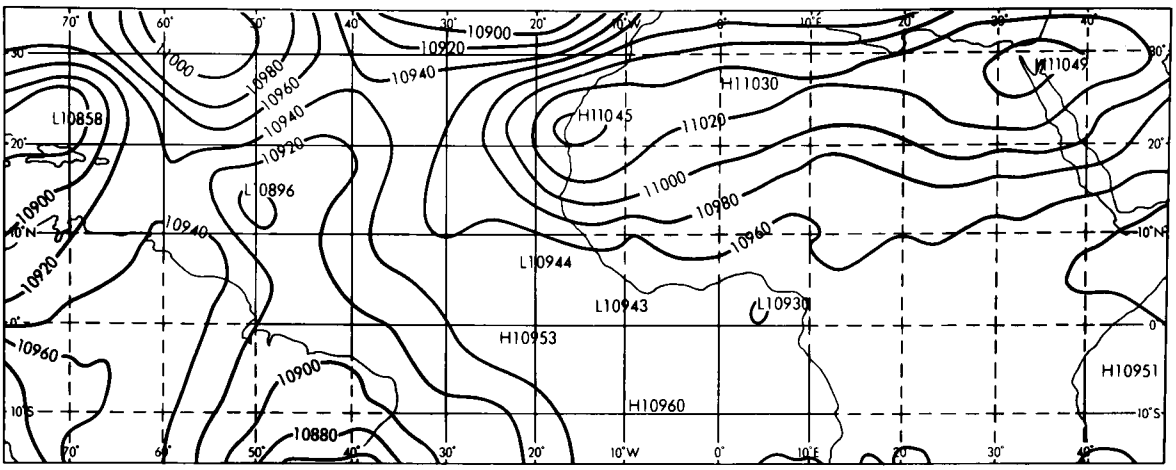

FIGURE 7(b). Objective analysis of geopotential at 250 mb for 00 GMT on 2 August 1974

Units: gpm

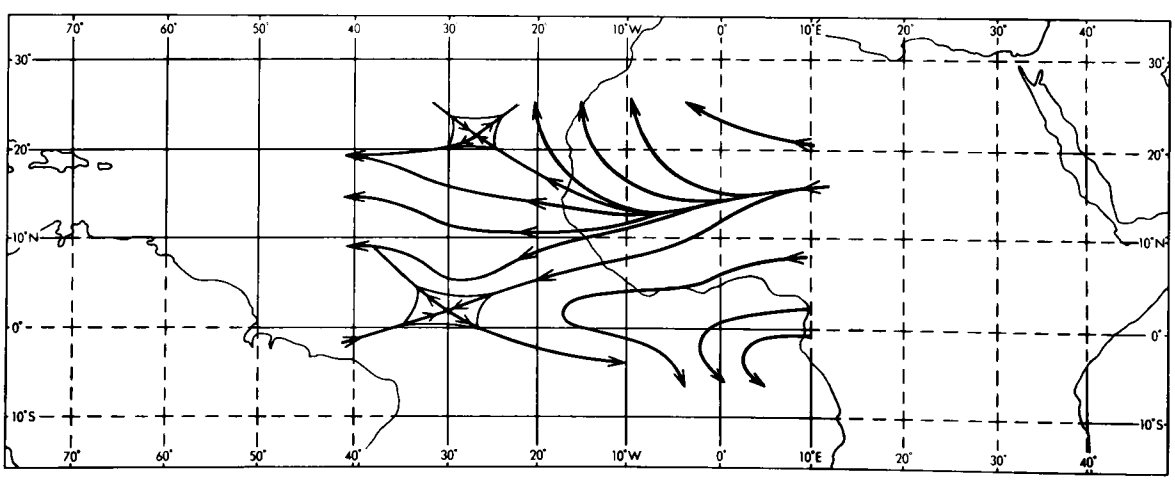

FIGURE 7(c). Hand-drawn 200 mb streamline analysis for 00 GMT on 2 August 1974

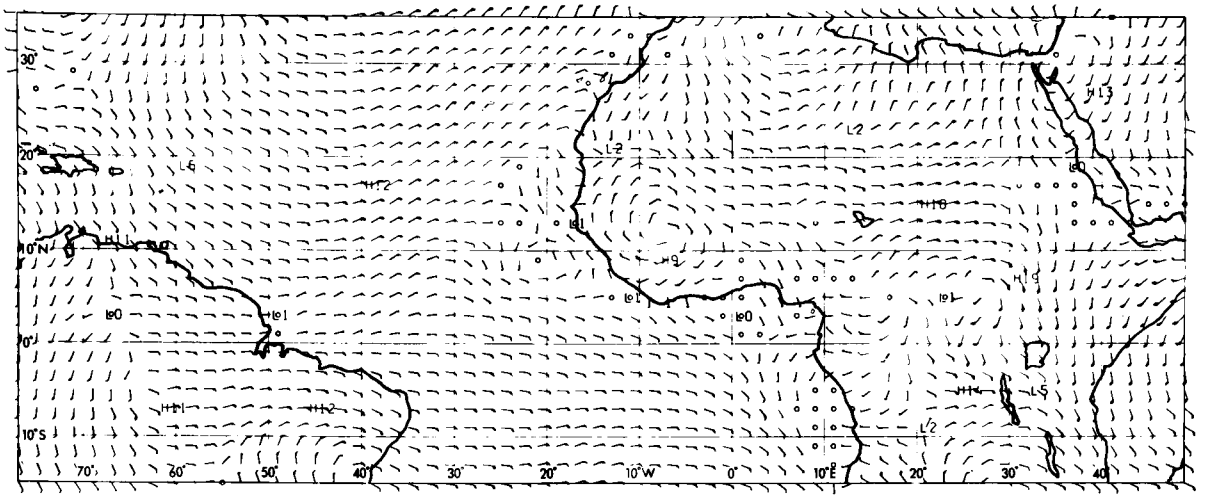

FIGURE 8(a). Objective analysis of winds at 850 mb for 12 GMT on 18 September 1974 before applying the Sasaki variational step

Full feather = 5 m s^{-1}

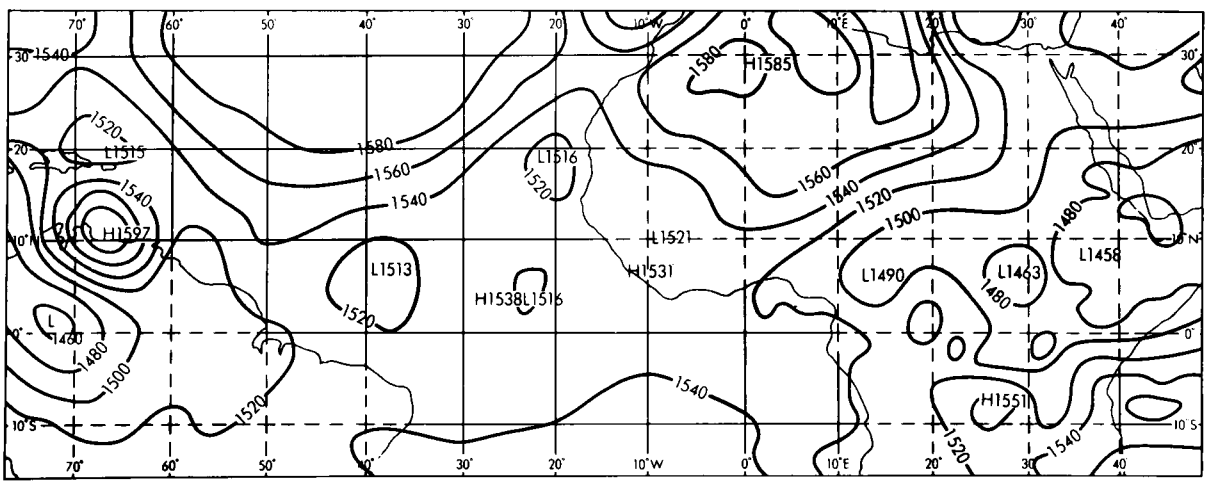

FIGURE 8(b). Objective analysis of geopotentials at 850 mb for 12 GMT on 18 September 1974 before applying the Sasaki variational step

Units: gpm

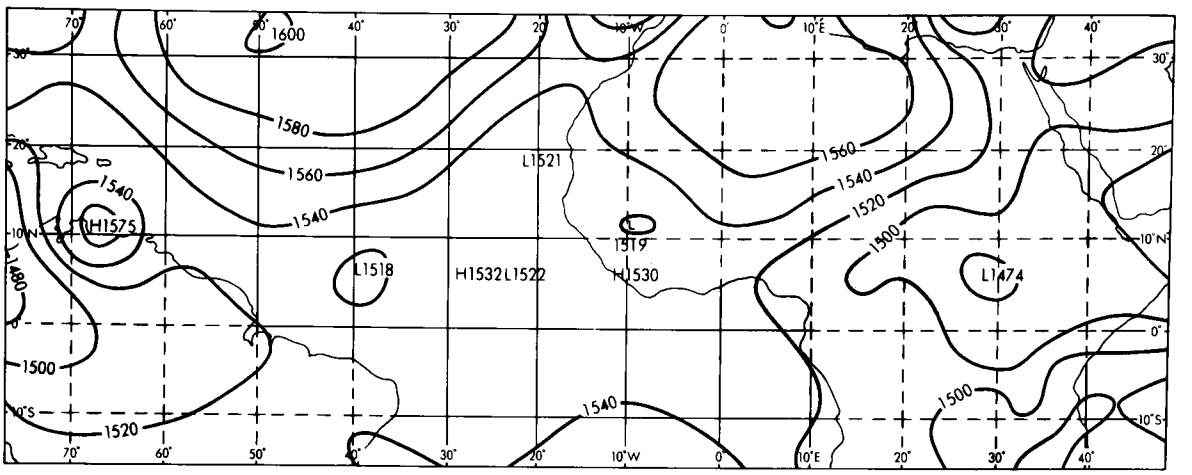

FIGURE 8(c). Objective analysis of geopotentials at 850 mb for 12 GMT on 18 September 1974 following the Sasaki variational step
Units: gpm

5. VERTICAL INTERPOLATION

by Julia M. Slingo, B.Sc. and P. R. Rowntree, Ph.D.

As explained in section 4, analyses of winds and geopotentials were prepared on pressure levels. Since the forecast model required data in σ-coordinates it was necessary to include an interpolation step.

Winds were interpolated from pressure to σ-levels using an eighth-order polynomial in the vertical. From the analysed geopotential fields, surface pressures and mean temperatures for σ-layers had to be derived. For these the method adopted was as follows:

(a) Obtain an estimate of the temperature of the surface layer by extrapolation, using a climatological lapse rate $\partial T/\partial(\ln p) \equiv \Gamma$ from the temperatures implied by the geopotentials Φ_1, Φ_2, at pressures p_1, p_2, where these are the first two analysed levels above ground.

(b) Calculate p_* using this temperature and Φ_1, Φ_2. The formula for p_* was:

$$\ln p_* = \frac{1}{2}\left\{ \ln(p_1 p_2) - \frac{2(\Phi_2 - \Phi_1)}{R_D \Gamma \ln(p_1/p_2)} \right\} \pm \frac{1}{2} \left[\left\{ -\frac{2(\Phi_2 - \Phi_1)}{R_D \Gamma \ln(p_1/p_2)} - \ln(p_1 p_2) \right\}^2 - \frac{8}{R_D \Gamma \ln(p_1/p_2)} \left\{ \Phi_* (\ln p_1 - \ln p_2) + \Phi_1 \ln p_2 - \Phi_2 \ln p_1 \right\} - 4 \ln p_1 \ln p_2 \right]^{\frac{1}{2}},$$

where Φ_* is the geopotential of the land surface.

(c) Calculate the geopotential Φ at σ-layer boundaries by interpolation with respect to $\ln p$, again assuming climatological lapse rates Γ:

$$\Phi = \Phi_1 + \frac{(\Phi_2 - \Phi_1)(\ln p_1 - \ln p)}{\ln p_1 - \ln p_2} + \frac{R_D \Gamma}{2}(\ln p - \ln p_2)(\ln p_1 - \ln p).$$

(d) Calculate mean virtual temperatures T_v for each layer and convert to actual temperatures T, where $T = T_v/(1.0 + 0.61q)$.

Some errors of the order of 1 mb remained in the calculation of surface pressure owing to the use of the dry gas constant R_D in step (b). This error could have been eliminated by use of an iterative procedure.

The interpolation step was changed during GATE as follows:

(i) To include a filtering step and zeroing of the boundary mass flux from 00 GMT on 31 July. Forecasts had previously generated area-mean surface pressure changes of up to 4 mb with deleterious effects on the analysis.

(ii) To smooth divergences using a fourth-order polynomial fit in the vertical from 00 GMT on 11 August in order to reduce the effect of spurious divergences (see (iv) below).

(iii) To remove superadiabatic lapse rates before calculating specific humidities with effect from the start of Phase III, since these were usually spurious and caused errors in the initialization step.

(iv) To remove divergences as from 12 GMT on 14 September, because these were dominated by spurious features from the previous forecast (section 8.1.3) (see also section 6.3).

Change (ii) introduced an error in the divergence in the shallow bottom layer which did not become obvious until change (iv) was made. Subsequent testing showed that the effect of this error on the predictions was negligible.

6. DYNAMIC INITIALIZATION DURING THE GATE EXPERIMENT

by C. Temperton, B.Sc.

6.1. *Introduction*

After interpolation to σ-coordinates, a period of dynamic initialization was applied to the data, with the aim of generating suitably balanced initial conditions for the forecast integration. The purpose of this section is to document the form of dynamic initialization scheme used, the changes produced by the initialization, and their effects on subsequent forecasts.

6.2. *The dynamic initialization scheme*

Initialization in the tropics is a difficult problem, largely because of the breakdown of the geostrophic relationship between mass and wind fields. Krishnamurti (1969) performed an initialization using comprehensive forms of the diagnostic balance and omega equations, but still found large unrealistic oscillations in his subsequent integration. Accordingly it seemed worth while to try dynamic rather than diagnostic initialization.

In dynamic initialization the primitive equations themselves are used to damp out high-frequency modes implied by the initial data, and hence balanced fields are obtained—indeed the absence of high-frequency modes is the simplest definition of 'balance'. Theoretical analyses of dynamic initialization usually discuss the balance obtained between mass and vorticity fields, but it can be shown (Temperton 1976) that consistent divergence fields should also be obtained, at least (in a multi-level model) for the external vertical mode of the model atmosphere.

The scheme used was that due to Nitta (1969). If the system of predictive equations is written symbolically as

$$\frac{\partial \mathbf{u}}{\partial t} = \mathscr{L}\mathbf{u},$$

where $\mathbf{u}$ is a vector representing all the variables in the model and $\mathscr{L}$ is a non-linear operator, then one cycle of Nitta's scheme is defined as follows:

$$\begin{aligned} \mathbf{u}^{*} &= \mathbf{u}^{(\nu)} + \Delta t \mathscr{L}\mathbf{u}^{(\nu)} \\ \mathbf{u}^{**} &= \mathbf{u}^{*} - \Delta t \mathscr{L}\mathbf{u}^{*} \\ \mathbf{u}^{(\nu+1)} &= 3\mathbf{u}^{(\nu)} - 2\mathbf{u}^{**} \end{aligned}$$

where ν is an iteration number. That is to say, the scheme consists of a forward timestep, followed by a backward timestep, followed by a linear combination of the latest values and the values at the end of the previous iteration. A wave of frequency W is damped by a factor $1 - 2W^2(\Delta t)^2$ by one cycle of this scheme, so that high-frequency modes are selectively damped.

In some applications of dynamic initialization, one of the variables (for example the mass field or the wind field) is restored at the end of each cycle, in order to force the remaining variables into balance with it. However, theoretical considerations (see for example Økland 1972) show that for a multi-level model, both mass-to-wind and wind-to-mass adjustments are to be expected among the various vertical modes and horizontal scales. Accordingly, all the variables were allowed to adjust mutually during the course of the initialization.

During the initialization the moisture field was held fixed, and all sources and sinks of energy (including latent heat release) were ignored. This is rather unsatisfactory — in particular, the balance in the lowest levels of the model should be influenced by frictional terms — but unfortunately no method has yet successfully incorporated source/sink terms into this type of dynamic initialization scheme. Experience with the initialization of a hemispheric model (Temperton 1976) suggested that the omission of sources and sinks may not be important.

One extra effect was, however, incorporated: at the end of each cycle a dry convective adjustment was applied to the temperature fields, to prevent the generation of vertical instabilities by the initialization. This dry convection was the same as that used in the model except that the maximum mass transfer was limited to half the mass of the lower layer as from 29 August.

During the initialization the same lateral boundary conditions were applied as during the forecast integrations, that is to say the boundary values were held fixed, and the time-tendencies of each variable were damped at all points within three grid lengths of the boundary (see section 7.2). The timestep Δt was chosen to be 450 seconds, so that 4

cycles of the scheme, involving eight model timesteps, were equivalent to one hour's forward integration. During Phase I of the GATE experiment, initialization was applied for 96 cycles (24 hours), but for Phases II and III this was reduced to 24 cycles (6 hours).

6.3. *Changes due to initialization in the fields of the basic variables*

The changes to the fields of basic variables produced by the initialization procedure are small. The root-mean-square changes in each fundamental variable during the five initialization runs, each of 24 cycles (6 hours) for 12 GMT on 9–13 September 1974 inclusive, are shown in Table III. Changes on individual days were similar in magnitude and vertical distribution. Before initialization, the fields were to some extent diagnostically balanced, since, as discussed in section 4.3, the analysis routine included a variational step with the balance equation as a constraint. During this period the wind field as analysed and interpolated to σ-surfaces before initialization included a vertically smoothed divergent component. An unfortunate side-effect of this procedure was that small areas of anomalously large divergence, generated during the forecast, tended to influence the next analysis via the background field, and thus persist into the following forecast. On 14 September 1974 the analysis/interpolation scheme was changed in an attempt to remove the divergence altogether from the analysed wind field. (The fields did not become entirely non-divergent because of the difficulty of separating a wind field into its rotational and divergent components on a grid with u and v defined at the same set of points; in fact the magnitude of the residual divergence was such that the effect of the initialization procedure was still to reduce it.) As a result of this change, the root-mean-square vector wind changes during the initialization procedure became even smaller, by a factor of around two.

TABLE III. *Root-mean-square changes due to initialization, 9–13 September 1974*

Level	11	10	9	8	7	6	5	4	3	2	1	all	surface
V (m s^{-1})	0.44	0.43	0.41	0.36	0.30	0.32	0.45	0.55	0.63	0.63	1.03	0.55	
T (K)	0.60	0.27	0.34	0.31	0.16	0.12	0.07	0.04	0.06	0.09	0.12	0.26	
p_* (mb)													0.57

Figure 9 illustrates the typical changes produced by 6 hours of initialization on a rerun of the 10 September analysis with the modifications described above included. The changes to the temperature field at level 6 ($\sigma = 0.436$) and the surface pressure field are shown. It will be seen that the changes form a coherent pattern; the small areas of larger temperature changes are probably due to convective rather than to dynamic adjustment. The changes in the surface pressure field show evidence of adjustment to the imposed boundary conditions. The centres of pressure change at 7°S, 25°W and 5°S, 23°E correspond respectively to the filling and deepening of surface lows in the analysis; most of the other centres of change correspond to the adjustment of gradients between surface features.

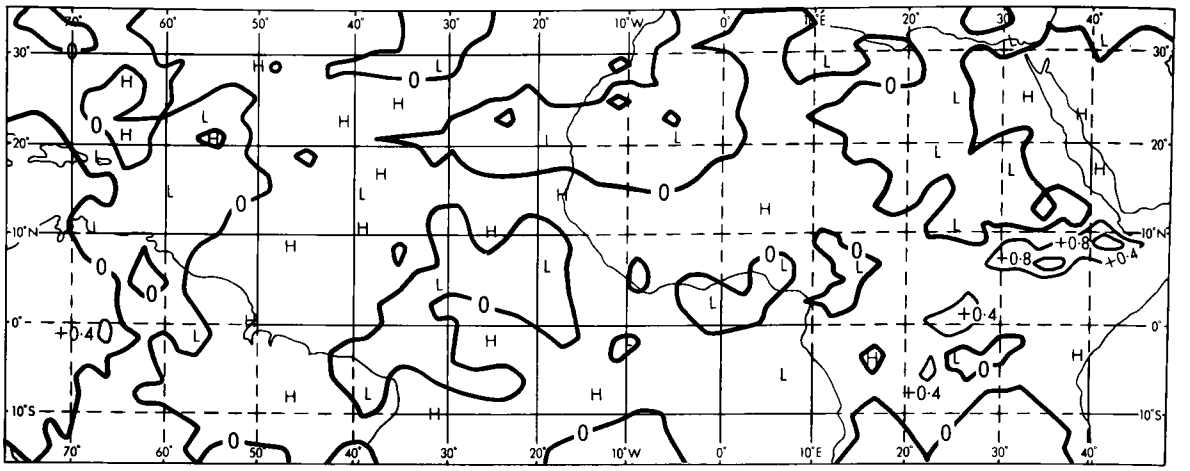

FIGURE 9(a). Change in temperature at level 6 ($\sigma = 0.436$) resulting from 6 hours of initialization
Units: K

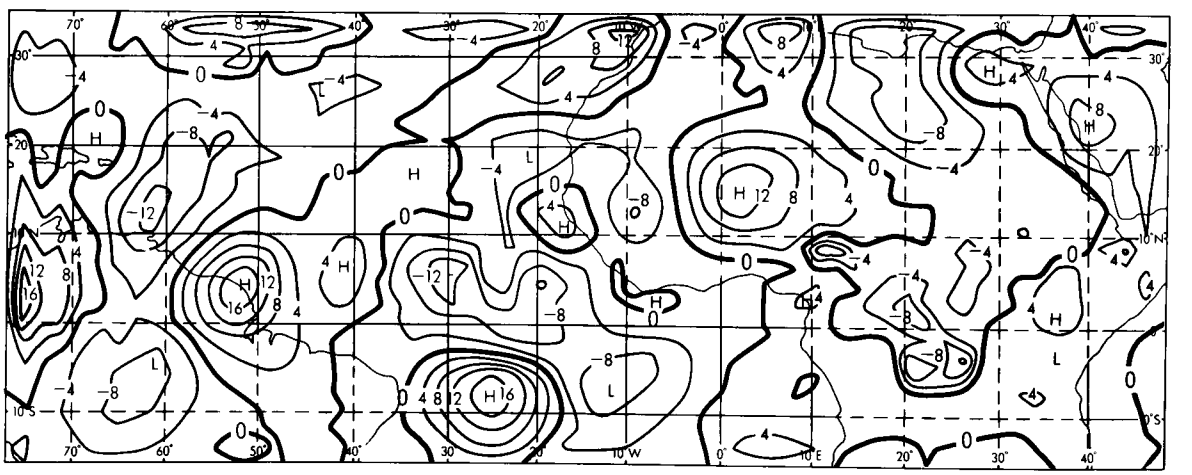

FIGURE 9(b). Change in surface pressure after 6 hours of initialization
Units: mb $\times 10^{-1}$

6.4. *Effects of different initialization periods on initial and forecast fields*

In order to study the effects of different initialization periods, three 12-hour forecasts were run, all starting from data for 12 GMT on 10 September 1974: one with no dynamic initialization at all, one after 6 hours of initialization (the period used during most of the GATE experiment), and one after 24 hours of initialization. All three experiments were run using the same forecast model as was used during Phase III of the GATE experiment, incorporating the full range of physical parametrizations.

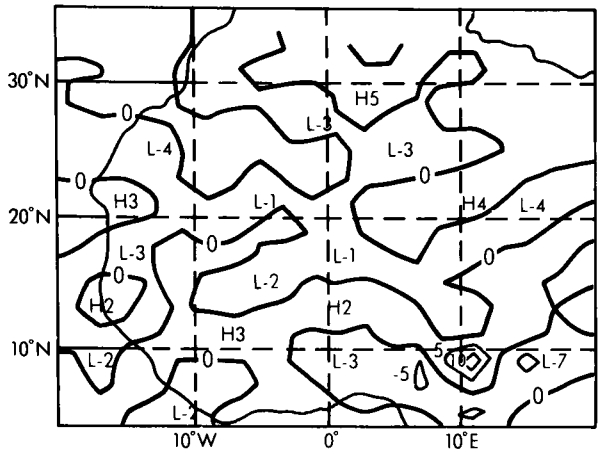

FIGURE 10(a). Initial field of divergence at level 5 ($\sigma = 0.317$)
Units: 10^{-6} s^{-1}

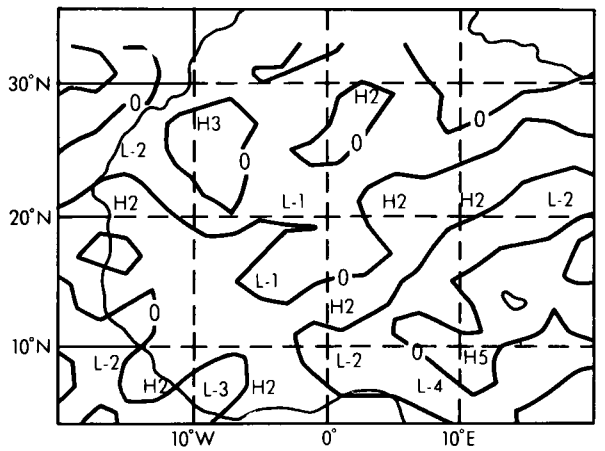

FIGURE 10(b). Initial field of divergence at level 5 ($\sigma = 0.317$) after 24 hours of initialization
Units 10^{-6} s^{-1}

As outlined in section 6.3, dynamic initialization resulted in rather small changes in the fields of basic variables. Also of interest, however, are the differential properties of the wind field; for instance (see, for example, Philips 1960) it is known that the divergence field, which is difficult to estimate diagnostically, must be correctly specified in order to achieve balanced initial conditions for a forecast. Figure 10 shows the divergence at level 5 ($\sigma = 0.317$) after 0 and 24 hours of initialization*. In fact there is little change, except that the field does become a little smoother as the initialization proceeds. In examining the effects of dynamic initialization, it is important to remember that a particular level is affected by all the vertical modes, of which there are as many as there are levels in the model. It is known (Temperton 1976) that dynamic initialization should balance the external vertical mode of a multi-level model quite successfully, but that balance will not be achieved for the internal modes of high vertical wave number and low frequency. The external mode is closely associated with the vertically integrated divergence $\partial p_*/\partial t$ and it is this quantity which is shown in Figure 11 for the cases of 0 and

*Only a limited area is shown in this and some subsequent charts because of the dominance of small-scale features and consequent similarity of different parts of the fields.

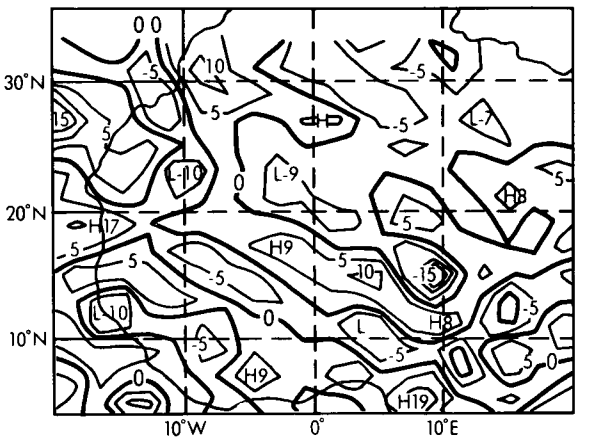

FIGURE 11(a). Initial field of $\partial p_*/\partial t$ —no initialization
Units: 0.1 μb s^{-1}

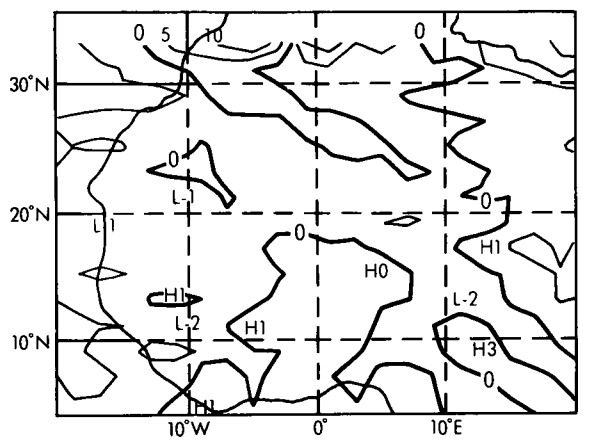

FIGURE 11(b). Initial field of $\partial p_*/\partial t$ after 6 hours of initialization
Units: 0.1 μb s^{-1}

6 hours of initialization. Here we see a dramatic change, from an incoherent field before initialization to a relatively coherent field after 6 hours of initialization, with values an order of magnitude smaller. Extension of the initialization period to 24 hours showed little further change, however. It is clear that external gravity waves were implied in the originally analysed data, and that these have been successfully removed after 6 hours of dynamic initializaton.

Turning now to the subsequent forecasts, it might of course be feared that gravity waves present in uninitialized fields would interact with the meteorological mode, particularly in the presence of highly non-linear physical effects such as latent heat release, and lead to rapidly amplifying errors in the forecasts. However, it was difficult to find any evidence of this in the fields of basic variables, or in the divergence fields for the 10 September case, during 12-hour forecasts (or even 24-hour forecasts) starting from data initialized for 0 and 24 hours. The only significant difference was that the forecast fields from initialized data were slightly smoother. On the other hand the forecast fields of $\partial p_*/\partial t$ showed the non-initialized forecast to be contaminated by external gravity waves (though interestingly their amplitude had been somewhat reduced) while the initialized forecast remained free of external gravity waves, except in the immediate neighbourhood of the boundaries.

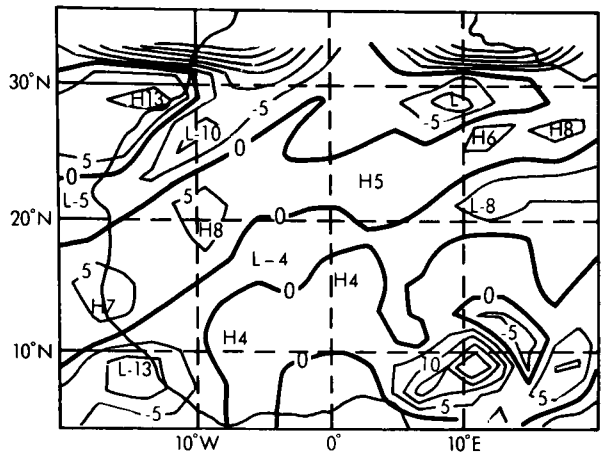

FIGURE 12(a). Forecast field of divergence at level 5 ($\sigma = 0.317$)—no initialization
Units: 10^{-6} s^{-1}

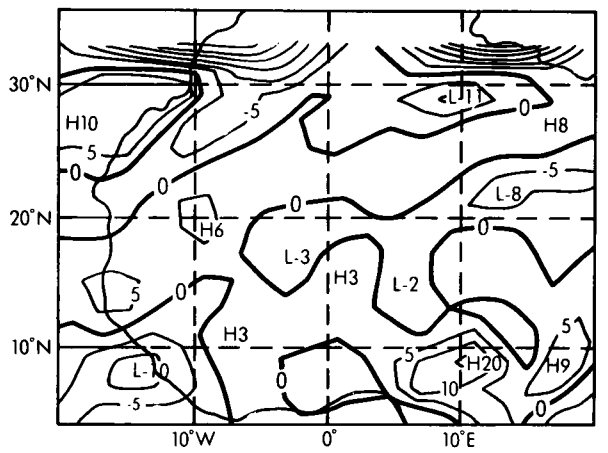

FIGURE 12(b). Forecast field of divergence at level 5 ($\sigma = 0.317$) after 24 hours of initialization
Units: 10^{-6} s^{-1}

One forecast quantity which might also be expected to be sensitive to the presence of gravity waves, and to changes in the initial conditions, is the total rainfall. However, the accumulated 12-hour rainfall patterns for each of three forecasts after 0, 6 and 24 hours of initialization (not shown) are remarkably similar, the main differences being that the rainfall maxima tend to be slightly reduced in the initialized cases, particularly after 24 hours of initialization.

Finally, comparison of Figures 12(a) and (b) with Figures 10(a) and (b) shows that the intensity of the divergence field grew during the course of the forecasts, implying that the initialization fails to generate the magnitude of divergence required by the forward integration. This is partly due to the inability of dynamic initialization to treat the low-frequency internal modes of the model atmosphere successfully, and partly due to the presence of physical processes in the forecast which are ignored during the initialization. To demonstrate this, an additional model run was carried out with minimal physics, consisting only of dry convection and boundary-layer friction and with 24 hours' initialization. Although patterns were very similar over much of the chart, intense local divergences generated over Africa during the forecast with full physics were completely absent in the run with minimal physics.

7. FORECAST MODEL

by W. H. Lyne, Ph.D and P. R. Rowntree, Ph.D.

The forecast model used in the GATE modelling experiment was developed from the 11-layer global model described by Saker (1975). The forecast domain, like the analysis area, extended from 15°S to 35°N, and from 77°W to 49°E, the boundaries being located so as to allow 48-hour forecasts in the region of the B-scale ship array (8½°N, 23½°W) with little chance of significant errors resulting from advection of air from the boundaries. The model orography was obtained by linear interpolation from that of the 5-layer global model described by Corby *et al.* (1977), which was obtained from that of Berkofsky and Bertoni (1960). This orography was modified near the western boundary after Phase I to remove the Andes, which had been causing spurious behaviour there. Heights were set to zero at 69°–77°W and halved at 67°W. With few observations in this region it seemed unlikely that a more realistic representation was worth while. The topography used is shown in Figure 13 together with the sea surface temperatures which were based on means for August in publications of the US Naval Oceanographic Office (1967) and the Meteorological Office (1948).

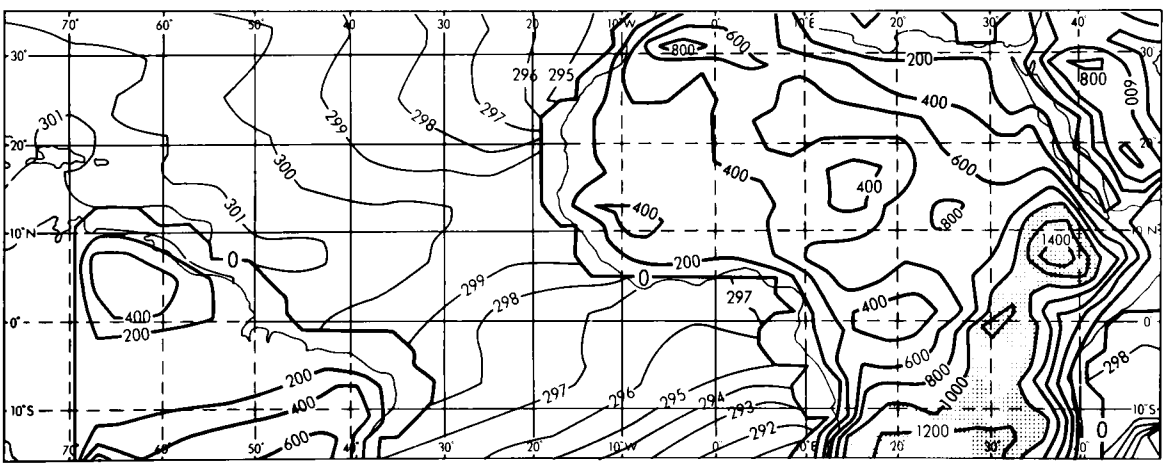

FIGURE 13. Land topography (gpm) and sea surface temperature (K)
Stippled areas show land higher than 1000 gpm

The horizontal finite difference scheme is identical to that in the 5-layer hemispheric model of Corby, Gilchrist and Newson (1972). In the vertical there are 11 layers: the layer boundaries and nominal central values are given in Table IV. This vertical resolution is chosen to give:

(a) A higher resolution near the surface to give a better representation of the temperature and humidity gradients needed for modelling the surface fluxes of the boundary layer and of the inflow into tropical convective systems.

(b) A vertical resolution of extratropical fronts consistent with the horizontal resolution.

(c) A consistent resolution of the jet stream in the sense of (b) and adequate representation of outflow from tropical convective systems.

(d) One layer wholly in the stratosphere to provide a stable lid on tropospheric vertical motions.

TABLE IV. *Layer boundaries and nominal levels in σ-coordinates*

Layer Number	11	10	9	8	7	6	5	4	3	2	1
Boundaries (σ)	1	0.975	0.9	0.79	0.65	0.51	0.37	0.27	0.195	0.125	0.06	0
Nominal level (σ)	0.9874	0.9370	0.8438	0.7177	0.5772	0.4363	0.3174	0.2305	0.1574	0.0886	0.0221	

Because the layers are of unequal mass, the vertical differencing is modified from that of Corby *et al.* (1972) to maintain energy conservation so that equations (7) and (10) of that paper become (with R_m replacing R):

$$\Phi_k = \Phi_* + \sum_{i=k+1}^{11} \left[R_m T_i \ln\left(\frac{\sigma_{i+\frac{1}{2}}}{\sigma_{i-\frac{1}{2}}}\right)\right] + \mu_k R_m T_k \ln\left(\frac{\sigma_{k+\frac{1}{2}}}{\sigma_{k-\frac{1}{2}}}\right),$$

$$-\left(\frac{\kappa_m T\omega}{\sigma}\right)_k = \frac{\kappa_m}{a\cos\theta}\left[\overline{U\overline{T}^{\lambda}\delta_\lambda \ln p_*}^{\lambda} + \overline{V\cos\theta\overline{T}^{\theta}\delta_\theta \ln p_*}^{\theta}\right]_k -$$

$$-\frac{\kappa_m T_k}{\sigma_k}\sum_{i=1}^{k+1}(\nabla\cdot\mathbf{V}_i)\,\sigma_i \ln\left(\frac{\sigma_{i+\frac{1}{2}}}{\sigma_{i-\frac{1}{2}}}\right) + \nu_k\,(\nabla\cdot\mathbf{V}_k)\sigma_k \ln\left(\frac{\sigma_{k+\frac{1}{2}}}{\sigma_{k-\frac{1}{2}}}\right)$$

where

$$\nabla\cdot\mathbf{V}_i = \frac{1}{a\cos\theta}\left(\delta_\lambda \overline{U}_i^{\lambda} + \delta_\theta \overline{V}_i^{\theta}\cos\theta\right)$$

It can be shown that energy is conserved if $\mu_k = \nu_k$ and $\Delta\sigma_k = \sigma_k\,\Delta ln\sigma_k$, the latter defining the nominal central values σ_k of the layer (Table IV). For the top layer $\Delta \ln\sigma$ is not defined, but by taking $\sigma_1 = e^{-1}\,\sigma_{1\frac{1}{2}}$, a constant divergence throughout the layer is implied. The μ_k and ν_k are chosen so that

$$\mu_k = \nu_k = \ln\left(\frac{\sigma_{k+\frac{1}{2}}}{\sigma_k}\right) \Big/ \ln\left(\frac{\sigma_{k+\frac{1}{2}}}{\sigma_{k-\frac{1}{2}}}\right),$$

which gives an exact estimate of Φ at σ_k and a reasonable estimate of ω/σ.

The values of T, q, U and V at layer boundaries used in calculating vertical flux divergences are defined by

$$X_{k+\frac{1}{2}} = W_{k+\frac{1}{2}}X_k + (1 - W_{k+\frac{1}{2}}X_{k+1}),$$

where X represents one of T, q, U or V and where the weights $W_{k+\frac{1}{2}}$ are equal to 0.5 for q, U and V. The weights for T are chosen so that, with a dry adiabatic lapse rate, ascending motion produces no temperature change; they are given in Table V.

TABLE V. *Weights for vertical differencing of T*

Level	$10\frac{1}{2}$	$9\frac{1}{2}$	$8\frac{1}{2}$	$7\frac{1}{2}$	$6\frac{1}{2}$	$5\frac{1}{2}$	$4\frac{1}{2}$	$3\frac{1}{2}$	$2\frac{1}{2}$	$1\frac{1}{2}$
Weights	0.246	0.394	0.422	0.476	0.469	0.551	0.542	0.482	0.464	0.378

The weights for q can be chosen so that with a saturated adiabatic lapse rate ascending motion produces no temperature change; this was not done during GATE but subsequent experimentation showed that such a change makes no significant difference.

Other departures from Corby *et al.* are (a) the use of the moist gas constant and ratio of specific heats defined by

$$R_m = (1 + 0.61q)R_D \text{ and } \kappa_m = \left(\frac{1 + 0.61q}{1 - 0.8q}\right)\kappa_D,$$

where R_D and κ_D correspond to dry air, and (b) the use of continuous time-meaning in the leap-frog time-stepping procedure to avoid time-splitting as in Francis (1975). Thus

$$\hat{f}_t = f_t + 0.0005(f_{t+\Delta t} - 2f_t + \hat{f}_{t-\Delta t}),$$

where f_t is any parameter at time t and $\hat{f}_t$ is the time-meaned value. A time step of $7\frac{1}{2}$ minutes is used in the model.

7.2 *The boundary conditions*

The boundary conditions in the vertical are $\dot{\sigma} = 0$ at $\sigma = 0$ and 1. Specification of the lateral boundary conditions requires more consideration. After some experimentation it was found that the 'sponge' conditions of Kesel and Winninghoff (1972) and Perkey and Kreitzberg (1973) were both simple and effective, and they were adopted at both zonal and meridional boundaries. The tendencies calculated in the boundary row ($i = 0$) and the first to third rows ($i = 1, 2, 3$) are multiplied by S_i, where $S_0 = 0$, $S_1 = 0.3827$, $S_2 = 0.7071$ and $S_3 = 0.9239$. The coefficients are arbitrary; these particular values are generated by the function

$$S_i = \cos[\pi(4 - i)/8] \qquad i \leq 3$$

but experiments show that the forecasts are relatively insensitive to the exact choice. In a corner the coefficients are defined by $S_{ij} = S_iS_j$.

One shortcoming of these conditions is the generation of two-gridlength waves, which, although not affecting the forecast significantly, give rise to roughness in the fields. This feature, however, was shared by other conditions tested and is removed by the use of the filter described below.

7.3 *The filter*

Instead of the nonlinear diffusion used in Corby *et al.* (1972), it was decided to use a filter to effect the complete removal of the two-gridlength waves, as described by Shapiro (1971) and Francis (1975). The maximum order of the filter is eight (involving 17 grid points) both in the meridional and zonal directions, and the same filtering operators are used in these directions as by Francis (1975). As the boundaries of the grid are approached, the order N_i of the filter is reduced progressively in the direction normal to the boundary so that $N_i = i$, with i defined as in section 7.2. The order of the filter in the tangential direction is not changed.

The fields which are filtered are pressure at mean sea level p_0 (see below), horizontal wind components, a linear combination of temperature T and potential temperature Θ, $bT + (1 - b)\,\Theta$ and specific humidity q. The coefficients b are chosen to give zero vertical gradients of $bT + (1 - b)\,\Theta$ at each level for the mean tropical atmosphere during July, August and September (Oort and Rasmusson 1971). The values are given in Table VI.

TABLE VI. *Coefficients for filtering* $bT + (1 - b)\Theta$

Level	11	10	9	8	7	6	5	4	3	2	1
b	0.4357	0.4990	0.5025	0.4455	0.4382	0.3643	0.2745	0.5258	0.6470	1.1196	1.1196

This eliminates roughness caused by filtering on sigma surfaces near mountains. Mountains also require the filtering of p_0 rather than p_*. Although it may be argued that pressure should not be filtered, since the filter can be regarded as modelling a diffusive process, it was found impossible to exclude it owing to roughnesses generated by the boundary conditions. p_0 is related to p_* by the formula

$$p_0 = p_* \exp\{\Phi_*/R_m(T_{11} + \gamma_c\Phi_*/2)\},$$

where γ_c is a typical lapse rate for the mean tropical atmosphere (Oort and Rasmusson 1971) and Φ_* is the geopotential of the surface. To recover p_* from the filtered p_0 the unfiltered values of T_{11} have to be used but this reintroduces very little roughness into the pressure field. In the experiments described here, the denominator 2 in the above equation was omitted; the effects of this are insignificant.

During GATE, the filter was applied to the fields at both time levels carried by the model, but not at every time step since it was felt that this might lead to too much damping of the meteorological modes as well as being computationally expensive. An intermittent application having been decided on, it became clear that there is considerable virtue in applying it as little as possible since each application throws the variables temporarily out of balance. Therefore the filter was applied only at six-hourly intervals (forecast time) so ensuring that output fields are relatively smooth. The fields were also filtered before and after initialization.

7.4 *Boundary layer*

The boundary layer formulation is based on Clarke's (1970) Method I. Clarke derives expressions for the surface flux of momentum, upward flux of sensible heat, H and potential evaporation E_p as functions of the dimensionless parameters z_m/λ_u and z_m/z_0, where z_m is the height of the centre of the lowest model layer (assumed to be 100 m), z_0 is the roughness length, and

$$\lambda_u = u_{11}^2/[g(\delta_0\Theta/\Theta_{11} + 0.61\delta_0 q)]$$

A subscript 11 refers to the lowest level of the model and $\delta_0\Theta$, $\delta_0 q$ *are the differences between* Θ, q at the lowest level and at the surface. The surface value of specific humidity q_0 is taken to be the saturated value at the surface temperature T_0. The roughness lengths are assumed to be

$$z_0 = \begin{cases} 10 \text{ cm over land} \\ 0.032\, u_*^2/g \text{ cm over sea,} \end{cases}$$

where the expression for z_0 over sea is due to Charnock (1955). The relation between actual evaporation E_v and potential evaporation E_p is based on the work of Priestley and Taylor (1972) and is

$$E_v = E_p \text{ if soil moisture content (SMC)} \geqslant 5 \text{ cm}$$

$$E_v = \frac{\text{SMC}}{5} E_p \text{ if soil moisture content} < 5 \text{ cm.}$$

While in general the model's soil moisture content is variable and affected by rainfall and evaporation, in the GATE modelling experiments it was kept fixed since it was considered that rainfall amounts would not be reliable enough. The fixed soil moisture contents were as in Table VII over Africa north of 12°N and 5 cm elsewhere. The Phase II and III values were chosen to give a steady decrease in evaporation from the moist region to the dry region. Those used in Phase I gave an abrupt decrease from 17° to 19°N. The values used later could be further improved to take account, for instance, of the aridity of Africa and South America south of the equator during northern summer.

TABLE VII. *Soil moisture content (cm) used over Africa*

Latitude (°N)	11	13	15	17	19
SMC (Phase I)	5	5	3.33	1.67	0
SMC (Phases II and III)	5	1	0.3	0.1	0

The thermal capacity of the land surface was assumed to be equivalent to 5 cm of water, i.e. 2.1×10^5 J m^{-2} K^{-1}.

In our use of Clarke's formulation the vertical mixing through the lowest three layers of the model is computed on a mixing-length hypothesis with an eddy diffusion coefficient K such that

$$K = l^2 \left| \frac{\partial \mathbf{V}}{\partial z} \right|$$

When no convection is occurring the mixing length is assumed to be the same for momentum, heat and water vapour, and the Obukhov length is as defined by Clarke. However, the scaling length L_* is redefined as

$$L_* = \min(10^4, u_*/f),$$

which avoids the discontinuity Clarke introduced at latitude 7°.

It is assumed that if the lowest two layers are convectively unstable then both temperature and water vapour are mixed entirely by the convection scheme with only the momentum being mixed by diffusion. The parameter representing the height of the highest level involved in the convection is set to 515 m or 1360 m as appropriate and is used to define the mixing lengths $l_{10\frac{1}{2}}$ and $l_{9\frac{1}{2}}$ in the way suggested by Clarke. When there is no convection Clarke's suggested formulae are used but in both cases the mixing lengths are restricted to

$$l_{10\frac{1}{2}} \leqslant 25 \text{ m}$$

$$l_{9\frac{1}{2}} \leqslant 200 \text{ m}$$

in order to maintain numerical stability.

The friction terms in the momentum equation are written:

$$\frac{\partial \mathbf{V}}{\partial t} = -\frac{g}{p_*}\frac{\partial \tau}{\partial \sigma}$$

where

$$\tau = -\rho K \frac{\partial \mathbf{V}}{\partial z}$$

and in finite difference form this can be expressed (for the u-component):

$$u_k = u_k' - 2\Delta t \delta_\sigma \{(g/\Delta\Phi)^3 l^2 |\Delta \mathbf{V}| \Delta u \Delta \sigma\}_k$$

where u_k' is the value of u at the kth grid point and time t after the model has been integrated from $t - \Delta t$ to $t + \Delta t$ by the dynamical equations, and $\Delta X_{k+\frac{1}{2}} = X_{k+1} - X_k$, etc. Similar equations can be derived for the thermodynamic and moisture equations and for the v-component.

7.5. *Radiation*

A simple radiative parametrization was used for GATE. The atmospheric radiative heating is $c_0 S - R$, where S and R are mean daily heating and long-wave cooling rates based on Rodgers (1967) and Dopplick (1970). $c_0 S - R$ is taken as zero for the top three layers; S, R are otherwise as given in Table VIII; c_0 is a diurnal variation coefficient which varies as a sine function with maximum at 12 hours local time but which is zero at night and scaled to give an average value of unity. The surface heating is $c_0 S_G - \epsilon_* \sigma_0 T_0^4$. Here S_G is the net downward solar flux, given in Table VIII, based on observed solar radiation (Thompson, 1965) and estimated albedo over Africa in July; σ_0 is Stefan's constant, T_0 the surface temperature and ϵ_* an effective surface emissivity dependent, through a relation based on the results of Rodgers (1967) (Rowntree 1975), on climatological 850 mb specific humidity and cloudiness. The cloudiness data were obtained from IGY data mapped for the northern hemisphere by Lobanova (1967) and

tabulated for the southern hemisphere by Kravcova (1968). For observed near-surface temperatures, the net downward radiation was about 130 W m^{-2}, varying remarkably little with latitude.

TABLE VIII. *Radiative constants used in the tropical model (values were linearly interpolated between tabulated values)*

Latitude	40°N	30°N	20°N	10°N	0	10°S	20°S
S (10^{-5} s^{-1} K)	1.112	1.091	1.090	1.046	0.941	0.781	0.619
R (10^{-5} s^{-1} K)	2.488 (same at all latitudes)						
S_G (W m^{-2})	232	245	216	159	155	199	179
ϵ_*	0.176	0.214	0.166	0.060	0.058	0.143	0.161

7.6. *Large-scale rain*

Supersaturation produced in the model is removed in precisely the same way as in Corby *et al.* (1972).

7.7. *Convection*

The scheme used during GATE is almost identical to that of Corby *et al.* (1972). The last term appearing in their equation (35) is omitted and because of the unequally spaced levels their equation (33) becomes

$$\Delta T_k = C_{k+\frac{1}{2}} \sigma_{k+\frac{1}{2}}^{\kappa} \left[\delta_\sigma (T/\sigma^\kappa) \right]_{k+\frac{1}{2}} \frac{\Delta\sigma_{k+\frac{1}{2}}}{\Delta\sigma_k} (2\Delta t)$$

$$\Delta T_{k+1} = - C_{k+\frac{1}{2}} \sigma_{k+\frac{1}{2}}^{\kappa} \left[\delta_\sigma (T/\sigma^\kappa) \right]_{k+\frac{1}{2}} \frac{\Delta\sigma_{k+\frac{1}{2}}}{\Delta\sigma_k} (2\Delta t)$$

and

$$C_{k+\frac{1}{2}} = C(\Delta\sigma_{k+\frac{1}{2}})^2 \left[\delta_\sigma (T/\sigma^\kappa) \right]_{k+\frac{1}{2}}$$

where $C = 4 \times 10^{-6}$ s^{-1} for dry convection; for moist convection, $C = 4 \times 10^{-6}$ s^{-1} until the run of 9 September and 4×10^{-7} s^{-1} thereafter. There is no minimum parcel size and evaporation of rainfall is allowed in the levels beneath if the relative humidity is less than 80 per cent. The maximum parcel size allowed is the smaller of the two layer depths involved. Although satisfactory in the tests prior to GATE this sometimes gave unrealistic responses to superadiabatic lapse rates encountered in GATE analyses until these were removed in the interpolation step in Phase III (section 5).

8. RESULTS OF THE FORECAST EXPERIMENT

by W. H. Lyne, Ph.D., P. R. Rowntree, Ph.D. and Julia M. Slingo, B.Sc.

8.1. *Forecasts of the circulation*

8.1.1 *Large-scale features of the GATE atmosphere.* Assessment of the model's behaviour has been concentrated on Phase III because 24-hour forecasts were made and because data, analysis and model were improved following the experience of the earlier phases. In this section the major features of the atmosphere in the forecast area are briefly considered so as to place in context the more detailed analyses of the simulations to be described later. Further details of some of these results are given by Lyne *et al.* (1975).

Figures 14 (a)–(c) show a selection of charts for 12 GMT on 13 September. The 1000 mb geopotential chart is, in most respects, typical of all Phase III. The north and south Atlantic tropical highs varied little, with maximum geopotentials in the analysis area mostly about 240 and 160 gpm respectively. Between them a trough with minimum geopotentials of order 110 gpm linked the continental lows over Africa and South America. The only major variation in this pattern was a simultaneous weakening of northern high and oceanic trough from 8 to 11 September with extremes of only 180–200 gpm and 130 gpm respectively. Krishnamurti *et al.* (1975) have discussed the variations in the strength of the Atlantic trades during GATE; the period 8–11 September was one of the two most marked minima, with mean wind speeds only about half the average. Analysis of the South American low was generally based on few data and was sometimes marred by spurious features caused either by erroneous data (for example near 9°S, 65°W in Figure 14(a)) or by incomplete correction of erroneous forecasts. Similar features were common in the poorly observed regions of central and eastern Africa.

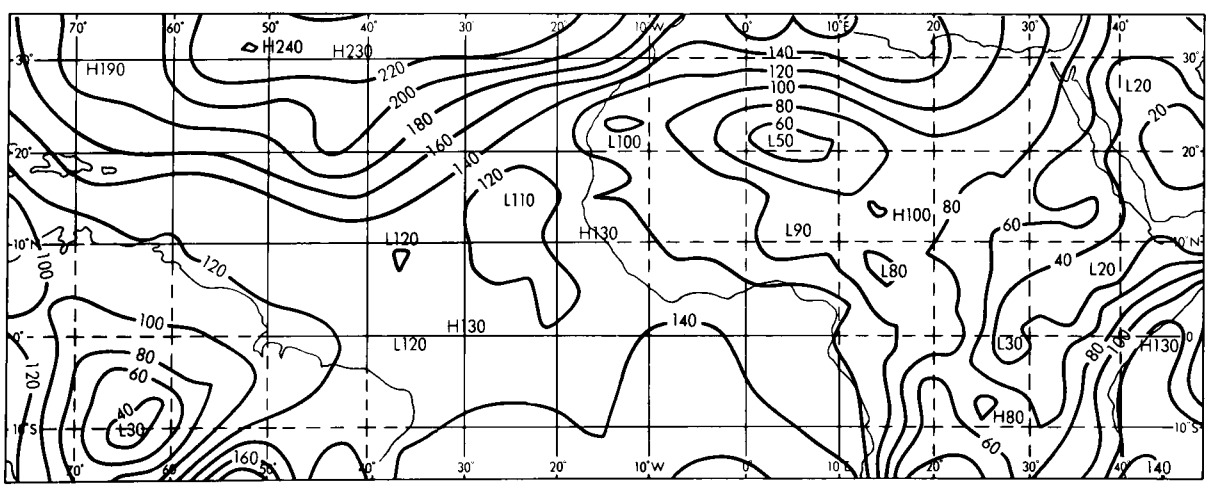

FIGURE 14(a). Initialized geopotential field at 1000 mb for 12 GMT on 13 September 1974

Units: gpm

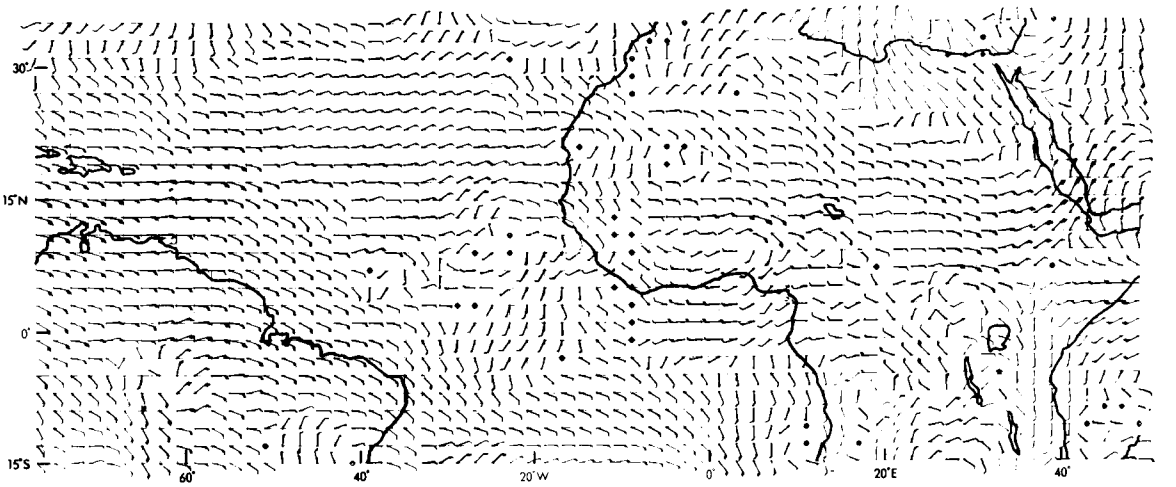

FIGURE 14(b). Initialized wind field at level 9 (σ = 0.844) for 12 GMT on 13 September 1974

Full feather = 5 m s^{-1}

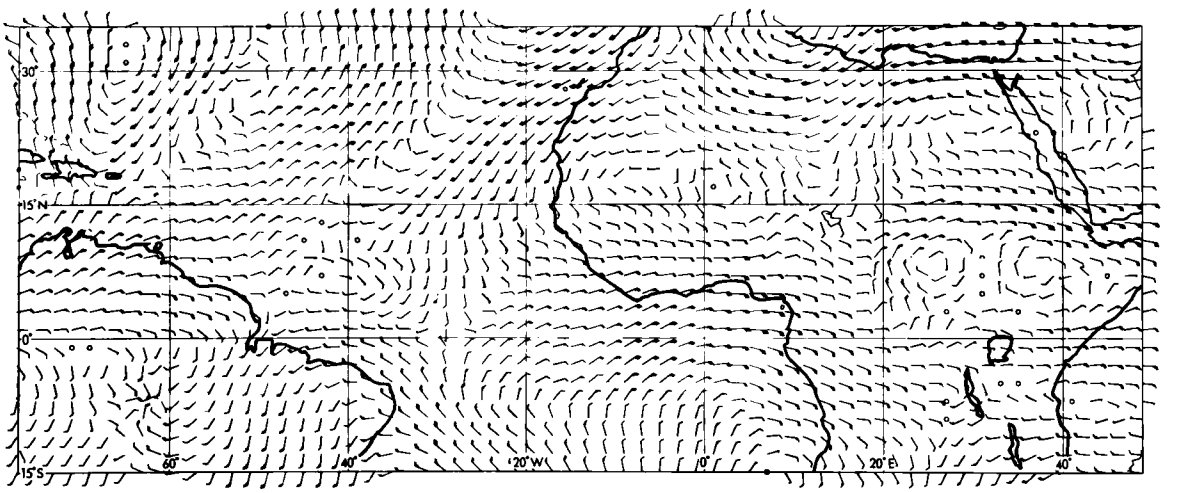

FIGURE 14(c). Winds at 250 mb for 12 GMT on 13 September 1974

Full feather = 5 m s^{-1}

Geopotential contours around the African low roughly followed the continental outline with variations over West Africa as disturbances moved west (for example near 25°W and 5°E in Figure 14(a)). Troughs from the Arabian low extended west into the Sahara and south-west into central and east Africa though 1000 mb geopotentials in the latter areas were mostly fictitious as they were below ground level.

The lower tropospheric flow may be illustrated by winds at σ = 0.844 (Figure 14(b)). Easterly flow predominated over the Atlantic, South America and Africa north of 10°N

with southerlies off east Africa. Over the Gulf of Guinea and nearby Africa westerly or south-westerly flow prevailed whilst over central Africa vortices such as that in Figure 14(b) were common. These vortices appear to be model-induced and are discussed further in section 8.1.3. As in the 1000 mb geopotential fields, the flow over West Africa and the northern tropical Atlantic was perturbed by African disturbances moving west. Troughs may be detected near 58°W, 23°W and 4°E in Figure 14(b). The history of such troughs at 13°N during Phase III is analysed in the next section, both for $\sigma = 0.844$ and for 500 mb.

The upper tropospheric flow may be represented by that at 250 mb where data were more adequate than at most levels because of the concentration of winds derived from satellite cloud pictures and aircraft reports. The inner tropics had generally easterly flow except where southern hemisphere troughs extended into low latitudes; this was particularly common near eastern South America as in Figure 14(c). In the northern tropics too, the flow over the Atlantic appeared more dominated by troughs extending from the subtropical westerlies such as that near 40°W in Figure 14(c) than by the waves in the easterlies. Therefore, in the analysis of wave movements in the next section, attention at 250 mb will be focused on these subtropical waves in the 20°–25°N region.

8.1.2. *Analysed and predicted wave movements.* Figures 15 and 16 show analysed and predicted trough movements at $\sigma = 0.844$ and 500 mb. Additionally, positions for 850 mb were subjectively estimated on the basis of observations at 00 GMT and occasionally 06 and 18 GMT as well as at 12 GMT. Continuity and satellite cloud data were also used where other data were inadequate. These subjective estimates thus serve as a check on the objective analyses which might be unduly influenced by erroneous forecasts. The analysed movements appear to be broadly in agreement though the objective analyses tend to place troughs too far east, as is to be expected from the forecast errors at this level summarized in Table IX for 20° longitude sectors, based on initial position. The analysed movement is similar for each region except 20°–40°E, where there are few observations and the waves are mainly spurious features created by the forecasts. The

TABLE IX. *Mean analysed and predicted 24-hour westward movements of troughs and prediction errors during Phase III*

	No. of cases	Movement analysed	(degrees of longitude) predicted	error
$\sigma = 0.844$				
60°–40°W	5	7.6	5.8	−1.8
40°–20°W	10	5.6	5.0	−0.6
20°–0°W	10	6.5	2.6	−3.9
0°–20°E	8	6.0	1.5	−4.5
20°–40°E	11	3.6	1.9	−1.7
500 mb				
60°–40°W	5	7.0	6.0	−1.0
40°–20°W	15	6.9	7.4	+0.5
20°–0°W	12	5.5	7.3	+1.8
0°–20°E	4	9.3	7.8	−1.5
20°–40°E	5	3.8	5.2	+1.4

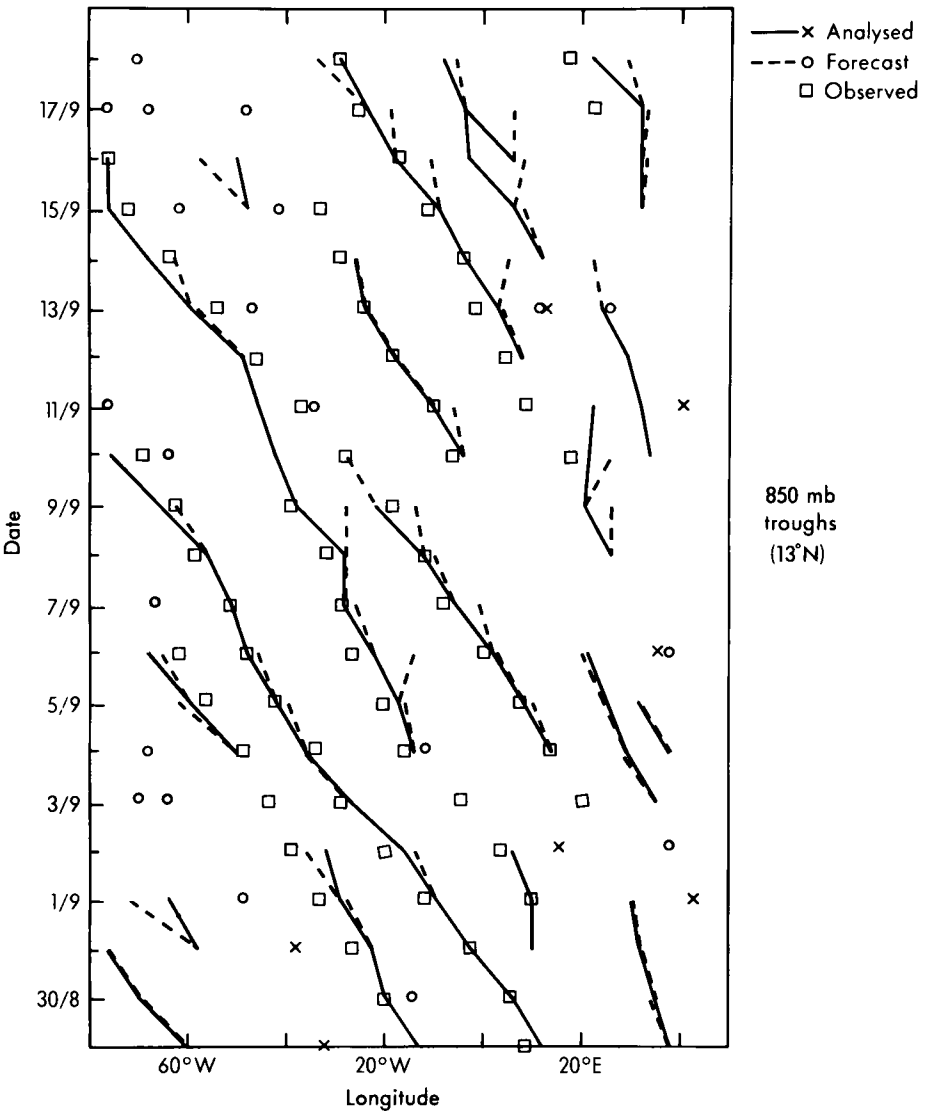

FIGURE 15. Analysed (solid lines, crosses) and predicted (dashed lines, circles) trough positions at $\sigma = 0.844$, 13°N during Phase III of GATE
Squares mark subjectively estimated 850 mb trough positions

errors are large for waves starting over land (20°W–40°E) with forecast movements only 10 to 50 per cent of the analysed. In some cases troughs appeared to stagnate when low-level convergence, ascent, upper outflow and rainfall became excessive. This is discussed further in section 8.1.3.

The forecast errors are much smaller at 500 mb and no longer depend on longitude, probably because of the relatively small effects of convergence and divergence at this level. Data were less plentiful at 500 mb but the similarity of the analysed speeds at

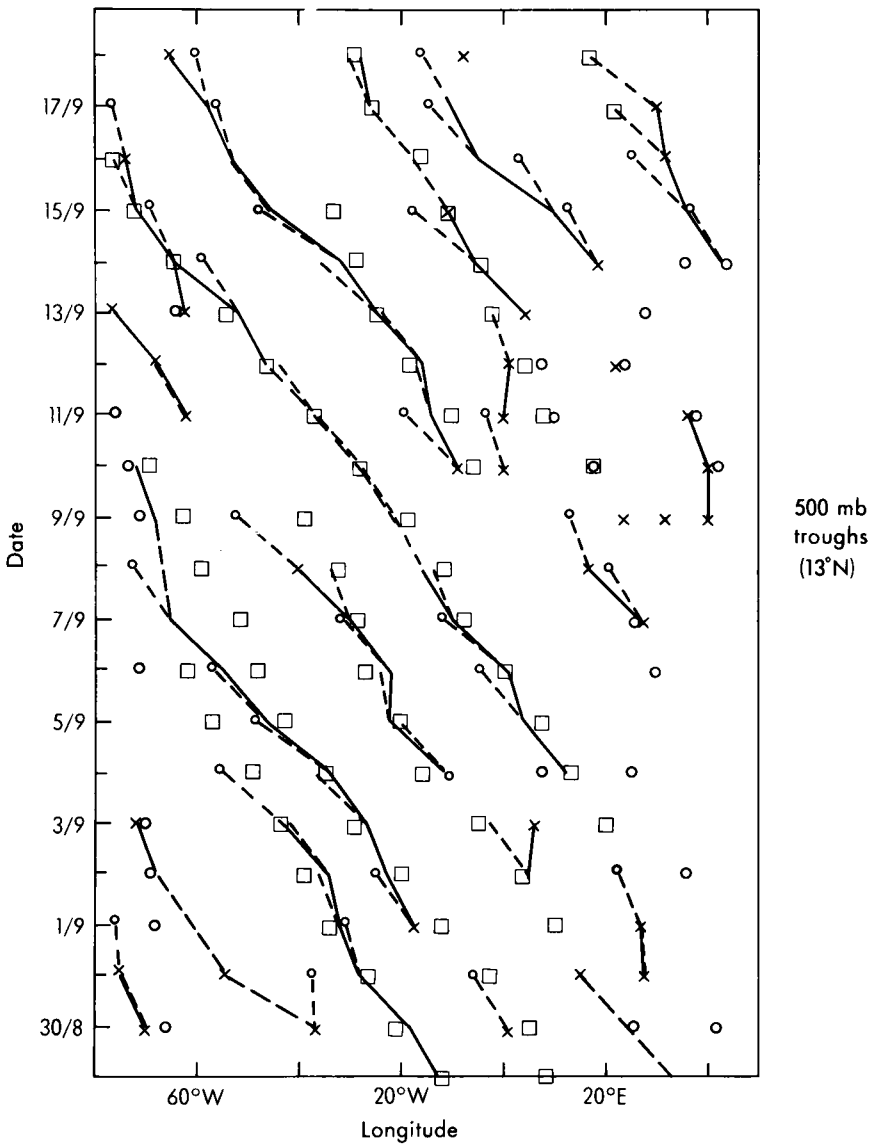

FIGURE 16. As Figure 15 but for 500 mb (except squares which are for 850 mb)

$\sigma = 0.844$ and 500 mb and the general agreement with subjectively estimated 850 mb trough positions (Figure 16) suggests that this has not significantly affected the comparison.

A notable feature of Phase III was the frequent development over the Atlantic of large-amplitude upper troughs in the northern tropics and subtropics such as that in Figure 14(c). A similar mean trough was found by Krishnamurti (1971) in his analysis of June to August 1967, and another such trough is well known over the Pacific (see for example Sadler 1975). The troughs sometimes become cut-off vortices. Their movement was generally westward over the Atlantic (Figure 17) with speeds similar to those of the

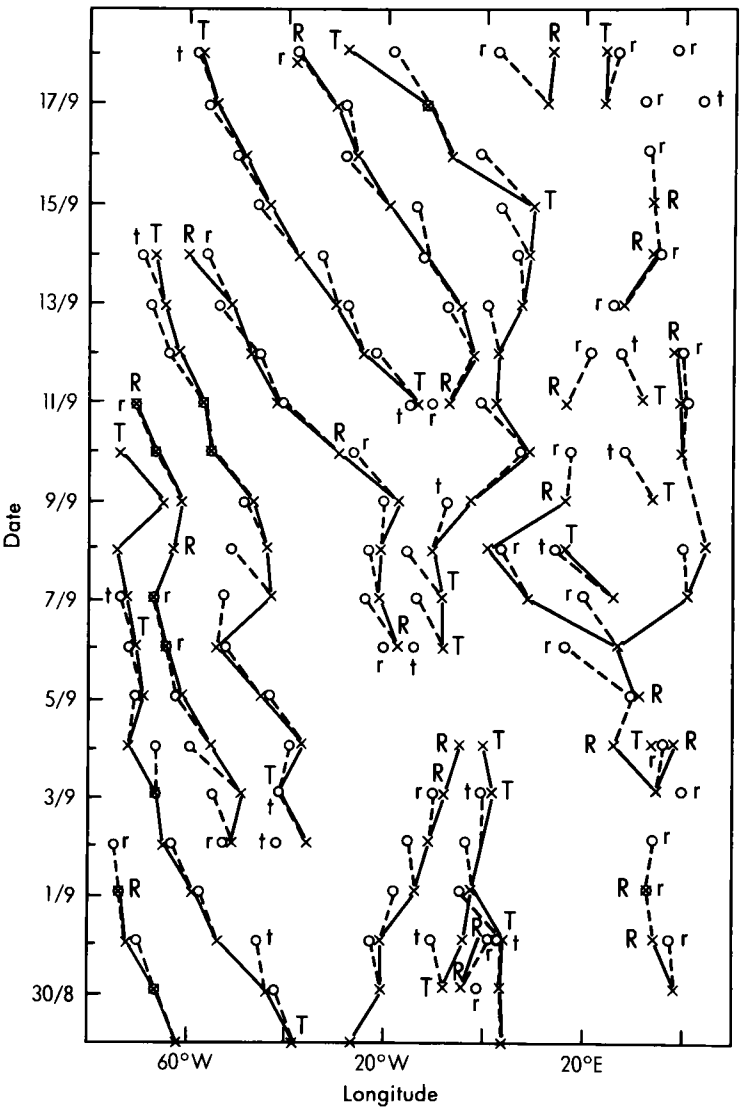

FIGURE 17. Analysed (solid lines, crosses) and predicted (dashed lines, circles) trough (T,t) and ridge (R,r) positions at 250 mb, 23°N during Phase III of GATE

tropical lower tropospheric troughs discussed above. The two wave systems are unlikely to be independent since they both affect the 500 mb level but the wavelengths of the upper tropospheric vortices are about twice as large so that parts of Figures 16 and 17 (for example 10–18 September at 0°–70°W) give the impression that tropical lower tropospheric troughs occur in phase sometimes with ridges and sometimes with troughs in the upper westerlies. A wave that developed into hurricane Fifi was in phase with a 23°N, 250 mb ridge from 20°W on the 9th to 60°W on the 14th while the preceding 250 mb ridge was close to the longitude of tropical storm Elaine as it moved from 50°W on the 4th into the subtropics near 70°W on the 8th (not shown beyond the 6th in Figures

15 and 16 because of its latitude). A warm upper ridge might be expected to favour development of warm-core disturbances such as tropical storms but a larger sample is obviously needed to confirm this relation.

8.1.3. *The mid-tropospheric temperature field and spurious rainfall maxima.* Figures 18(a) and (b) show initial 850–500 mb thickness and 24-hour rainfall for the forecast from 12 GMT on 13 September. The thickness or mean temperature distribution was

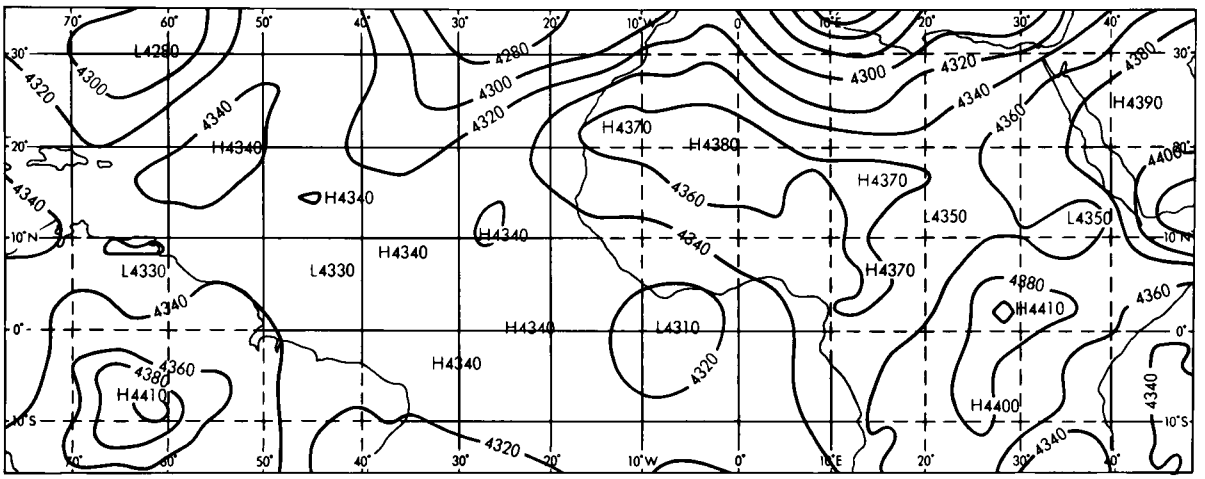

FIGURE 18(a). Initialized field of 850–500 mb thickness for 12 GMT on 13 September 1974

Units: gpm

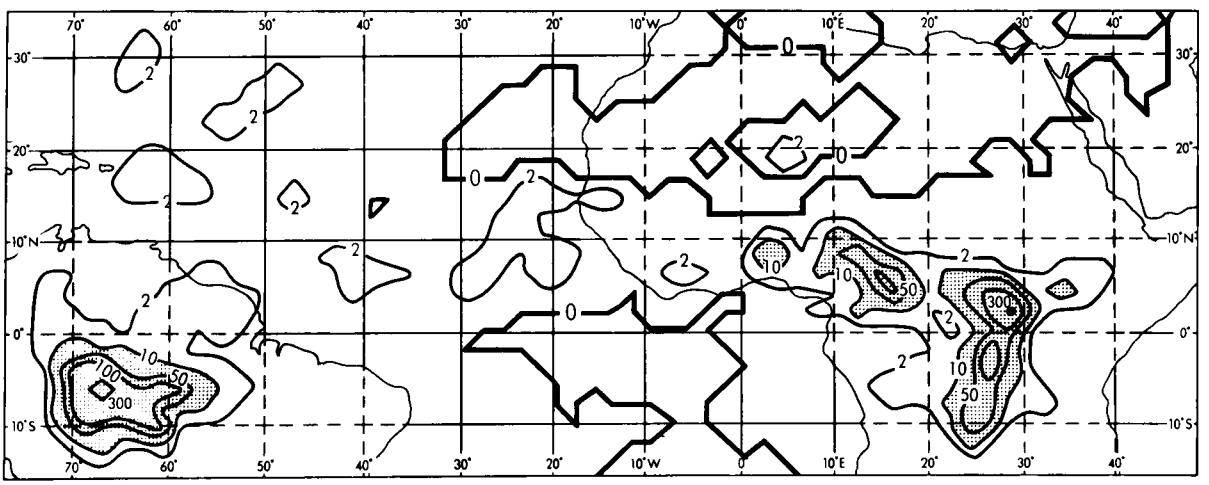

FIGURE 18(b). Total rainfall forecast for 24-hour period ending 12 GMT on 14 September 1974 from fields initialized at 12 GMT on 13 September 1974

Units: mm

typical of Phase III except for the warm region over South America, analysed thicknesses of 4370 gpm upwards usually being confined to Africa. The very small regional temperature variations over the tropical Atlantic and the moister parts of west Africa were normal. The higher thicknesses over the drier Sahara were a persistent large-scale feature, which is well known from climatology and may be attributed to high near-surface temperatures over arid ground with a steady return with height to values typical of surrounding moister areas. The temperature distribution over central and eastern Africa was more irregular and, with the sparse data cover, unconvincing.

The rainfall in Figure 18(b) was also typical of Phase III except, again, that intense peaks over South America occurred only occasionally. The rainfall forecasts are discussed in section 8.2 but it is appropriate to discuss these intense rainfall maxima here. Such rainfall data as were available clearly showed them to be spurious. Note that the African and South American rainfall maxima in Figure 18(b) were both located near maxima of 850–500 mb thickness. That this relation held rather generally was established for the African region by comparing the locations of thickness maxima to the locations of intense rainfall peaks over Africa for forecasts starting on 4 to 13 September (Lyne *et al.* 1975). Nine of the ten forecasts studied had a thickness maximum exceeding 4380 gpm over Africa south of 10°N and each of these was associated with a 100 mm rainfall peak within about 500 km. The thickness maxima tended to occur in gaps between radiosonde stations which provided good 12 GMT data, the warm areas having been retained from the previous forecast. It is evident that in this version of the model warm regions tended to generate intense vortical rain-producing disturbances rather like hurricanes. Improvements in experiments since GATE in the flow and rainfall forecasts over Africa and south America are discussed in section 10.

8.2. *West African forecasts for 4–14 September*

8.2.1. *Introduction.* In this section the observed and forecast rainfall distributions over west Africa and the B-scale area are considered and their relationship to synoptic features is discussed. The 10-day period 4–14 September is considered, though attention is mainly focused on the five-day period from the 9th to the 14th. As noted in section 7.7 the convection parameter, C, was changed between 9 and 10 September with the aim of reducing the intensity of rainfall maxima, especially over central Africa. It was obvious that this had a large effect on the rainfall predicted over west Africa.

If meaningful rainfall statistics are to be compiled, the observing network must be quite dense. All the rainfall reports available during GATE were used but unfortunately there were periods when data in certain areas (principally the region around Liberia and Sierra Leone) were sparse. The area from 5°N to 20°N and from 10°E to 20°W was divided into 5° squares and the 24-hour totals observed at 06 GMT were meaned for each square. These data were used in constructing Figures 19 and 20. Table X gives the total number of rainfall observations at 06 GMT for each 5° square over the 10-day period.

Figure 19 shows the isopleths of mean 24-hour rain totals for the period 4–14 September. The 06 GMT observations were used to calculate the observed distribution, and totals for the 24 hours to 12 GMT were used to calculate the forecast distribution. In plotting the forecast distribution in both Figures 19 and 20, the forecast region was divided into the same 5° squares as for the observations and the means for each square

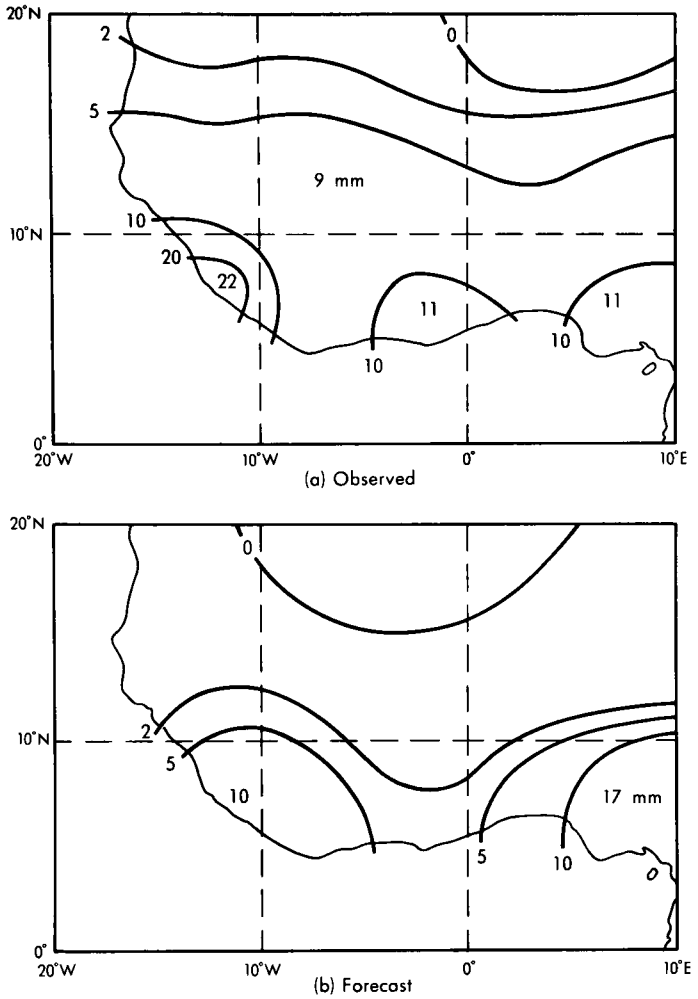

FIGURE 19. Mean 24-hour rainfall totals for the 10-day period 4–14 September 1974, as (a) observed and (b) forecast
Units: mm

TABLE X. *Total number of rainfall observations at 06 GMT for each 5° square over the 10-day period 4–14 September*

	20°W	15°W	10°W	5°W	0°	5°E	10°E
20°N	35	55	24	25	0	9	
15°N	43	40	40	59	67	67	
10°N		17	52	40	84	34	
5°N							

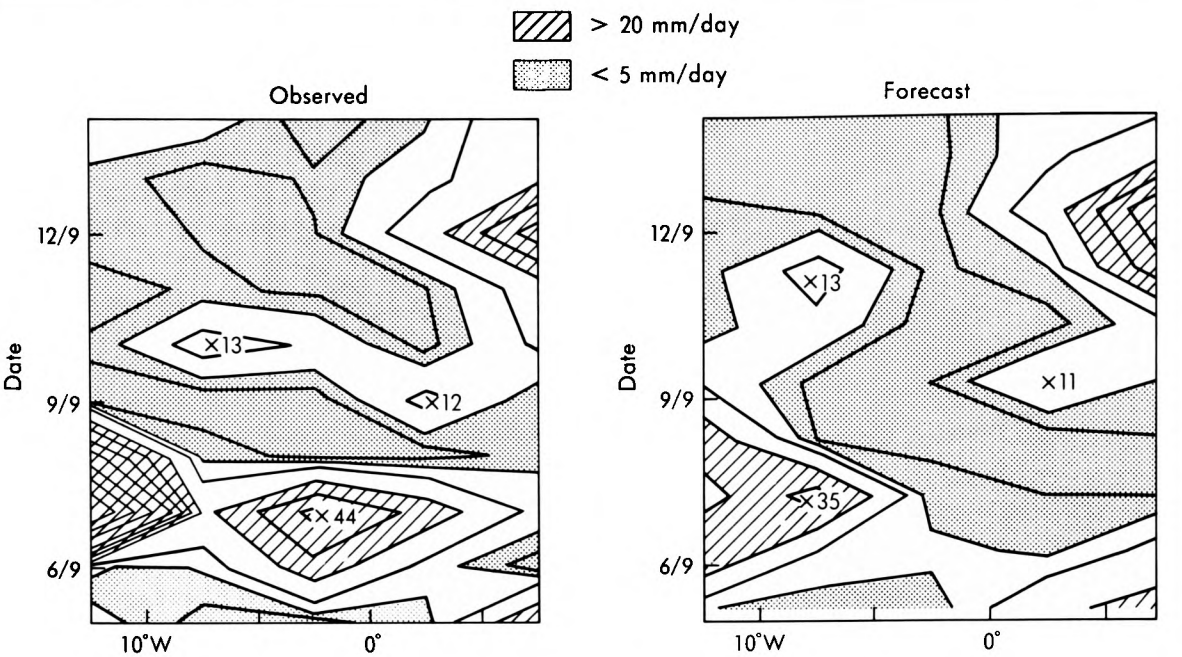

FIGURE 20. Mean totals of observed and forecast rainfall for the previous 24 hours
Units: mm

found. It can be seen that the model was generally too dry especially north of 10°N, but that it did get the distribution approximately correct. An interesting feature in the observations was the weak maximum at about 2°W near the coast, whereas the model had a minimum in that region. However, climatology also shows this to be a region of minimum rainfall at this time of year as well and this 10-day period is, in this respect, anomalous.

8.2.2. *Rainfall in the strip 5°–10°N.* Most of the observed and forecast rainfall occurred between 5° and 10°N, and its history is shown in Figure 20. Each of the two diagrams has longitude as the abscissa and time as the ordinate, so it should be possible to track areas of rainfall as they crossed the region from east to west. Note that the isopleths for the forecast rainfall begin six hours later than the observed because of the difference in data times mentioned in section 8.2.1.

The rainfall between 5° and 10°N over west Africa largely occurs ahead of and within the troughs of westward-moving African waves or vortices (Burpee 1974, Reed *et al.* 1977). The figure shows that the model produced the observed alternation of wet and dry periods, associated with the waves, together with approximately the right longitudes for the maxima of rainfall. Thus the wet period of the 5th to the 8th, associated with the wave which crossed west Africa at this time (Figure 15), was forecast though the maximum in the west was wrongly placed at 7.5°W and rainfall was too light in the 0°–5°W region.

The following dry spell was forecast correctly though the subsequent maximum of rainfall at 06 GMT on the 10th at 7.5°W was forecast a day late. This rainfall was associated with the next wave and the maximum of rainfall that it produced at 06 GMT on the 9th at 2.5°E was forecast correctly, as was the dry region between the two maxima. This demonstrates a major failing of the model in moving these features too slowly, as discussed in section 8.1.2.

The next dry period was forecast as was the maximum of rainfall at 06 GMT on the 12th at 7.5°E. This was associated with the third wave of the period which gave a maximum of 8 mm at 06 GMT on the 14th at 12.5°W. The model again forecast this a day late (not shown), but it gave the dry region between correctly.

It is interesting to note that the forecast totals of rainfall in this strip were quite close to the actual totals, as were the locations of their maxima and minima. Therefore the model, although too dry further north, appeared to give a good forecast for the rainfall in terms of quantity and location when averaged over 5° squares, but because it moved the disturbances too slowly the timing was generally late.

8.2.3. *Lower tropospheric wind analyses and forecasts.* Figure 21 shows the analysed and 24-hour forecast flow patterns at level 9 (near 850 mb) for the period 9–14 September. The forecast fields shown on the right were used as background for the analysis so the two are not independent, and good agreement may only mean that there were few observations with which to correct the background field.

Three major 850 mb troughs moved westward in the region under consideration during this period; in Figure 15 these are shown crossing 10°W on about the 8th, 11th and 15th. The first, which was associated with the heavy rain over Africa on the 5th–8th (Figure 20), can be seen in the analysis for the 9th off the west African coast. On the 10th both forecast and analysis place it north of the B-scale ship array whereafter it moved across the Atlantic and later developed into hurricane Fifi which devastated Honduras on the 19th.

The second trough had become a well-developed vortex by the 10th and moved steadily westward near 7°N until the 12th and then crossed the B-scale array ($8\frac{1}{2}$°N, $23\frac{1}{2}$°W) on the 13th. The forecasts for the 10th and 11th when it was over land move it too little westward but thereafter its position is quite well forecast as also is the well-marked ridge which is analysed behind it on the 14th.

The third trough was not clearly analysed until the 12th. It moved west near 9°W and was poorly forecast, as the second wave was while over land. As shown by Figure 20 the model forecast persistent heavy rain over Nigeria at this time and this was again associated with the slow forecast movement which was typical of the model used during GATE (see section 8.1.3).

8.3. *A comparison of the observed and predicted structure of the tropical atmosphere*

8.3.1. *Introduction.* The temperature, humidity and zonal wind structure of the model have been studied using vertical cross-sections along certain latitudes and longitudes. Particular attention has been paid to the change in the fields during a 24-hour forecast. The period studied covered 9–15 September. Time-mean fields were constructed by taking a mean of the initial conditions for 9–14 September and a mean of the 24-hour forecast fields for 10–15 September (all fields were valid for 12 GMT). Cross-sections

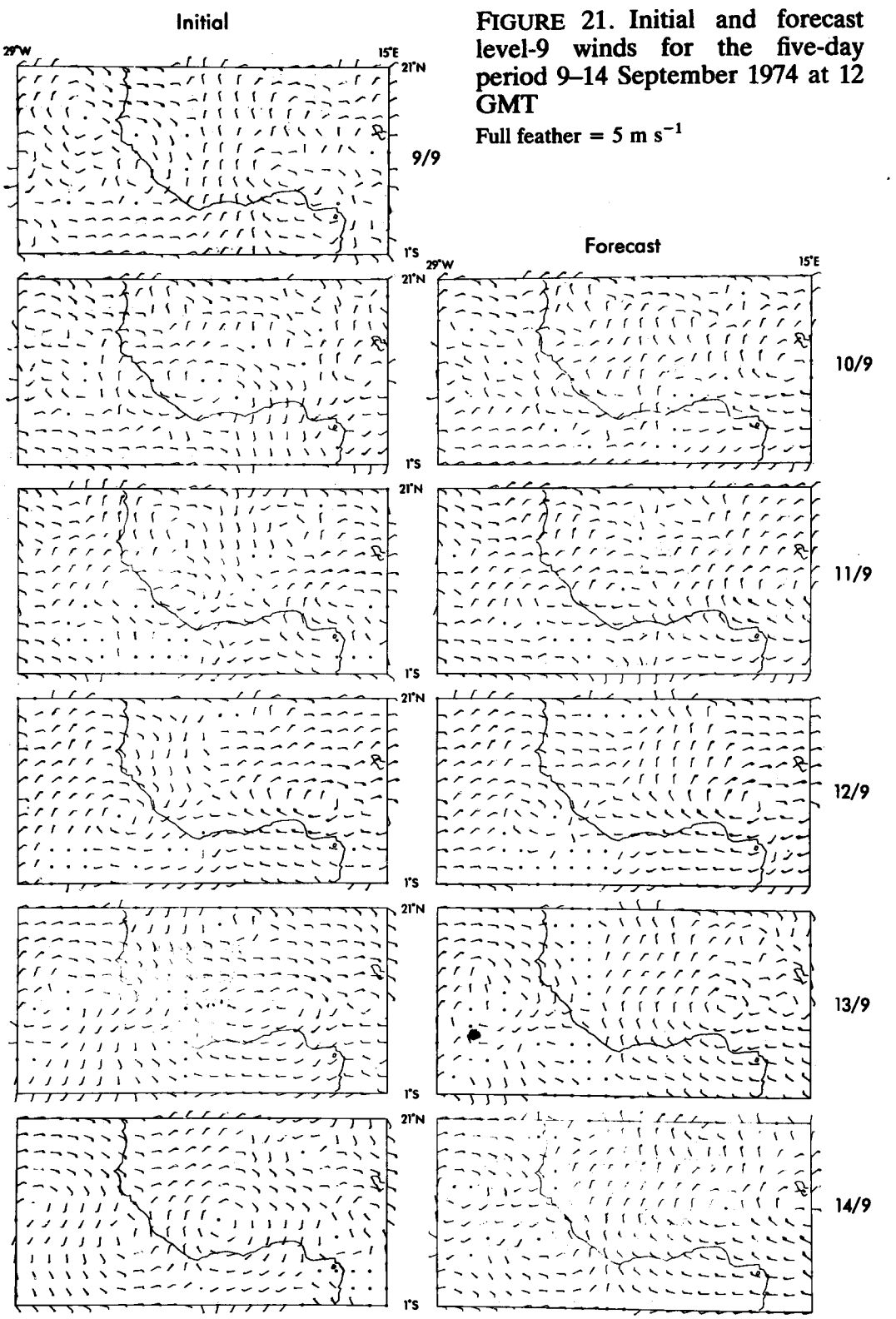

FIGURE 21. Initial and forecast level-9 winds for the five-day period 9–14 September 1974 at 12 GMT

Full feather = 5 m s^{-1}

from these two mean fields were then compared and the trend during the forecast assessed. However, it should be noted here that some of the changes shown in the mean fields were associated with features that moved through the cross-sections during the period and show up owing to the difference in the period of meaning between initial and forecast fields, whilst others are residuals of large day-to-day forecast errors of opposite sign.

The three cross-sections chosen for studying temperatures and relative humidities are shown in Figure 22 together with adjacent stations normally available. Zonal winds were studied for the first two sections. The first cross-section runs north–south through the centre of the B-scale area where there was good coverage from ships. The second extends north from the Bight of Benin into the Sahara Desert and the third lies along 15°N at which latitude two of the A-scale ships and several other stations were situated; only a few results are shown for the 15°N section.

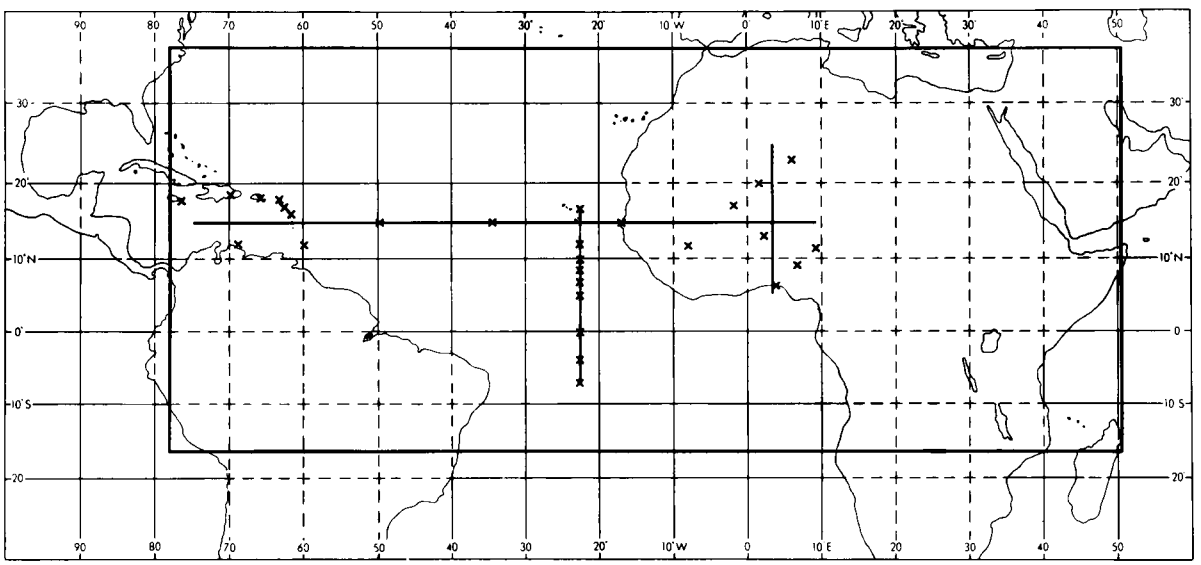

FIGURE 22. Map of the GATE model area showing the positions of the three cross-sections and adjacent upper-air observing stations

To enable the structure of the temperature fields to be seen, the differences from a model mean atmosphere at 7°N were used. The temperatures of this mean atmosphere at each σ-level are given in Table XI.

8.3.2. *Temperatures.* Figure 23 shows the vertical temperature cross-sections along 23°W. The most noticeable feature is the intensification near to and south of the equator of a stable layer near the top of the model's boundary layer at $\sigma = 0.79$ during the forecast. This is not an unrealistic structure and is often observed over tropical oceans in areas where there are few disturbances. A vertical cross-section of the time-meaned observed, subjectively analysed temperatures has also been constructed (Figure 23(d))

TABLE XI. *Model mean temperature at 7°N*

Level σ	Temperature K
0.022	216.16
0.089	201.10
0.157	206.71
0.230	223.84
0.317	241.47
0.436	258.08
0.578	271.22
0.718	281.29
0.844	288.73
0.937	293.18
0.987	295.05
Surface	297.64

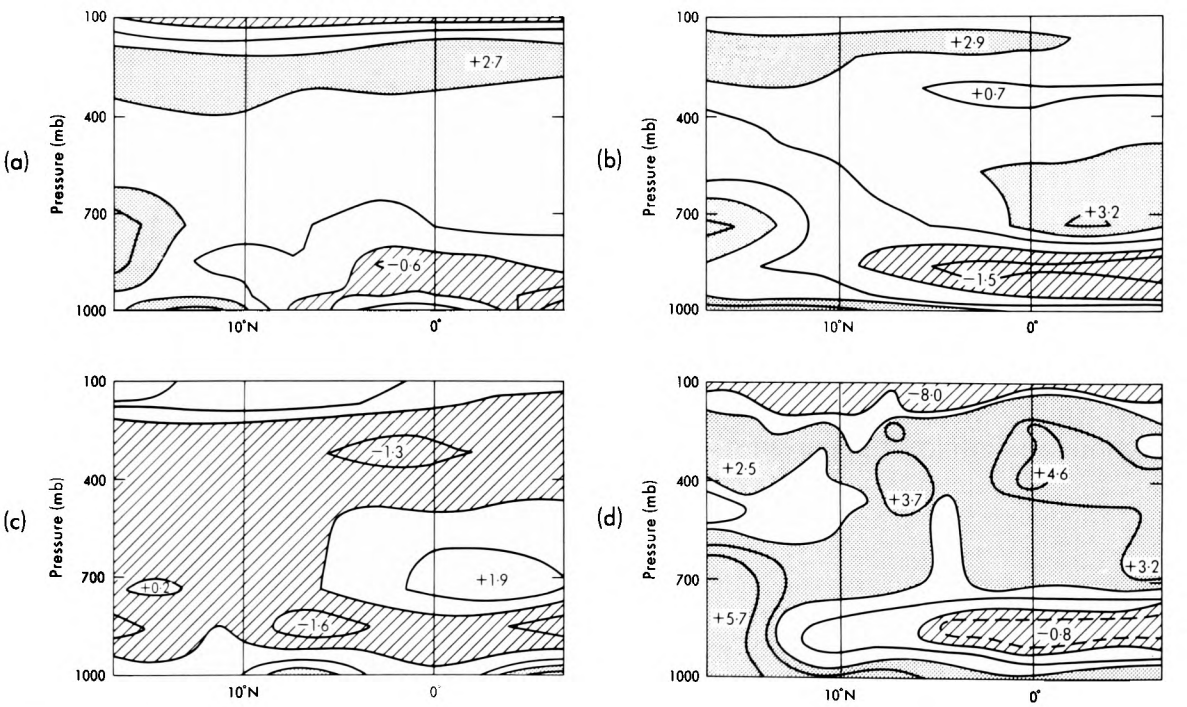

FIGURE 23. Vertical cross-sections of temperature (K) along 23°N. Time averages for 9–14 September 1974 at 12 GMT expressed as departures from the model's 7°N mean

Isopleths generally at 1 K intervals. Areas >2 K stippled, <0 K hatched.

(a) Initialized 9th–14th; (b) Forecast 10th–15th; (c) Forecast minus Initialized; (d) Observed 9th–14th

and this clearly shows an inversion between 850 and 700 mb. It seems that this feature is smoothed out in the interpolation to σ-levels and is then re-created by the model. The large negative departures of the observed temperatures near 100 mb from the model's 7°N average are at the tropopause, which cannot be represented in this detail by the model's layered structure. A general cooling of about 1 K in the middle troposphere of the initialized field relative to the observed can largely be explained by a correction for estimated ship sonde error of about −0.5 K and by the cooling evident north of 6°N in the 24-hour forecasts which were used as background for the analysis. This forecast cooling appears to be due to insufficient compensation of radiative cooling by convective heating. Experiments with a single-column model show that this convection scheme tends to produce too cool a troposphere.

The near-surface temperatures in the initialized cross-section show cool spots near 7°S and 7°N. The former is due to a single erroneous observation and that at 7°N is due to a persistently erroneous ship sounding which gave heights some 20 to 30 gpm too low. This had more effect at 950 mb than at 1000 and 850 mb, apparently because it affected 950 mb both through the background field for that level, which took account of changes from background field to analysis at 1000 and 850 mb (section 4.2.2), and directly as an observation. Thus the near-surface layer was spuriously cold. In later versions of the analysis scheme the separate analysis of heights for secondary levels which is responsible for this error has been omitted because the structure functions derived from the GATE experiments do not justify its retention.

The 3°E cross-section (Figure 24) shows a warming south of 13°N over the Sahel and Sahara Desert. The near-surface temperatures increase by nearly 5 K during the forecast. This appears to be due to underestimation of the near-surface temperature maximum by either the analysis or interpolation. The highest 3°E forecast temperatures at 100 m ($\sigma = 0.987$) are about 310 K at 21°N which is about 3 K below the mean daily maximum screen temperature in 17°–27°N in September and so not unrealistically high. In the middle troposphere at these latitudes the forecast changes are small but further south over the moist land a cooling is evident similar to that noted for 23°W.

8.3.3. *Relative humidity.* Figure 25 shows the relative humidity cross-sections for 23°W. A feature which appears in most of the daily difference profiles is the drying south of the equator above the inversion. This is mainly attributable to descent which is forecast to be nearly $1\mu b\ s^{-1}$ at 24 hours. This is not necessarily unrealistic and the discrepancy from observations could be partly due to the model's neglect of vertical mixing in the absence of convection outside the boundary layer whose top is at $\sigma = 0.79$. The moistening near 15°N also occurs in most of the forecasts. Figure 26 shows that this occurs near 15°N over the central and east Atlantic near each observation, suggesting that the model's equilibrium state is moister than observed. The reason for this is not obvious.

The cross-section at 3°E (Figure 27) shows that the model maintains the dry initial state in the lower troposphere over the Sahara. Though relative humidity increases with height the model's absolute humidity varies little through a deep well-mixed layer. The moistening of the model's middle and upper troposphere in the rainy belt near 9°N occurs on most days in this period with development of saturated or near-saturated air

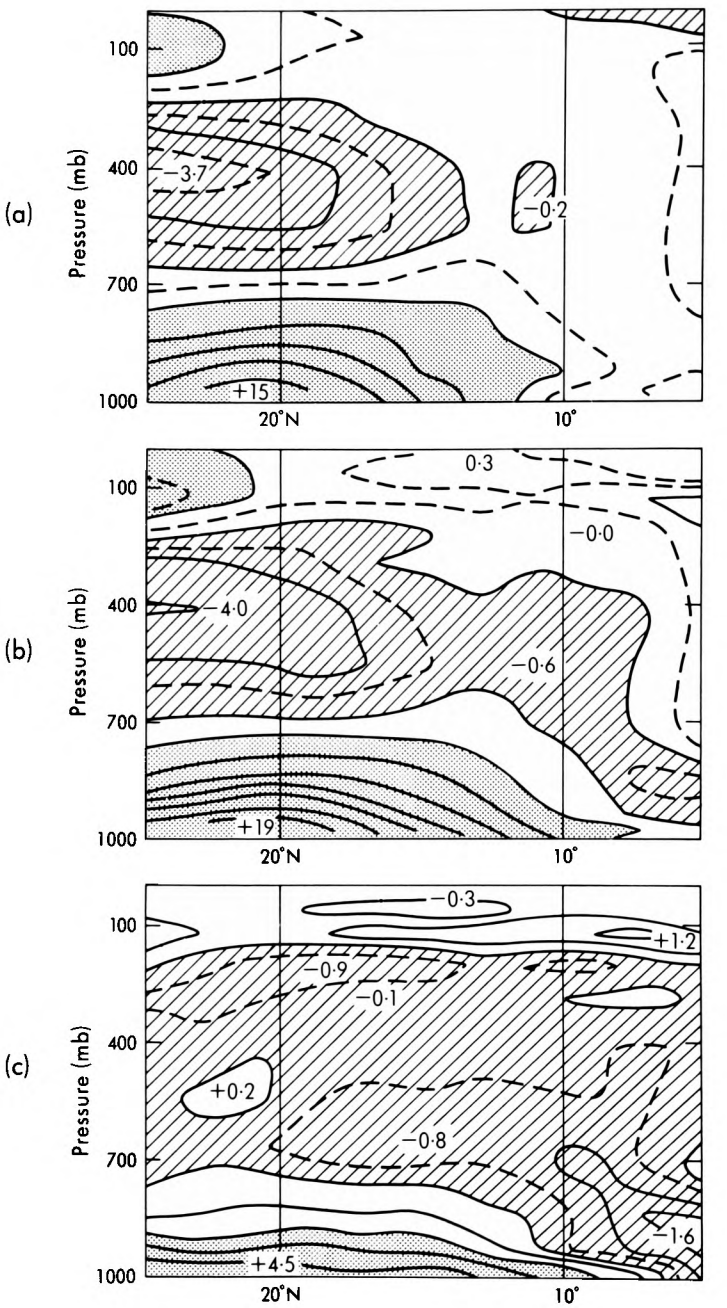

FIGURE 24. Vertical cross-sections of temperature (K) along 3°E. Time averages for 9–14 September 1974 at 12 GMT expressed as departures from the model's 7°N mean

Isopleths generally at 2 K intervals for (a) and (b), 1 K for (c). Shading as in Figure 23.

(a) Initialized 9th–14th; (b) Forecast 10th–15th; (c) Forecast minus Initialized

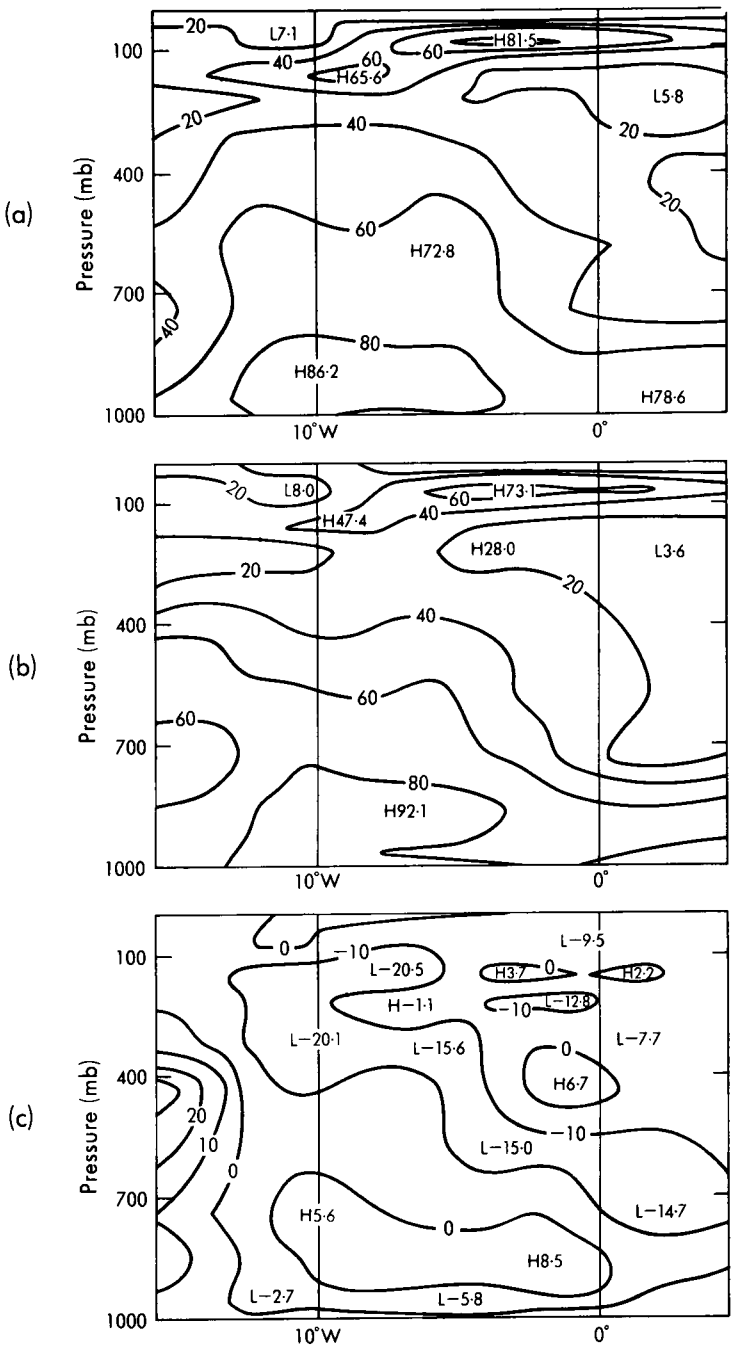

FIGURE 25. As Figure 24 except for relative humidities (per cent) along 23°W.

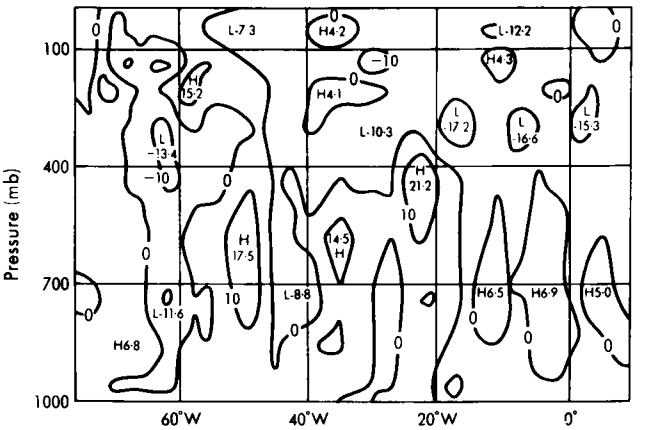

FIGURE 26. Vertical cross-section of time-averaged forecast minus initialized relative humidities along 15°N.

Initial fields for 12 GMT 9–14 September 1974; 24-hour forecasts verify at 12 GMT 10–15 September 1974

on the western edge of the persistent rainy area shown in Figure 19(b). This moistening was a feature of the intense rainfall areas discussed in section 8.1.3.

8.3.4. *Winds.* The zonal wind structure suffered less from recurrent errors than either the temperature or humidity structure. Cross-sections were constructed for 23°W and 3°E. The average changes at 23°W (Figure 28) were at most about 3 m s^{-1}, at least in the troposphere; these are much less than many of the day-to-day changes, so that a longer period would be necessary to establish their significance. There are significant changes in the boundary-layer winds near to and south of the equator with a regular weakening of the near-surface easterlies and a strengthening at 800–900 mb. Further evidence of this is shown in Table XII which compares the boundary-layer winds at the grid points on 23°W nearest to the equator and the winds observed at the ship at 0°N, 23½°W. All the observed data, and to a less extent, the model's initialized data, show a decrease in wind upwards from a maximum near the surface. The model fails to maintain this decrease, predicting a maximum near 950 mb ($\sigma = 0.937$) with a substantial decrease at 1000 mb and an increase at 850 mb. There is a marked decrease in the southerly component at 950 mb. The pressure gradient in this region is from high pressure south of the equator to low pressure in the intertropical convergence zone region at 5°–10°N. The model's frictional stress is tending to decelerate the near-surface flow both by surface friction and by downward transfer of more westerly momentum from above. The fact that the real atmosphere maintains the near-surface maximum suggests that the model overestimates these frictional stresses.

In the 3°E cross-section (Figure 29), the fields are dominated by the mid-tropospheric easterly associated with the strong meridional temperature gradient between the hot desert and the cooler savannah and tropical forest regions further south. As is shown in Figure 24, this observed north-south temperature gradient reverses above 600 mb. On the basis of thermal wind arguments the easterlies should show a maximum at the level of reversal, as observed. During the forecast the mid-tropospheric easterly becomes

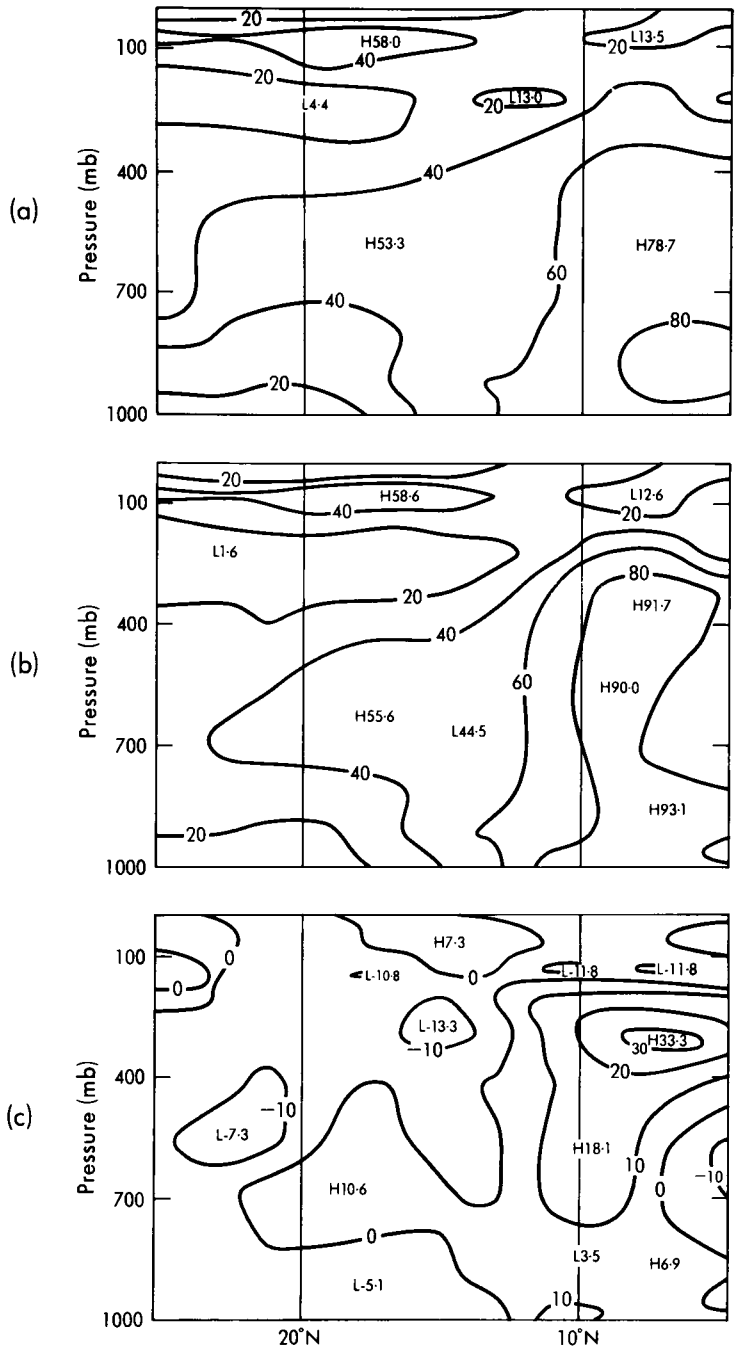

FIGURE 27. As Figure 24 except for relative humidities (per cent) along 3°E

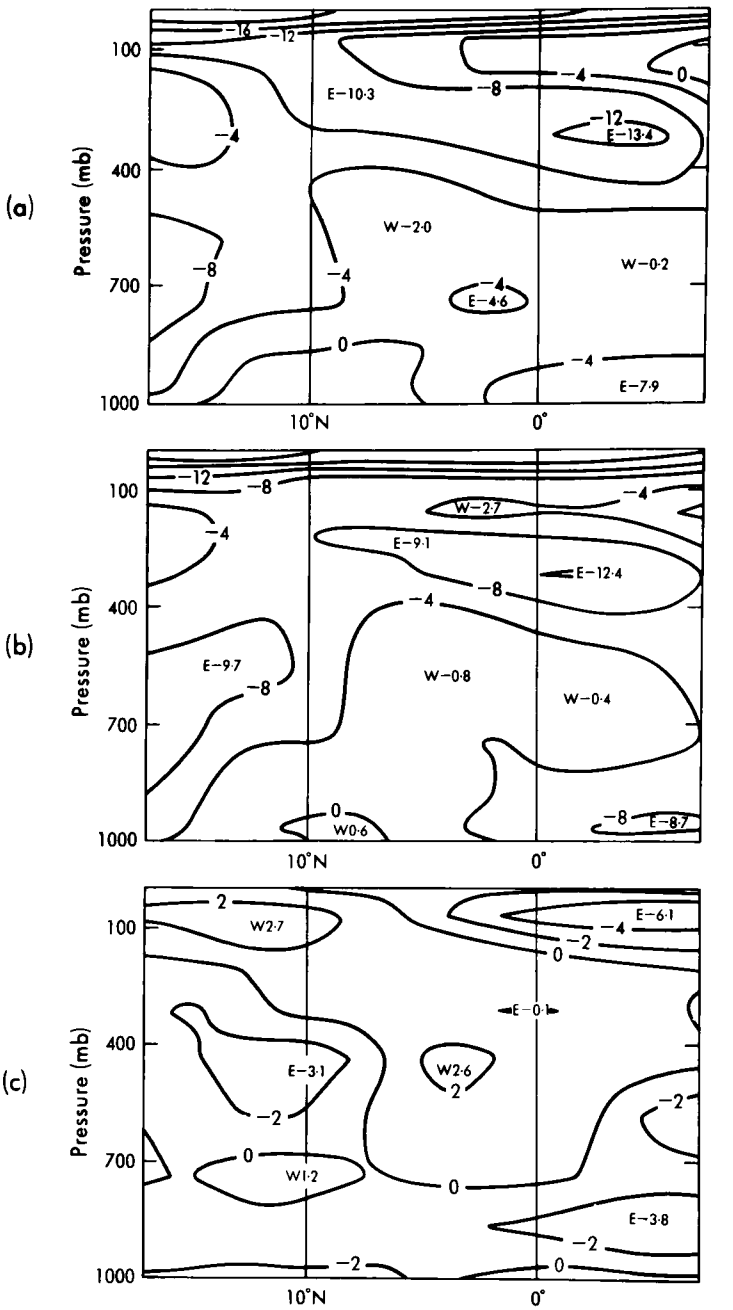

FIGURE 28. As Figure 24 except for zonal winds (m s^{-1}) along 23°W

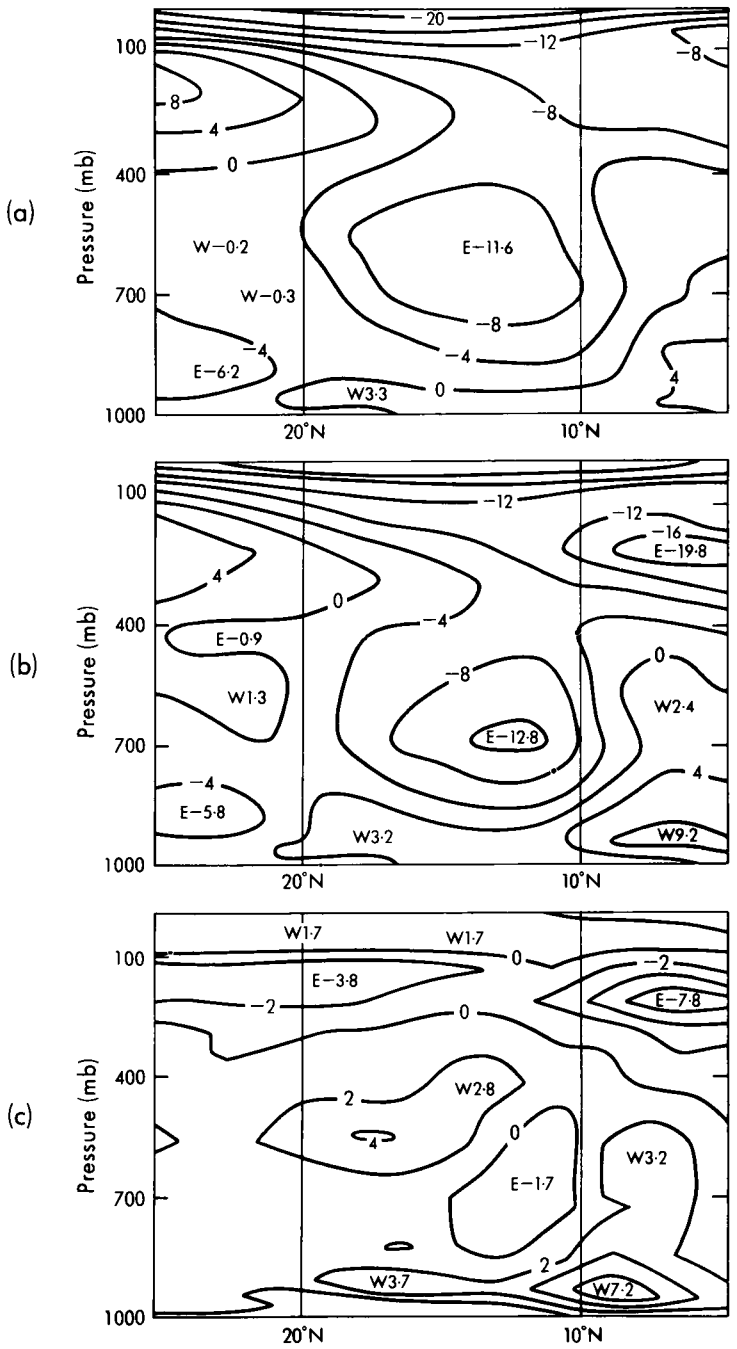

FIGURE 29. As Figure 24 except for zonal winds (m s^{-1}) along 3°E

TABLE XII. *Observed, initialized, and forecast boundary-layer winds*

	1°N, 23°W		Ship UBLF 0°N, 23.4°W	1°S, 23°W		Level
	Forecast	Initialized	Observed	Initialized	Forecast	
	deg m s^{-1}	deg m s^{-1}	deg m s^{-1}	deg m s^{-1}	deg m s^{-1}	mb
Date September						
	080 06	110 06	—	105 07	075 07	850
10	100 05	115 09	—	120 10	095 06	950
	110 04	130 10	—	125 12	100 04	1000
	100 07	110 03	150 05	120 04	105 08	850
11	120 10	130 09	130 09	125 11	120 11	950
	120 07	140 08	110 12	130 08	125 07	1000
	090 05	125 01	170 02	190 02	115 05	850
12	115 06	160 05	150 08	155 08	115 08	950
	125 05	165 10	160 13	160 10	115 05	1000
	160 04	200 04	185 04	215 06	170 05	850
13	145 05	165 12	—	160 14	135 07	950
	150 03	155 14	150 16	145 15	135 05	1000
	125 04	145 03	130 06	130 04	105 04	850
14	115 06	130 08	130 06	120 09	105 07	950
	110 04	085 07	125 14	065 09	105 05	1000
Mean components m s^{-1}						
u	−4.5	−1.9	−1.8	−1.9	−4.9	850
v	1.3	2.0	3.5	2.7	1.7	850
u	−5.5	−5.2	−5.2	−6.7	−6.9	950
v	3.0	6.2	5.5	7.3	3.2	950
u	−3.9	−5.7	−8.3	−7.2	−4.5	1000
v	2.4	6.9	9.6	6.0	2.3	1000

more concentrated about the 700 mb level. The increasing vertical shear of the zonal wind below 700 mb during the forecast can be related to the warming of the lowest layers over the desert by sensible heat flux from the surface and thus to an intensification of the meridional temperature gradient. Further south at 7°N the model develops a stronger upper tropospheric easterly. This is due to outflow on some days from the intense rainfall areas to the east discussed in section 8.1.3. The increase in the westerlies between 5° and 11°N in the lowest three layers can also be related to convergence into these rainfall areas.

Figure 30 shows the rms (root-mean-square) vector differences of the initial 850 mb winds from the analysed fields 24 hours later for Phase III. This is usually called the error of a persistence forecast, but that title is only appropriate where the analysis is reliable. Reference to Figure 1(b) shows that this is most likely to be the case in the areas of relatively good data such as 5°–12°N, 15°–28°W and 5°–15°N, 5°E–10°W, where the

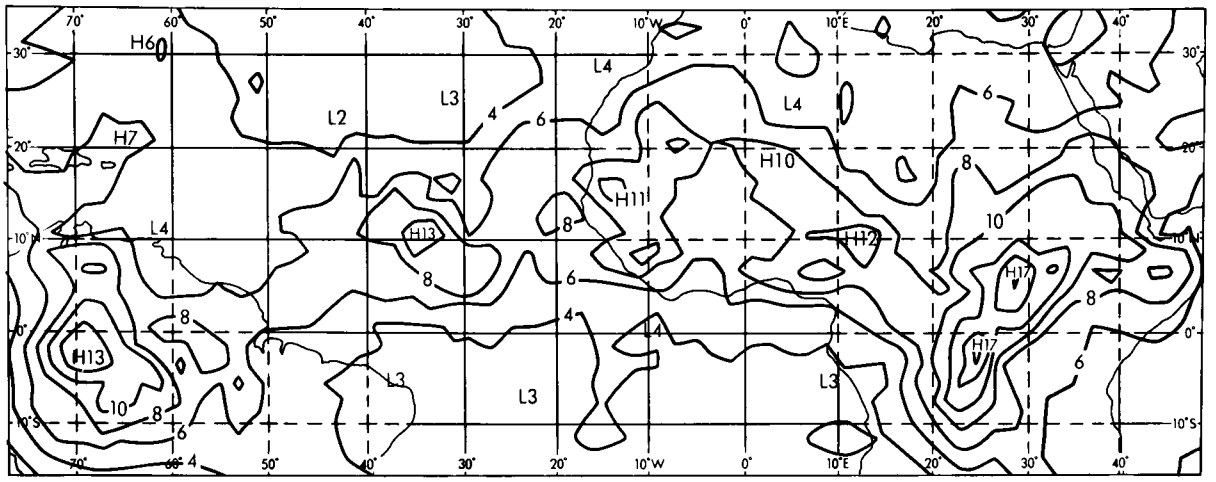

FIGURE 30. Magnitude of the root-mean-square vector differences between the initial 850 mb winds and the analysed wind fields 24 hours later, for Phase III
Units: m s^{-1}

typical rms difference is 6–7 m s^{-1}. In these regions we may also expect the rms vector differences of the 24-hour forecast winds from the analyses (not shown) to be a fair representation of the forecast error. Typical values in these areas were 3–5 m s^{-1}, suggesting that the model is showing some skill in predicting 24-hour changes in these regions.

Figure 30 shows areas of much smaller differences, locally as low as 2 m s^{-1}. These are in regions of steady trade winds over the Atlantic south of the equator and north of 20°N where forecast changes are small and data are few. Over central Africa and South America there are large changes between analyses, associated with the development of vortices and intense rainfall peaks in regions of sparse data as discussed in section 8.1.3.

9. REVISED ESTIMATES OF THE BACKGROUND FIELD ERROR STATISTICS

by D. B. Shaw, B.Sc.

As discussed in section 4.2.3 the specification of the error variance of the background field was originally made using skill estimates combined with climatological variability estimates, the specification being subsequently revised subjectively. Similarly, the spatial covariance of background field errors could not be specified directly from model results and was derived from the results of Rutherford (1972).

Since the near real-time experiments, statistics of both these quantities have been compiled, based on the Phase III observations, analyses and forecasts. These statistics show that for the background field error variance the subjective adjustments made during the early experiments (section 4.2.3) were unduly pessimistic; that is to say, the forecasts, at least in Phase III, were generally of better quality than was assumed.

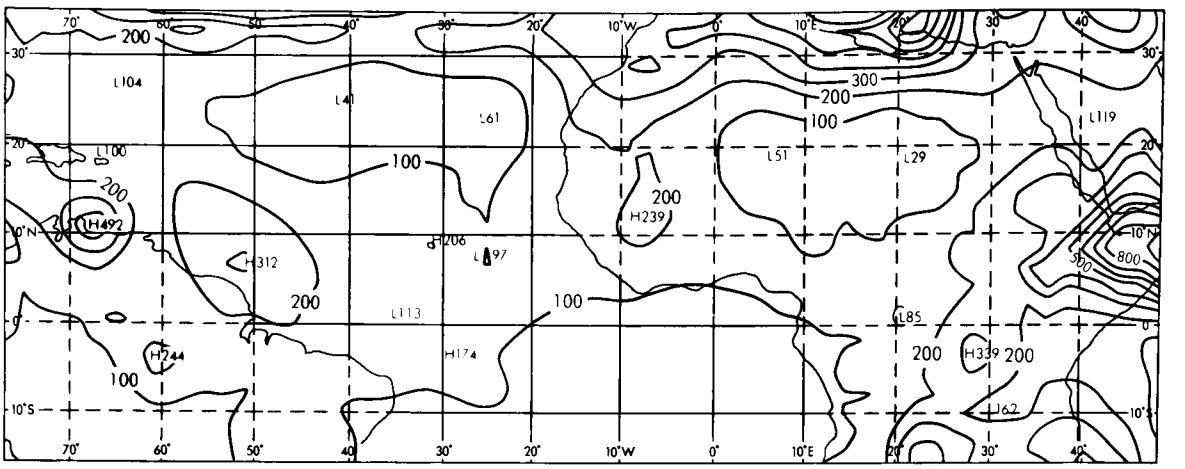

FIGURE 31. Background error variances for geopotential at 850 mb in Phase III
Units: $(gpm)^2$

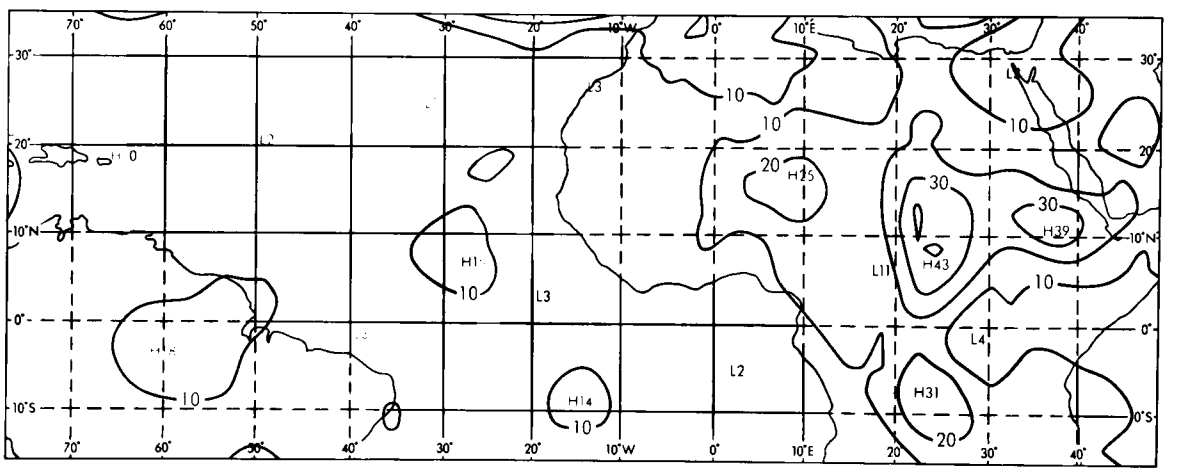

FIGURE 32. Background error variances for zonal wind component at 850 mb in Phase III
Units: $m^2\ s^{-2}$

Figures 31 and 32 show the background field error variances of geopotential and *u*-component of wind respectively at 850 mb. These variances have been derived on the assumption that the objectively analysed fields are correct, that is to say that they can be taken as 'truth'. This assumption can cause errors in the variance fields in two ways. Firstly in data-sparse areas the objective analysis relies heavily on the background field and so a bias is introduced which underestimates the true background field error variance. This effect is evident in both diagrams in the minima found around 25°N over

the Atlantic. Secondly the objective analysis is from time to time based on erroneous observations, as a result of which the true background field error variance is overestimated. This effect is evident in Figure 31 where the local maxima at 11°N, 67°W and 9°N, 49°E have been caused by known errors in the analyses on specific days.

Typical background field error variances at the different primary pressure levels for a 24-hour forecast are about 100 $(\text{gpm})^2$ and 10 $(\text{m s}^{-1})^2$ for geopotential and wind components respectively, over the GATE ship area. The eastern inflow region shows larger error variances, but they are not as large as those adopted for the analysis. It is in the region of the northern boundary where the progression of mid-latitude systems is not well forecast that the background field error variances should be largest. The spatial correlations, derived from the Phase III forecast errors at the primary levels, show a well-structured relationship for the lower troposphere geopotentials. Figure 33 shows the correlation curve for 850 mb. In this diagram the 'background field error' is taken to be observed minus background field values of geopotential, measured at an observation point, and the correlation of this quantity between pairs of stations at different separation distances and for many different pairs of stations has been used to derive the curve shown. The curve is a polynomial, the form of which is shown at the top of the diagram, and the plotted values to which the curve has been fitted represent the average values of

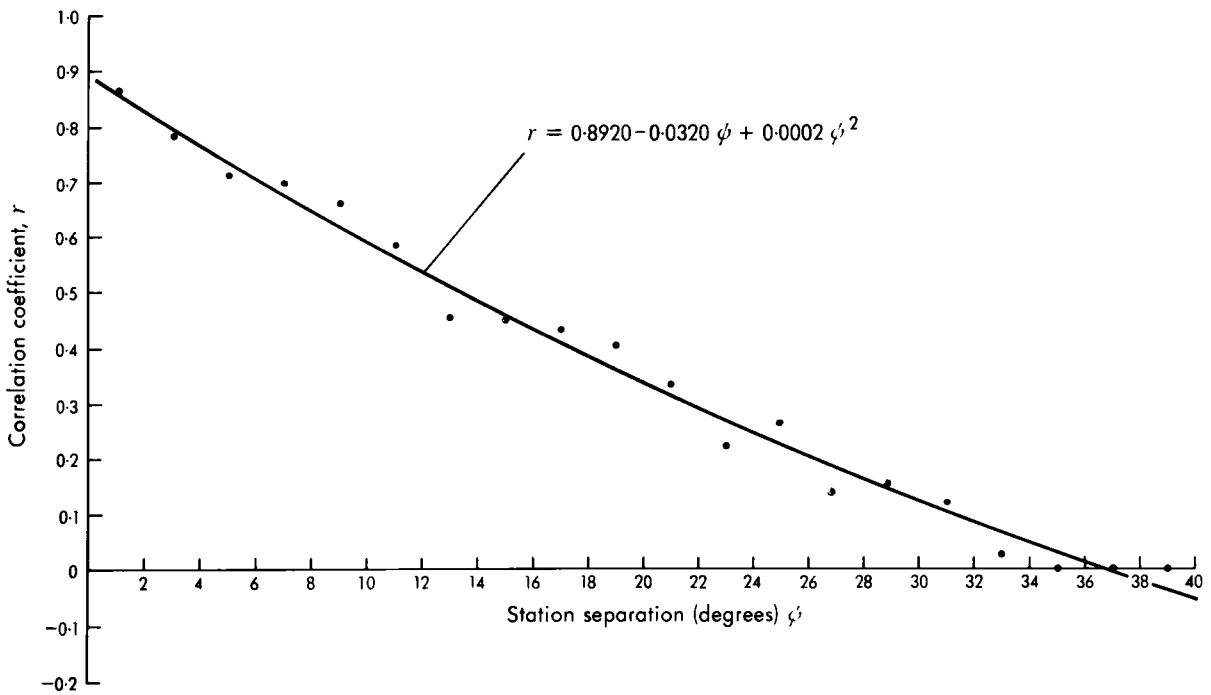

FIGURE 33. Correlation coefficient for geopotential background field errors at 850 mb as a function of station separation (see text for further explanation)

Station separation is measured in terms of the angle (degrees) subtended at the centre of the earth by the great-circle arc passing through the two stations

the correlation over 2° separation ranges, typically based on many individual correlations. The plotted values beyond 35° separation have been artificially constrained to zero. The correlations are mainly based on station pairs within the GATE ship array. The correlation curves for 850 mb and 1000 mb (not shown) are in fact broader structure functions than were used in the analysis originally; the positive correlation at large separation distances can be attributed to the planetary-scale waves discussed by Burpee (1976). For the upper troposphere geopotentials the structure of the curve is less well defined, observational errors being of similar magnitude to true atmospheric variations and to forecast errors. Consequently the spatial correlations of background field errors (in geopotential), which were derived with the aid of observational data, are generally much lower than those used in the original analysis scheme. The spatial correlations of the background wind field errors show a positive correlation out to a separation of about 10° at all levels, the correlation beyond that being small. Figure 34 shows the correlation curve for 850 mb. This curve has been derived in a manner similar to that for Figure 33. The plotted values to which the curve has been fitted represent the average values of the correlation over 1° separation ranges; in each range two values are plotted, being the separate u and v component correlations. The plotted values beyond 10° separation have been artificially constrained to zero. No attempt has been made in the derivation of the curve to take account of possible directional bias in the data sample, or of non-isotropic effects. Both the geopotential and the wind correlations are sensitive to the quality of data used and to the relatively short period (GATE Phase III) making up the sample.

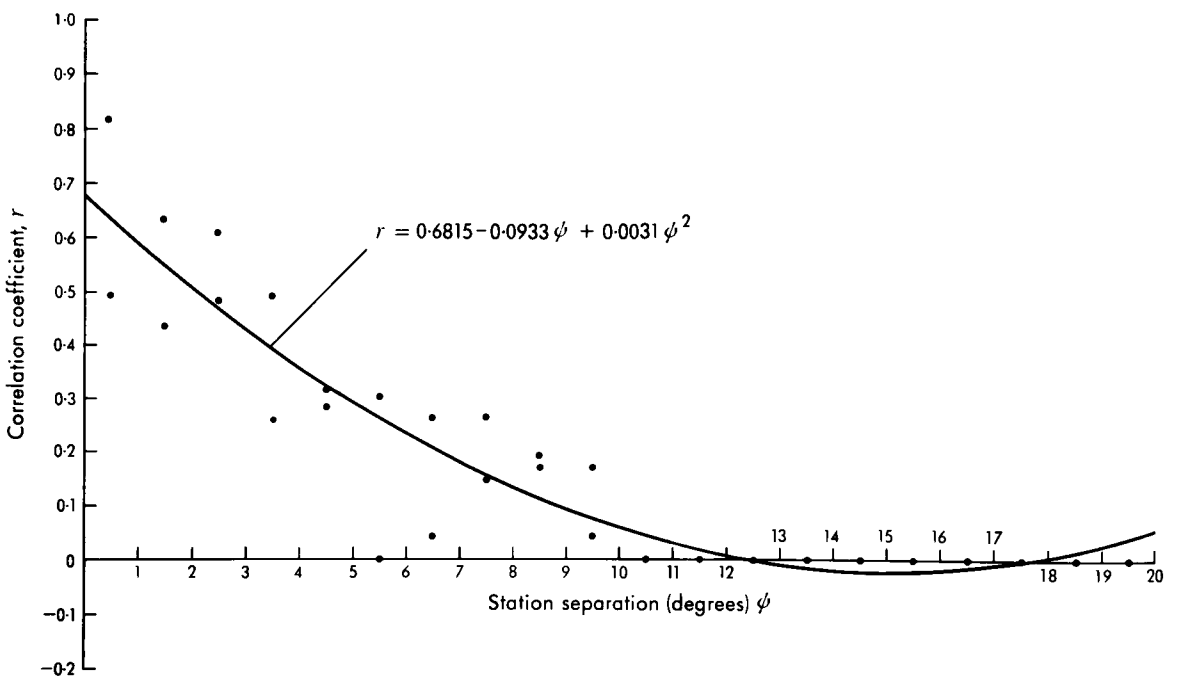

FIGURE 34. As Figure 33 but for 850 mb wind components

10. SOME EXPERIMENTS SINCE GATE

by P. R. Rowntree, Ph.D. and D. B. Shaw, B.Sc.

10.1. *Use of winds to derive geopotentials*

The usefulness of geopotential data in the tropics has often been questioned. Atmospheric variations are frequently less than the observational errors involved in measuring these variations. Some tropical analysis schemes make no use of reported geopotentials, working exclusively with the wind data. With this in mind, and in order to try to eliminate the problem discussed above, some experiments have been made in which the analyses were based almost entirely on wind data. This was done by deriving geopotential fields from the wind fields, using the balance equation in the fashion discussed earlier (section 4.3). In this process the only role played by geopotential data is in determining the boundary values of geopotential required for solving the balance equation. With the original formulation for surface friction (section 4.3.2), analyses carried out for 12 GMT on 4 September using this technique and using the enhanced data coverage provided by the paper tape collection service organized by the GATE Synoptic-scale Subprogram Data Centre, gave geopotential fields at 850 mb and above which were generally similar to, but smoother than, those derived from geopotential data. However, at 1000 mb over Africa (Figures 35 and 36), the geopotential gradients derived from the analysed winds at 10 m were too weak, with only a very shallow Saharan trough. Near the surface over land the frictional stress is an important term in the balance equation and it seemed possible to improve on the formulation given in section 4.3.2 in which the stress was assumed to vary linearly between 1000 and 900 mb.

Boundary-layer wind data indicate that $\partial\tau/\partial z$, the vertical gradient of the stress, is greater at 10 m than in the mean from 1000 to 900 mb. For example, an interpolation of the Leipzig wind profile data gives

$$\beta_* \equiv -\frac{|\partial\tau/\partial z|}{|\tau_0|} = 2.2 \times 10^{-3},$$

where τ_0 is the surface stress. Section 4.3.2. implies a value of β_* only half as large. If the formulation of τ_0 is also changed, to

$$\tau_0 = \rho C_D |\mathbf{V}_{10}| \mathbf{V}_{10},$$

where $\mathbf{V}_{10}$ is the wind at 10 metres, and $C_D = 1.2 \times 10^{-3}$ over sea and 7.54×10^{-3} over land, values appropriate for neutral conditions with roughness lengths of 0.01 and 10 cm respectively, then the frictional term in the balance equation may be written as

$$\nabla \cdot \left[\frac{\partial}{\partial z}\left(\frac{\tau}{\rho}\right)\right] = \frac{1}{a\cos\theta}\frac{\partial}{\partial\lambda}\left[C_D|\mathbf{V}_{10}|\,(\alpha_* v_{10} - \beta_* u_{10})\right] -$$

$$-\frac{1}{a\cos\theta}\frac{\partial}{\partial\theta}\left[C_D|\mathbf{V}_{10}|\,(\beta_* v_{10} + \alpha_* u_{10})\cos\theta\right],$$

where $-\alpha_*$ is the rate of change with height of the angle between τ and the geostrophic wind, taken as $-\alpha_* = -2.6 \times 10^{-3}$ m^{-1}. With this formulation (due to D. J. Carson (private communication)), the 1000 mb geopotential field (Figure 37) was considerably

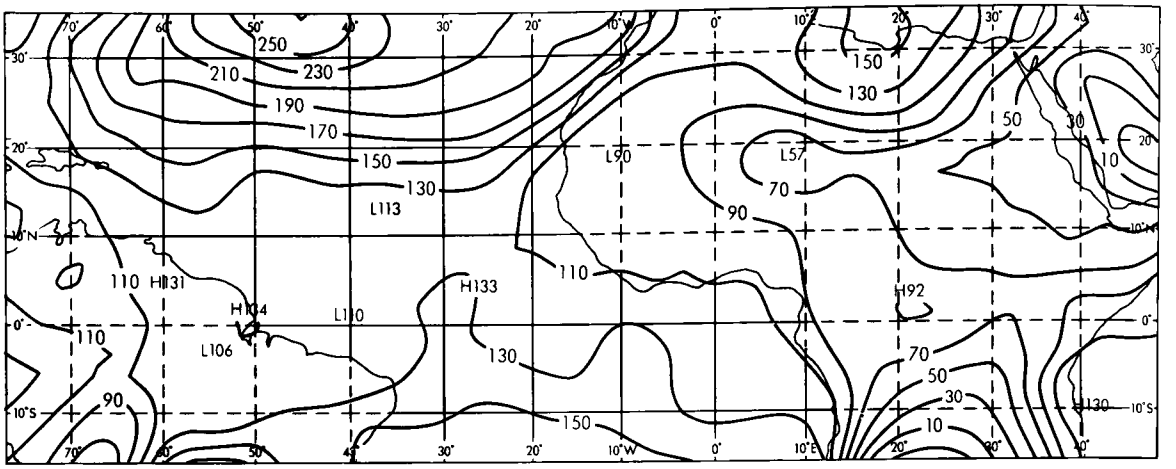

FIGURE 35. 1000 mb geopotentials for 12 GMT on 4 September 1974 analysed by the scheme in operation during GATE

Units: gpm

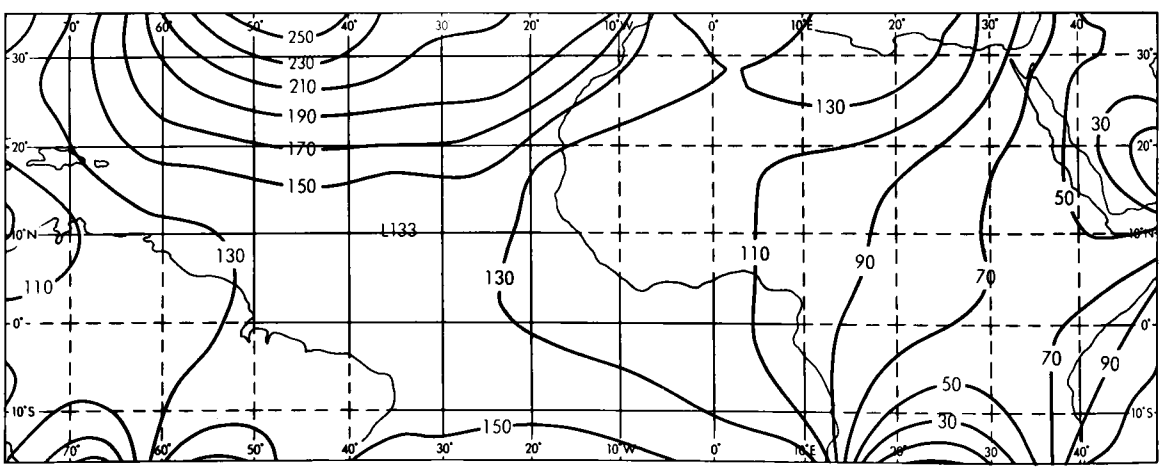

FIGURE 36. 1000 mb geopotentials for 12 GMT on 4 September 1974 derived from the corresponding wind field by solution of the balance equation with friction as represented in the scheme operated during GATE

Units: gpm

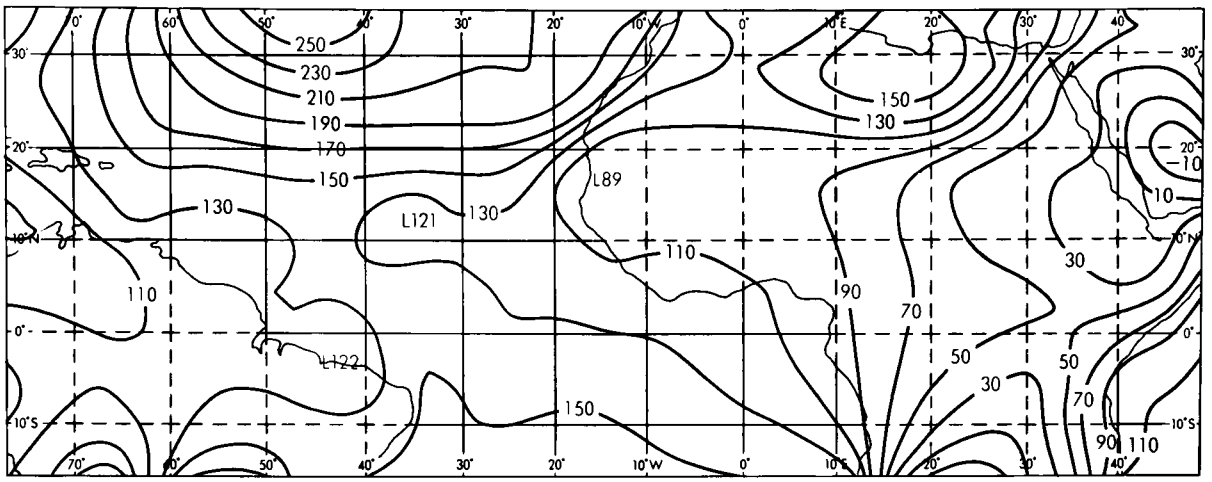

FIGURE 37. As Figure 36 but using Carson's friction formulation

improved over Africa with the low near the west coast reappearing. The low shown in Figure 35 north-west of Lake Chad is still absent. This low was based on one pressure observation which appears to be about 2 mb low on the basis of pressure tendency checks. The error in this region in Figure 37 is thus probably about +20 gpm.

Over the Atlantic there are smaller changes due to the friction modification, generally towards the original analysis. Over South America a trough reappears near the north coast somewhat like that discernible through the roughness of Figure 35. Results of a similar character were obtained for 12 GMT on 10 September.

The most noticeable change brought about by the use of the balance equation in analysis at 850 mb was over east Africa, north of Lake Victoria, where a trough feature found in the geopotential analysis had been filled by 30 gpm. The effect of this change in the 24-hour forecast was quite dramatic, for on the 24-hour rainfall fields, a spurious rainfall maximum over the region of 100 mm was reduced by a factor of two, whilst the convergent/divergent flows in the two halves of the troposphere were also greatly reduced.

10.2. *Results with a new convective parametrization*

The forecasts shown in Figures 35 to 37 differed from those made in near-real time, not only in the initial data and its treatment, but also in their use of a convective parametrization designed to represent the effects of penetrative convection rather than the convective mixing between adjacent layers applied previously. The new scheme is based on the concept of parcel theory with a simple treatment of entrainment and detrainment.

We imagine an ensemble of buoyant plumes of different radii, temperatures and humidities. Their characteristics will determine their entrainment rates and hence their upward extent. The less buoyant plumes will terminate and detrain through lack of buoyancy at a lower level than more buoyant plumes which may, in favourable conditions, reach the heights accessible to an undiluted parcel. Rather than attempting to treat plumes of different characteristics separately we have considered the mean characteristics of the ensemble. These are modified by an entrainment rate which decreases

with height as the mean plume radius is assumed to increase, and by a detrainment of air from less buoyant plumes as they die; since this detrainment is at environmental buoyancy it enhances the positive mean buoyancy of the ensemble. The environment is modified by removal of entrained air, addition of detrained air, the compensating subsidence and the evaporation of precipitation.

The effects of the change from the GATE convection scheme are illustrated in Figures 38 and 39 by the rainfall on the third day of forecasts from the GATE wind and balanced geopotential analyses for 12 GMT on 10 September 1974. Although on the first day (not shown) the intense small-scale rainfall maxima evident with forecasts from analysed

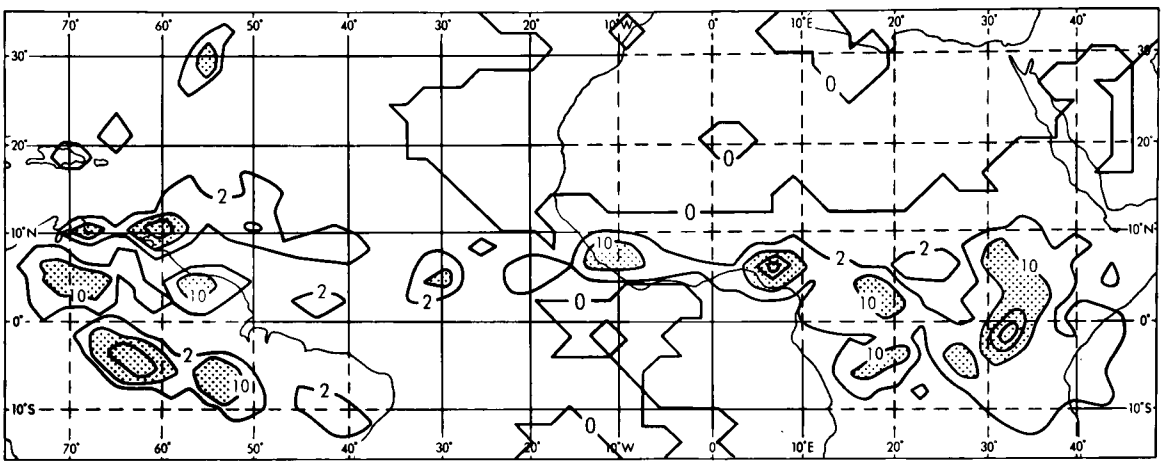

FIGURE 38. Rainfall (mm) predicted for 24 hours ending 12 GMT on 13 September 1974 from initial data for 12 GMT on 10 September 1974, using GATE model convection scheme (and geopotentials derived from winds through the balance equation)
Isopleths at 2, 10, 50, 100 mm/day.

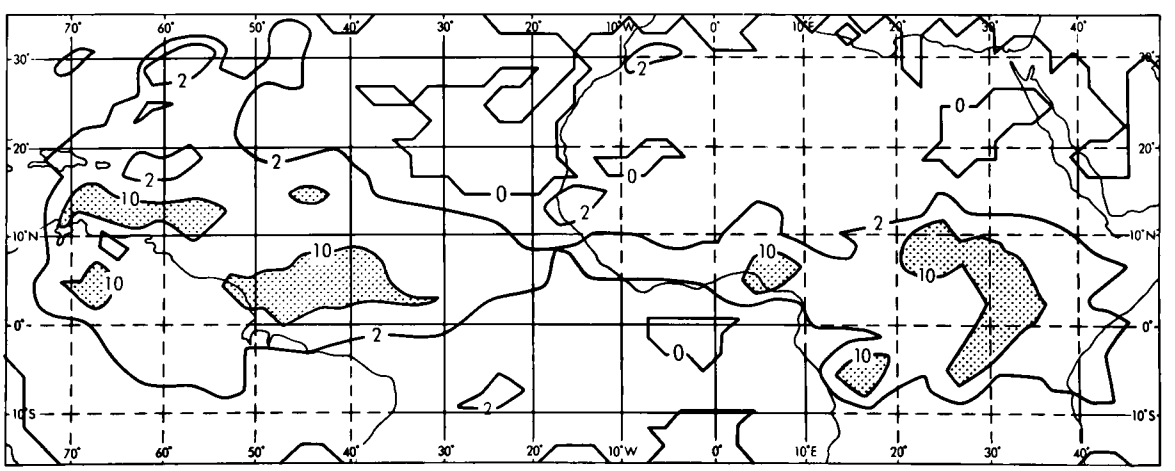

FIGURE 39. As Figure 38 but using the penetrative convection scheme

geopotential fields were absent, by the third day with the GATE convection scheme several intense rain areas have been generated. With the new scheme, on the other hand, the maximum rainfall on the third day is 37 mm.

It should be mentioned that these two forecasts also used different sea surface temperatures, those for the forecast with the GATE convection scheme being August normals and those for the penetrative convection experiment being GATE Phase III means which were of the order of 1 K warmer over much of the area. The main effects of this change, an equatorward spread of about 2° latitude in the east Atlantic rainfall, were very small relative to the differences due to the change in the convection scheme.

Figures 40 and 41 (a) and (b) show some results of a forecast to 8 days with initial geopotential fields derived from the winds by the balance equation, and using the new convection scheme. Despite the fixed boundary conditions, the movement of 850 mb troughs was surprisingly well forecast throughout the eight days (Figure 40) although there were increasing errors in trough shape and intensity.

The rainfall predictions have been verified for two regions (Figure 41), one over west Africa (Figure 41(a)) and one over the GATE ships (Figure 41(b)). The magnitudes of daily rainfall are quite realistic over the west African region; over the GATE ships the heavy rains of 5 September 1974 are predicted but rainfall is deficient after Day 3.

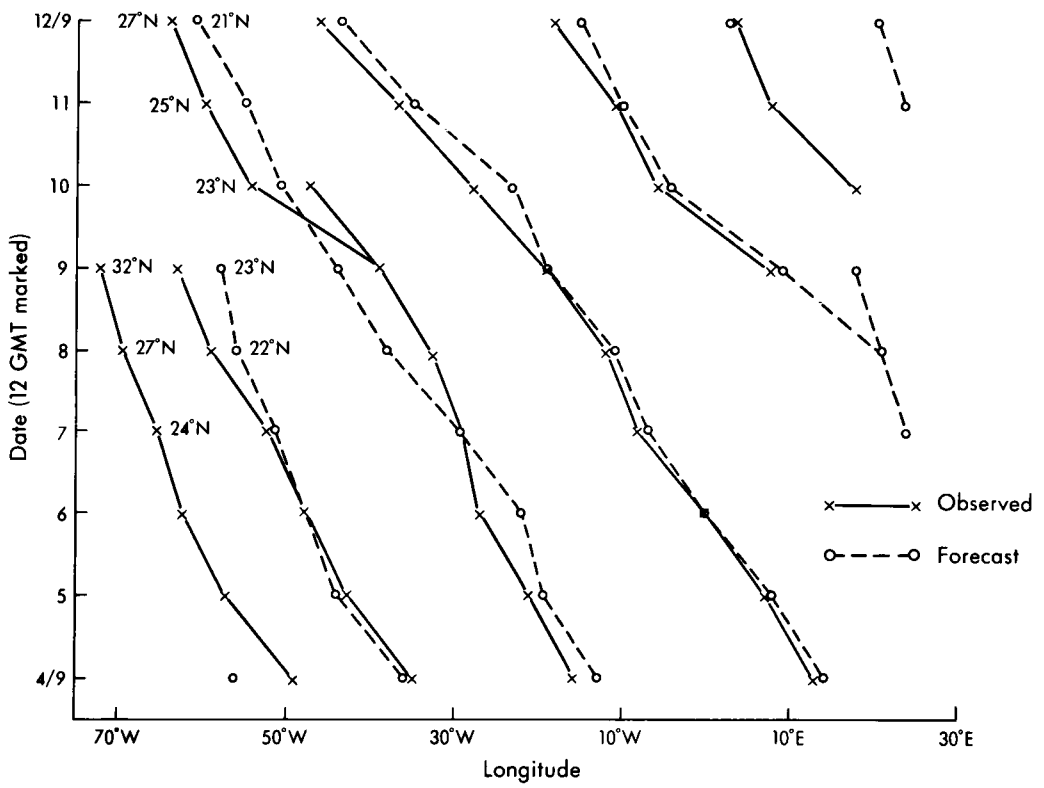

FIGURE 40. 850 mb trough positions as observed and as predicted in an 8-day forecast from initial data for 12 GMT on 4 September 1974 (latitude near 13°N except where indicated)

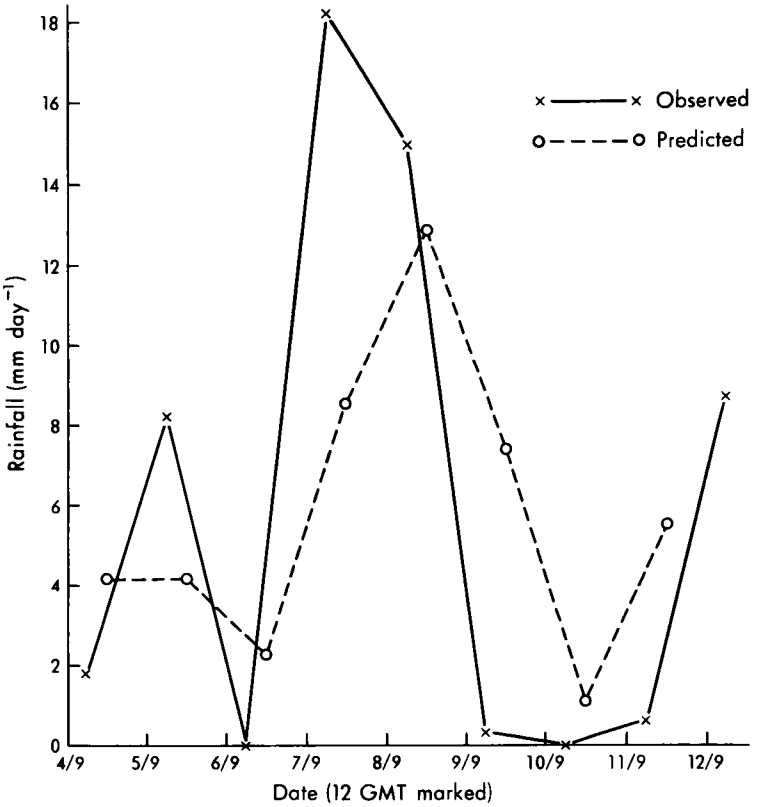

FIGURE 41(a). 24-hour rainfall for 10°–15°N, 10°–15°W: observed and predicted from initial data for 12 GMT on 4 September 1974

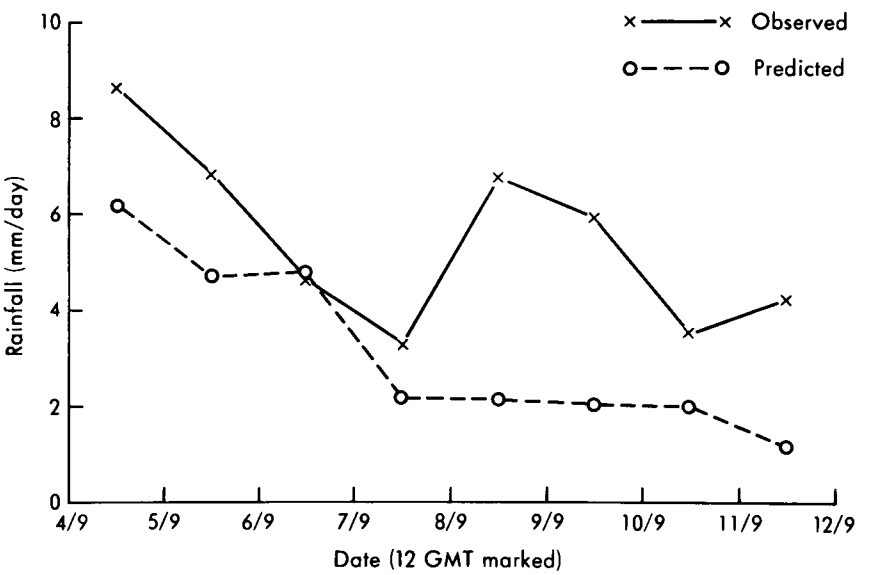

FIGURE 41(b). As for Figure 41(a) but for 6°–12°N, 20°–26°W

11. CONCLUDING REMARKS

This paper has described modelling work with a tropical forecast suite developed specifically to take advantage of the increased data coverage in the tropical Atlantic during GATE. The techniques used are undoubtedly capable of improvement. This naturally applies particularly to the analysis system which was designed for, and developed during, GATE. In particular it is felt that not enough attention was paid to obtaining a consistent vertical structure in the temperature and stability fields. It might also have been better for the analyses to have been made directly on σ-surfaces to avoid interpolation to and from the pressure coordinate system, for this process can lose detail in the vertical structure. Further study of the structure functions involved should lead to improvements in the depiction of details in areas of dense data; a start on such work was discussed in section 9.

The running of the forecast suite in near-real time during GATE was of value in several ways, especially because it stimulated interest and concentrated effort on solving the problems that arose. The real-time use of the data provided information to the Synoptic-scale Subprogram Data Centre on the availability and quality of the data on the Global Telecommunication System. Daily running of the programs in the suite greatly accelerated the detection and correction of errors. However, the resulting analyses might have been of greater subsequent value had it been possible to mount a short (say 10-day) trial experiment early enough to allow revisions and further testing of the suite so that a substantial part of the improvements actually made during GATE could have been made before GATE. The time required for this would have been of the order of two months or more. Any such test would have been without the important GATE ship data and the satellite wind data. Nevertheless an earlier start to testing of the full scheme, had it been possible, would have allowed earlier treatment of the problems associated with detection of program errors, analysis of boundary regions and treatment of erroneous data including the systematic errors in satellite temperature data. This needs to be taken into account when planning future experiments.

The availability of the GATE analyses has allowed substantial progress in development of the tropical model. Experiments with the model (some discussed in section 10, others reported by Rowntree (1979), Slingo (1980) and Gilchrist *et al.* (1982)) have investigated its sensitivity to soil moisture and the parametrization of radiative and cloud processes, and convection. Some of these have already led to improved parametrizations in the tropical model which either have been used or are expected to be used in global circulation models. Also since GATE the forecast suite has been used in experimental predictions for the Indian Monsoon Region (Shaw, 1978) and has been extended to cover the whole of the tropics in order to provide initial analyses for experimental predictions with models covering the globe north of 15°S.

ACKNOWLEDGEMENTS

Many people contributed to the execution and analysis of the GATE modelling experiment. It is particularly desirable here to acknowledge the contribution of those who designed and wrote the programs used in the experiment. The data extraction scheme was largely planned by Dr K. M. Carpenter and programmed by Mr D. M. Pusey, using

retrieval routines made available by the Data Processing Branch of the Meteorological Office. The analysis scheme was devised by scientists of the Forecasting Research Branch, primarily Mr D. E. Jones, Mr A. Belyavin and Dr S. A. Clough. Much of the practical work in implementing it was carried out by Miss Mavis K. Hinds and Mr C. S. Clarke. Most of the work in design, and writing and adaptation of programs for other sections of the suite, was by the persons who have contributed the relevant sections of this paper; additionally Dr K. M. Carpenter was involved in the design of the interpolation scheme and much of the writing of output programs was by Mr R. S. Walker.

BIBLIOGRAPHY

ALAKA, M. A. and ELVANDER, R. C.; 1972, Optimum interpolation from observations of mixed quality. *Mon Weather Rev,* **100,** pp. 612–624.

ATKINS, MARGARET J.; 1974, The objective analysis of relative humidity. *Tellus,* **26,** pp. 663–671.

BERKOFSKY, L. and BERTONI, E. A.; 1960, Topographic charts at one-degree intersections for the entire earth. Bedford, Mass., Air Force Cambridge Research Laboratories, GRD Research Notes, No. 42.

BURPEE, R. W.; 1974, Characteristics of North African easterly waves during the summers of 1968 and 1969. *J Atmos Sci,* **31,** pp. 1556–1570.

——; 1976, Some features of global-scale 4–5 day waves. *J Atmos Sci,* **33,** pp. 2292–2299.

BURRIDGE, D. M. and GADD, A. J.; 1977, The Meteorological Office operational 10-level numerical weather prediction model (December 1975). *Sci Pap, Meteorol Off,* No. 34.

CATTLE, H.; 1982, The equivalence of the GATE and Gandin optimum interpolation schemes. (Unpublished, copy available in the National Meteorological Library, Bracknell.)

CHARNOCK, H.; 1955, Wind stress on a water surface. *Q J R Meteorol Soc,* **81,** pp. 639–640.

CLARKE, R. H.; 1970, Recommended methods for the treatment of the boundary layer in numerical models. *Aust Meteorol Mag,* **18,** pp. 51–73.

CORBY, G. A., GILCHRIST, A. and NEWSON, R. L.; 1972, A general circulation model of the atmosphere suitable for long period integrations. *Q J R Meteorol Soc,* **98,** pp. 809–832.

CORBY, G. A., GILCHRIST, A and ROWNTREE, P. R.; 1977, United Kingdom Meteorological Office five-level general circulation model. *Methods Comp Phys,* **17,** pp. 67–110.

DOPPLICK, T. G.; 1970, Global radiative heating of the earth's atmosphere. Cambridge, Mass., Massachusetts Institute of Technology, Department of Meteorology, Planetary Circulations Project, Report No. 24.

FRANCIS, P. E.; 1975, The use of a multipoint filter as a dissipative mechanism in a numerical model of the general circulation of the atmosphere. *Q J R Meteorol Soc,* **101,** pp. 567–582.

GANDIN, L. S.; 1963, An objective analysis of meteorological fields allowing for their statistical structure. Leningrad, *Gl Upr Gidrometeorol.* (Translated by the Israel Program for Scientific Translations, Jerusalem, 1965.)

GILCHRIST, A., ROWNTREE, P. R. and SHAW, D. B.; 1982, Large scale modelling. The GARP Atlantic Tropical Experiment (GATE) Monograph. WMO/ICSU, GARP Publications Series No. 25, pp. 183–218.

HALTINER, G. J.; 1971, Numerical weather prediction. New York, John Wiley & Sons, Inc.

HARTREE, D. R.; 1958, Numerical analysis (second edition). Oxford, Clarendon Press.

HAWSON, C. L. and CATON, P. G. F.; 1961, A synoptic method for the international comparison of geopotential observations. *Meteorol Mag,* **90,** pp. 336–344.

JONES, D. E.; 1976, The United Kingdom Meteorological Office objective analysis scheme for GATE. *Meteorol Mag,* **105,** pp. 249–260.

KESEL, P. G. and WINNINGHOFF, F. J.; 1972, The Fleet Numerical Weather Central operational primitive-equation model. *Mon Weather Rev,* **100,** pp. 360–373.

KNIGHTING, E., CORBY, G. A. and ROWNTREE, P. R.; 1962, An experiment in operational numerical weather prediction. *Sci Pap, Meteorol Off,* No. 16.

KRAVCOVA, L. M.; 1968, Climatic characteristics of cloudiness in the IGY, Southern hemisphere. Vol. 2, Africa and Australia. Moscow, Naucno Issledovatel'skij Institut Aeroklimatologii (in Russian).

KRISHNAMURTI, T. N.; 1969, An experiment in numerical prediction in equatorial latitudes. *Q J R Meteorol Soc,* **95,** pp. 594–620.

——; 1971, Observational study of the tropical upper tropospheric motion field during the northern hemisphere summer. *J Appl Meteorol,* **10,** pp. 1066–1096.

KRISHNAMURTI, T. N., LEVY, C. E. and PAN, H.-L.; 1975, On simultaneous surges in the trades. *J Atmos Sci,* **32,** pp. 2367–2370.

KRUGER, H. B.; 1969, General and special approaches to the problem of objective analysis of meteorological variables. *Q J R Meteorol Soc,* **95,** pp. 21–39.

LEWIS, J. M. and GRAYSON, T. H.; 1972, The adjustment of surface wind and pressure by Sasaki's variational matching technique. *J Appl Meteorol,* **11,** pp. 586–597.

LOBANOVA, V. JA.; 1967, Climatic charts of cloudiness in the northern hemisphere. January and July (Period IGY and IGC). Moscow, Naucno Issledovatel'skij Institut Aeroklimatologii (in Russian).

LYNE, W. H., ROWNTREE, P. R., TEMPERTON, C. and WALKER, JULIA M.; 1975, Numerical modelling during GATE. (Unpublished, copy available in the National Meteorological Library, Bracknell.)

——; 1976, Numerical modelling using GATE data. *Meteorol Mag,* **105,** pp. 261–271.

METEOROLOGICAL OFFICE; 1948, Monthly meteorological charts of the Atlantic Ocean, M.O. 483 (reprinted 1959). London, HMSO.

——; 1976, A scheme for the objective analysis of GATE data. (Unpublished, copy available in the National Meteorological Library, Bracknell.)

NITTA, T.; 1969, Initialization and analysis for the primitive equation model. Proceedings of the WMO/IUGG Symposium on Numerical Weather Prediction, Tokyo, November 26–December 4 1968. Tokyo, Japan Meteorological Agency.

ØKLAND, H.; 1972, On the balance, initialization and data assimilation in primitive equation prediction models. *J Atmos Sci,* **29,** pp. 641–648.

OORT, A. H. and RASMUSSON, E. M.; 1971, Atmospheric circulation statistics. US Department of Commerce, NOAA Professional Paper No. 5.

PERKEY, D. J. and KREITZBERG, C. W.; 1973, Mesoscale primitive equation forecasts nested within a large-scale forecast. Paper presented at the WMO/IAMAP Symposium on Mesoscale Meteorological Systems and Fine-mesh Modelling, Shinfield Park, United Kingdom, May 1973.

PHILLIPS, N. A.; 1960, On the problem of initial data for the primitive equations. *Tellus,* **12,** pp. 121–126.

PRIESTLEY, C. H. B. and TAYLOR, R. J.; 1972, On the assessment of surface heat flux and evaporation using large-scale parameters. *Mon Weather Rev,* **100,** pp. 81–92.

REED, R. J., NORQUIST, D. C. and RECKER, E. E.; 1977, The structure and properties of African wave disturbances as observed during Phase III of GATE. *Mon Weather Rev,* **105,** pp. 317–333.

RODGERS, C. D.; 1967, The radiative heat budget of the troposphere and lower stratosphere. Cambridge, Mass., Massachusetts Institute of Technology, Department of Meteorology, Planetary Circulations Project, Report No. A2.

ROWNTREE, P. R.; 1975, The representation of radiation and surface heat exchange in a general circulation model. (Unpublished, copy available in the National Meteorological Library, Bracknell.)

——; 1979, Numerical prediction and simulation of the tropical atmosphere. *In* SHAW, D. B. (ed.), Proceedings of Conference on Meteorology over Tropical Oceans, Royal Meteorological Society, pp. 219–249.

RUTHERFORD, I. D.; 1972, Data assimilation by statistical interpolation of forecast error fields. *J Atmos Sci,* **29,** pp. 809–815.

SADLER, J. C.; 1975, The upper tropospheric circulation over the global tropics. Honolulu, University of Hawaii, Department of Meteorology, UHMET-75-05.

SAKER, N. J.; 1975, An 11-layer general circulation model. (Unpublished, copy available in the National Meteorological Library, Bracknell.)

SASAKI, Y.; 1970, Some basic formalisms in numerical variational analysis. *Mon Weather Rev*, **98**, pp. 875–883.

SHAPIRO, R.; 1971, The use of linear filtering as a parametrization of atmospheric diffusion. *J Atmos Sci*, **28**, pp. 523–531.

SHAW, D. B.; 1978, Numerical prediction experiments in the monsoon region. *Indian J Meteorol Hydrol Geophys*, **29**, pp. 361–366.

SLINGO, JULIA M.; 1980, A cloud parametrization scheme derived from GATE data for use with a numerical model. *Q J R Meteorol Soc*, **106**, pp. 747–770.

SPACKMAN, E. A. and FARMER, S. F. G.; 1975, Synoptic-scale data received at Bracknell during GATE. (Unpublished, copy available in the National Meteorological Library, Bracknell.)

TEMPERTON, C.; 1976, Dynamic initialization for barotropic and multi-level models. *Q J R Meteorol Soc*, **102**, pp. 297–311.

THOMPSON, B. W.; 1965, The climate of Africa. London, Oxford University Press.

U.S. NAVAL OCEANOGRAPHIC OFFICE; 1967, Oceanographic atlas of the North Atlantic Ocean. Section II: Physical properties. Washington, D. C., Publication No. 700.

WACHSPRESS, E. L.; 1966, Iterative solution of elliptic systems and applications to the neutron diffusion equations of reactor physics. Englewood Cliffs, N.J., Prentice-Hall.

WORLD METEOROLOGICAL ORGANIZATION; 1972, Experiment design proposal for the GARP Atlantic Tropical Experiment. GATE Report No. 1.

Printed in UK for Her Majesty's Stationery Office
Dd 717745 PS 2250554 C.10 7/83 33626

HER MAJESTY'S STATIONERY OFFICE
Government Bookshops
49 High Holborn, London WC1V 6HB
13a Castle Street, Edinburgh EH2 3AR
Brazennose Street, Manchester M60 8AS
Southey House, Wine Street, Bristol BS1 2BQ
258 Broad Street, Birmingham B1 2HE
80 Chichester Street, Belfast BT1 4JY
Government publications are also available through booksellers

ISBN: 011 400 3424.